

The inversion of data from very large 3-D ERT mobile surveys.

M.H. Loke^{1*}, N. Papadopoulos², P.B. Wilkinson³, D. Oikonomou^{2,4}, K. Simyrdanis²
and D. Rucker⁵

¹ Geotomo Software Sdn Bhd, 115 Cangkat Minden Jalan 6, 11700 Gelugor, Penang, Malaysia.

email : drmhloke@yahoo.com

² Laboratory of Geophysical-Remote Sensing & Archaeoenvironment (GeoSat ReSeArch), Institute for Mediterranean Studies, Foundation for Research and Technology Hellas, Nikiforou Foka 130, 74 100 Rethymno, Crete, Greece.

emails : nikos@ims.forth.gr, doikonomou@ims.forth.gr, ksimirda@ims.forth.gr

³ British Geological Survey, Keyworth, Nottingham, NG12 5GG, U.K.

email : pbw@bgs.ac.uk

⁴ Aristotle University of Thessaloniki, Thessaloniki, Greece.

⁵ hydroGEOPHYSICS Inc., 2302 North Forbes Boulevard, Tucson, AZ 85745, U.S.A.

email : druck8240@gmail.com

* Corresponding author

Keywords : Resistivity inversion, 3-D, segmentation

Abstract

New developments in mobile resistivity meter instrumentation have made it possible to survey large areas with dense data coverage. The mobile system usually has a limited number of electrodes attached to a cable that is pulled along behind an operator so that a large area can be covered within a short time. Such surveys can produce 3-D data sets with hundreds of thousands of electrodes positions and data points. Similarly, the inverse model used to interpret the data can have several hundred thousand cells. It is impractical to model such large data sets within a reasonable time on microcomputers used by many small companies employing standard inversion techniques. We describe a model segmentation technique that subdivides the finite-element mesh used to calculate the apparent resistivity and Jacobian matrix values into a number of smaller meshes. A fast technique that optimises the calculation of the Jacobian matrix values for multi-channel systems was also developed. A 1-D wavelet transform method was then used to compress the storage of the Jacobian matrix, in turn reducing the computer time and memory required to solve the least-squares optimisation equation to determine the inverse model resistivity values. The new techniques reduce the calculation time and memory required by more than 80% while producing models that differ by less than 1% from that obtained using the standard inversion technique with a single mesh. We present results using a synthetic model and a field data set that illustrates the effectiveness of the proposed techniques.

Data Availability Statement

The data that support the findings of this study are available from the corresponding author upon reasonable request.

INTRODUCTION

3-D ERT (Electrical Resistivity Tomography) surveys are now widely used to map areas with complex geology (Loke *et al.* 2013a). Most surveys use multi-channel resistivity meter systems with the electrodes planted in the ground. A system with 32 to 128 electrodes linked by multi-core cables to the resistivity meter is frequently used. The number of unique electrode positions used in the survey usually does not exceed a few thousand. Compared to normal 'static' resistivity meter systems, 'mobile' systems use a cable with a more limited number of electrodes (4 to 12) that is pulled along the surface. Some surveys use a normal galvanic resistivity-meter system with a streamer pulled behind a boat in a water-covered area (Rucker and Noonan 2013; Simyrdanis *et al.* 2015). In land surveys capacitively coupled systems (Hildes *et al.* 2005; Kuras *et al.* 2006; Unrau 2019) can be used that avoid direct galvanic contact with the ground where a limited number of measurements are simultaneously made at approximately regular intervals. Both types use a GPS receiver attached to a computerised central system to trace the position of the line and subsequently estimate the actual position of the electrodes with a certain accuracy based on specific assumptions (Oikonomou *et al.* 2019). The streamer is pulled to and fro crisscrossing the survey area to get dense data coverage. In some surveys, the number of unique electrode positions can exceed a hundred thousand. A 3-D finite-element mesh is used to model the resistivity data so that topography can be directly incorporated into the inverse model (Loke 2000). To accurately model the data from such large surveys, a dense mesh with more than one million nodes is sometimes used. The combination of a large number of electrode positions together with a large mesh presents computational problems in terms of computer execution time and high memory demands.

1
2
3 To reduce these computational issues, some researchers in the past have
4 resorted to shortcuts, such as binning electrode positions, nudging electrode positions
5 and subdomains. Xu and Dunbar (2015) took methods from marine-based streaming
6 seismic acquisition through data binning. The technique of binning converts a series
7 of closely spaced 2-D profiles into a quasi-3-D survey through combining scattered
8 data points onto regular grids and then conducting 3-D inversion. The survey is
9 divided into multiple rectangular horizontal zones called bins on the surface and each
10 measurement is assigned to a bin according to the midpoint between the source and
11 the receiver. The apparent resistivity measurements are sorted into bins based on the
12 centre points of each four-electrode configuration and there will typically be multiple
13 measurements placed into a single bin. The bin size is selected based on the data
14 density and the required resolution of the 3-D inversion, balanced with the time
15 required to complete the resulting 3-D inversion. Rucker *et al.* (2009) used a concept
16 called nudging to move the electrode positions for ease of modelling. To decrease the
17 number of unique electrode positions, thereby reducing the number of mesh nodes
18 needed for inversion, they nudged electrodes to the nearest 3 m. The initial survey
19 design was established on a 3 m grid, but a few of the electrode coordinates for non-
20 orthogonal lines had to be repositioned to reduce memory storage. Their justification
21 for nudging was a trade-off between accuracy and expediency, for what was at the
22 time, the largest published 3-D modelling study with over 7,000 electrode positions.
23
24
25
26
27
28
29
30
31
32
33
34
35
36
37
38
39
40
41
42
43
44
45
46
47
48

49 Rucker *et al.* (2009) also experimented with manually dividing the large
50 model domain into individually processed, smaller subdomains in order to reduce the
51 computer memory usage; computer memory was generally quite low at the time of the
52 study relative to today. Experiments with the subdomains included increasing the
53 amount of overlap for adjacent models. Four sets of model overlap were tested
54
55
56
57
58
59
60

1
2
3 including: 15 m (6 total model domains), 50 m (8 total model domains), 100 m (15
4 total model domains), and 150 m (50 total model domains). The results of modelling
5
6 total model domains), and 150 m (50 total model domains). The results of modelling
7
8 with a large number of subdomains were undesirable, showing mismatches in target
9
10 shape and values in the areas of overlap.
11

12 In this paper we describe techniques to reduce the computer time and memory
13 needed so that the data inversion to produce a 3-D model can be completed within a
14 reasonable time with common personal computers. We use a method similar to
15 Rucker *et al.* (2009) in creating subdomains. Here, we refer to it as mesh
16 segmentation. The difference in the methodology, however, is that the overlap from
17 one domain is accommodated in the other domains to ensure continuity in model
18 values. While the potentials and sensitivity values are calculated individually for each
19 segment (similar to the subdomain technique), a single unified model inversion step is
20 carried out that covers the entire survey area. This greatly reduces mismatches in the
21 areas of overlap.
22
23
24
25
26
27
28
29
30
31
32
33
34

35 We test the new mesh segmentation method on synthetic and field data sets
36 and demonstrate that the results are nearly identical to modelling all of the data using
37 a single mesh. The advantage, however, is the significantly reduced computer time
38 and memory.
39
40
41
42
43
44
45
46
47
48

49 **DATA INVERSION METHOD**

50
51 For 3-D ERT data sets, the smoothness-constrained least-squares optimisation
52 method is widely used (Li and Oldenburg 2000, Loke *et al.* 2013a). The linearised
53 least-squares equation that gives the relationship between the model parameters (\mathbf{r})
54 and the data misfit (\mathbf{g}) is given below.
55
56
57
58
59
60

$$\left[\mathbf{J}_i^T \mathbf{R}_d \mathbf{J}_i + \lambda_i \mathbf{W}^T \mathbf{R}_m \mathbf{W} \right] \Delta \mathbf{r}_i = \mathbf{J}_i^T \mathbf{R}_d \mathbf{g}_i - \lambda_i \mathbf{W}^T \mathbf{R}_m \mathbf{W} (\mathbf{r}_{i-1} - \mathbf{r}_m) \quad (1)$$

The Jacobian matrix \mathbf{J} contains the partial derivatives of the measured data (apparent resistivities) with respect to the model resistivity. The inversion procedure is stabilised through the roughness filter \mathbf{W} (deGroot-Hedlin and Constable 1990) with a damping factor λ . $\Delta \mathbf{r}_i$ is the required change in the model parameters (the logarithms of the model resistivity values) to reduce the data misfit \mathbf{g} while \mathbf{r}_{i-1} is the resistivity model from the previous iteration. The vector \mathbf{r}_m is a reference background model. \mathbf{R}_d and \mathbf{R}_m are weighting matrices used by the L1-norm inversion method (Farquharson and Oldenburg 1998) applied to the data misfit and model roughness. The inversion algorithm usually takes 3 to 6 iterations to converge. In the tests with the data sets carried out in this paper, we used the L1-norm for both the data misfit and model roughness. Further details on the practical use of the least-squares iterative method, such as the use of different norms and selection of the damping factor, can be found in the references (Farquharson and Oldenburg 1998; Loke *et al.* 2003; Farquharson and Oldenburg 2004; Loke *et al.* 2014a).

Each iteration requires the calculation of the model response (calculated apparent resistivity values) using the finite-element method and the Jacobian matrix using the adjoint-equation method (McGillivray and Oldenburg 1990). The least-squares equation (1) then needs to be solved to determine the change in the model parameters ($\Delta \mathbf{r}_i$) to reduce the data misfit. The calculation time increases non-linearly with the finite-element mesh size and the number of data points and model parameters. In surveys using a mobile measuring system where the electrodes are on a streamer, the number of electrode positions, data points and model parameters can exceed more than a hundred thousand and the finite-element mesh used might have

1
2
3 more than one million nodes. The calculation of the apparent resistivity and Jacobian
4 matrix for each iteration can exceed a day on inexpensive PCs used by small
5 companies and institutions. The complete inversion of a data set might take more than
6 a week using standard techniques. To reduce the calculation time, we use a ‘divide
7 and conquer’ strategy that subdivides the mesh in a number of smaller meshes
8 (Christiansen and Auken 2004; Loke and Lane 2004).
9

10
11
12
13
14
15
16
17 Another computational problem is the size of the Jacobian matrix \mathbf{J} and the time
18 taken to solve the least-squares equation (1). The \mathbf{J} matrix has n times m array
19 elements, where n is the number of data points and m is the number of model
20 parameters. As an example, a data set with 200,000 data points and a model with
21 150,000 model cells will have a Jacobian matrix with 30,000,000,000 array values. To
22 solve the least-squares equation for such large matrices, the linear conjugate-gradient
23 method together with a data compression technique (using wavelet transforms) is
24 commonly used (Li and Oldenburg 2003; Davis and Li 2013). The inverse models
25 used in this research have a simple arrangement with the model cells arranged in a 3-
26 D rectangular pattern. We describe a simple technique to optimise the wavelet
27 transform method for the model structure used in this research.
28
29
30
31
32
33
34
35
36
37
38
39
40
41
42
43
44
45
46

47 **METHODS TO REDUCE COMPUTER TIME AND MEMORY**

48
49 In this section, we described various methods used to reduce the computer time
50 and memory required for the inversion of very large data sets with hundreds of
51 thousands of electrode positions and data points. The calculations were carried out
52 using a PC with an 18-core Intel W-2195 CPU and 256 GB of RAM.
53
54
55
56
57
58
59
60

Mesh segmentation

Surveys conducted with a mobile resistivity meter system are characterised by arrays having a limited footprint that is proportional to the length of the streamer. Figure 1 shows a schematic diagram of a streamer cable for a 10-channel resistivity meter system using a dipole-dipole arrangement. If the unit electrode spacing is 1 m, the furthest distance between a current and potential electrode is 12 m. The footprint of the system (Tsourlos *et al.* 2014) can be much smaller than the survey area which might be several hundred meters in length. Unlike a survey with a static resistivity meter system, where an array can have electrodes that extend across the entire survey line, the region of the subsurface that affects a measurement using a cable of limited length has a more limited lateral extent compared to the total length of the survey line. This property was previously used (Christiansen and Auken 2004; Loke and Lane 2004; Tsourlos *et al.* 2014) to reduce the calculation time for the inversion of data from long 2-D survey lines. We note that in some surveys a larger spacing might be used between the potential electrodes towards the end of the streamer (such as between electrodes P9 to P11 in Figure 1) to obtain a stronger signal strength. However, the footprint of the system is still limited by the maximum length of the cable. We extend the segmentation technique to 3-D surveys.

As an example, Figure 2 shows the algorithm used to subdivide a rectangular model grid with 160 by 45 cells in the x and y directions. In the first step (Figure 2a), the model grid is subdivided in 6 approximately equal segments. Next, we mark the data points with at least one electrode in segment 1. The electrode arrays near the boundaries of the segment are likely to have one or more electrodes outside the segment. The boundaries of the segment are next extended (Figure 2b) so that it covers all the electrodes that are used by data points marked earlier. In this example,

1
2
3 the measurements are only made in the x direction, so only the x boundary is
4 extended. In surveys with measurements in the y direction, the y boundary is similarly
5 extended. In the final step, the boundaries in both the x and y directions are extended
6 by 5 model grid lines (Figure 2c) so that the effect of model cells near edges of the
7 segment are included in the calculation of the apparent resistivity and Jacobian matrix
8 values for the data points that were marked for this segment. Next, the same
9 procedure is used for segment 2 (Figure 2a). The data points that were marked for
10 segment 1 are removed from the data set used for determining the data points that fall
11 within segment 2 (as well as other segments). Next the boundaries for the remaining
12 segments are set one by one using the same procedure. Note this procedure allocates a
13 data point to only one segment in the calculation of the apparent resistivity and
14 Jacobian matrix values. Figure 3a shows the final boundaries of the 6 segments. There
15 is an overlap of 10 model grid lines at the boundaries of the neighbouring segments.
16 The overlap minimises discontinuities in the calculated apparent resistivity and
17 Jacobian matrix values near the boundaries.

18
19 To avoid the build-up of artefacts near the edges of the segments, the
20 boundaries of the segments are changed after each iteration. In the second iteration of
21 the least-squares optimisation method (Figure 3b), the boundaries for segment 1 are
22 pushed forward in the x and y directions by 3 model grid lines. At the same time, the
23 lower y boundary for segment 2 is pushed upwards in the y direction by 3 model grid
24 lines. In the same way, the left x boundary for segment 3 is moved to the right by 3
25 model grid lines. In the third iteration (Figure 3c), the boundaries for segment 1 are
26 pushed backwards in the x and y directions by 3 model grid lines from the positions in
27 the first iteration. In the fourth iteration, the boundaries in the first iteration are used.
28 The algorithm uses the alternating positions of the boundaries in a cyclic manner.

1
2
3 The segmentation algorithm extends the final boundaries of the segments by at
4
5 least 5 model grid lines. The widths of the model cells are usually set to be the same
6
7 as the minimum distance between adjacent electrodes in the streamer. Extending the
8
9 boundaries to a larger distance should increase the accuracy of the model obtained by
10
11 the segmentation method (compared to a normal single mesh inversion) but at the cost
12
13 of larger computer memory and time. To estimate the optimum distance to extend the
14
15 boundary, we first examine the sensitivity values for a dipole-dipole array survey
16
17 similar to that used in the synthetic model and field survey discussed in this paper.
18
19 Figure 4a shows a 3-D plot of the sensitivity values (Fréchet derivative) for a dipole-
20
21 dipole array with $a=1$ m and $n=10$ for a homogeneous medium that can be calculated
22
23 analytically (Loke and Barker 1996). The regions with the highest sensitivity values
24
25 are located near the electrodes. The isosurface plot shows the regions with significant
26
27 sensitivity values are located near the dipoles and elongated in the direction
28
29 perpendicular to the axis of the array. Figure 4a shows the model sensitivity
30
31 distribution for a single array. To study the characteristics of a data set that consists of
32
33 many arrays, the model resolution is used (Loke *et al.* 2014b). The resolution value of
34
35 a model cell is limited to between 0.0 (no resolution) to 1.0 (perfect resolution). We
36
37 calculate the resolution values for a data set from a survey grid with 64 by 23
38
39 electrodes (Figure 4b), with all the possible dipole-dipole measurements with $a=1$ m
40
41 and $n=1$ to 10 in the x -direction only (giving a total of 12995 data points). The survey
42
43 grid and number of electrodes is similar to a single segment in Figure 2. Figure 4b
44
45 shows a 3-D plot of the resolution values. The subsurface is divided into uniform cells
46
47 with dimensions of $1.0 \times 1.0 \times 0.5$ m. The maximum resolution value at the surface near
48
49 the centre of the survey grid is about 0.84. The resolution values gradually decrease
50
51 with increasing distance from the edge of the survey grid. The band with significant
52
53
54
55
56
57
58
59
60

1
2
3 resolution values is wider at the y boundaries compared to the x boundaries. This is
4
5 because the measurements are only made in the x direction, and the zone with higher
6
7 sensitivity values are elongated in the direction perpendicular to the array axis. Figure
8
9 4c shows the change in the resolution values at the x and y boundaries with distance
10
11 from the boundaries. For the y boundary, the cell at the surface immediately next to
12
13 the boundary has significant resolution value of 0.76. The resolution rapidly decreases
14
15 with distance to about 0.002 at 4.5 m. So, extending the segment boundary up to 5
16
17 times the unit electrode spacing should include all the regions with significant
18
19 resolution values. Figure 4c also shows that the resolution values are lower at the x
20
21 boundary, and also decreases with depth. Field data sets sometimes have
22
23 measurements in both directions, so the boundary is normally extended by the same
24
25 distance in both directions. Most conventional arrays have sensitivity patterns that do
26
27 not extend as far out as the dipole-dipole array (Loke *et al.* 2014b). So, extending the
28
29 segment boundaries to about 5 times the unit electrode spacing is a conservative
30
31 approach that should cover most field surveys situations.
32
33
34
35
36

37
38 The time and taken by the finite-element method increases nonlinearly with
39
40 the number of nodes in the mesh (Christiansen and Auken 2004; Loke and Lane
41
42 2004). Calculating the apparent resistivity values for all the data points using a
43
44 number of smaller sub-meshes takes less time than using a single large mesh for very
45
46 large models that might have more than a million nodes. Another benefit of using
47
48 segments is the reduction in the calculation of the Jacobian matrix values. In the
49
50 standard monolithic inversion approach, the sensitivity values for all the model cells
51
52 are calculated for each data point. In the segmented inversion approach, the sensitivity
53
54 values for only the model cells that fall within the segment are calculated for each
55
56 data point. The average number of model cells in a segment for the grid in Figure 3a
57
58
59
60

1
2
3 is 14960 which is about 26% of the entire model with 57600 cells (with 10 layers).
4
5 For larger model grids, with grid sizes much larger than the overlap between adjacent
6
7 segments, the Jacobian matrix calculation time is usually reduced to about 20%
8
9 compared to the standard single mesh inversion method.
10
11
12
13

14 **Optimising the Jacobian matrix computations for multi-channel systems**

15
16
17 The Jacobian matrix is frequently calculated using the adjoint-equation
18
19 method for resistivity problems (Sasaki 1989; McGillivray and Oldenburg 1990).
20
21 Many modern resistivity meter systems have multi-channel capability where a number
22
23 of simultaneous potential measurements are made for a single injection of the current.
24
25 As an example, the arrangement in Figure 1 makes 10 measurements using the same
26
27 C1-C2 current dipole. This feature can be used to reduce the numerical calculations
28
29 required by the adjoint-equation method to calculate the sensitivity values for the 10
30
31 data points that share the same current electrodes positions. The finite-element
32
33 method is commonly used to calculate the apparent resistivity values for surveys over
34
35 areas with topography (Loke 2000). The potentials are calculated by solving the
36
37 following capacitance matrix equation (Sasaki 1989; Silvester and Ferrari 1990; Loke
38
39 *et al.* 2018).
40
41
42
43

$$44 \quad \mathbf{C}\Phi = \mathbf{s} \quad (2)$$

45
46
47 Φ is a vector that contains the potentials at the nodes of the finite-element grid while \mathbf{s}
48
49 is the current source vector. \mathbf{C} is the capacitance matrix that contains the positions of
50
51 the nodes and the model conductivity values. Figures 5a and 5c show the quadrilateral
52
53 and hexahedral elements used for 2-D and 3-D models. For the following discussion,
54
55 we use the 2-D mesh (Figure 5b) as an example as the matrix structure (Figure 5d) is
56
57
58
59
60

easier to visualise. However, the matrix equations for both the 2-D and 3-D finite-element methods are essentially the same.

Differentiating the capacitance matrix equation (2) with respect to the model cell conductivity σ_k leads to the following relationship.

$$\mathbf{C} \frac{\partial \Phi}{\partial \sigma_k} = - \frac{\partial \mathbf{C}}{\partial \sigma_k} \Phi \quad (3)$$

This equation has the same form as equation (2). All the information required to calculate the sensitivity $\frac{\partial \Phi}{\partial \sigma_k}$ is available in the process of solving equation (2) to calculate the potentials. The matrix $\frac{\partial \mathbf{C}}{\partial \sigma_k}$ is very sparse with only 16 non-zero terms for a 2-D trapezoidal element (Figure 5d). The terms in the capacitance matrix \mathbf{C} consists of the coupling coefficients between the nodes in each element in the mesh (Silvester and Ferrari 1990) and the conductivity of the element. The coupling coefficient between two nodes in an element (Figure 5a) has the following form.

$$c_{pq} = d_{pq}(x, z) \sigma_k \quad (4)$$

The function $d_{pq}(x, z)$ depends only on the coordinates of the four nodes at the corners of the trapezoidal element. The derivative of the coupling coefficient with respect to the element conductivity is thus given by

$$\frac{\partial c_{pq}}{\partial \sigma_k} = d_{pq}(x, z). \quad (5)$$

As the $d_{pq}(x, z)$ terms are calculated in the process of constructing the capacitance matrix \mathbf{C} in equation (2), so it is not necessary to recalculate them for the $\frac{\partial \mathbf{C}}{\partial \sigma_k}$ matrix. In terms of computer program implementation, calculating a member of the $\frac{\partial \Phi}{\partial \sigma_k}$ vector, basically involves the multiplication of a 4 by 4 non-zero sub-matrix

(containing the d_{pq} terms for the mesh element) by the potentials (Φ) at the nodes due to current sources located at the positions of the current electrodes used in the measurement (Figure 5d). This is represented by the following equation.

$$\mathbf{e} = \frac{\partial \mathbf{C}}{\partial \sigma_k} \Phi \quad (6)$$

This produces a vector (\mathbf{e}) with 4 non-zero values that is in turn multiplied by the potentials at the nodes due to current sources located at the positions of the potential electrodes. The calculation of the \mathbf{e} vector requires 16 multiply-add operations for a 2-D quadrilateral element. In total 20 multiply-add operations are required for each mesh element.

For a 3-D hexahedral element, calculating the \mathbf{e} vector involves the multiplication of an 8 by 8 non-zero sub-matrix with a vector which requires 64 multiply-add operations. It is then followed by 8 multiply-add operations to add the potentials at the 8 nodes of the element due to current sources at the potential electrodes giving a total of 72 multiply-add operations. We note that for both the 2-D and 3-D problems, the most time-consuming part is in the calculation of the \mathbf{e} vector in equation (6).

However, the \mathbf{e} vector only involves the current electrodes and is independent of the position of the potential electrodes used in a measurement. If there is a series of measurements that use the same positions of the current electrodes, it is only necessary to calculate the \mathbf{e} vector once and store the values in a temporary array in the computer memory. The temporary array is then used to calculate the Jacobian matrix values for subsequent measurements that use the same current electrodes. As an example, the electrodes arrangement in Figure 1 uses the same C1-C2 current dipole for 10 different measurements. Thus, it is only necessary to directly calculate

1
2
3 the \mathbf{e} vector for the first measurement that uses the C1-C2-P1-P2 electrodes. For the 9
4 subsequent data points (using the C1-C2-P2-P3 until C1-C2-P10-P11 configurations)
5
6 it is not necessary to directly calculate the \mathbf{e} vector which can be retrieved from the
7
8 computer memory. This means that while the calculation of the sensitivity value for
9
10 the first measurement requires 72 multiply-add operations, the sensitivity values for
11
12 the 9 subsequent measurements require only 8 multiply-add operations each. This
13
14 reduces the total number of multiply-add operations for the 10 data points from 720 to
15
16 144 which reduces the calculation time by about 80% for 3-D problems.
17
18
19
20

21 It was noted by Loke *et al.* (2015) in the study of optimised arrays that for
22 some data sets the number of independent current-potential (C-P) pairs can be much
23 less than the number of data points. This was used to greatly reduce the calculation
24 time to generate the optimised arrays. The same technique can be used to further
25 reduce the calculation time for the Jacobian matrix for data sets where the number of
26 unique C-P pairs is much less than the number of data points. However, the benefit of
27 using this technique is highly data dependent. For surveys that use the same current
28 electrodes for a large number of data points (Blome *et al.* 2011) using a resistivity
29 meter with a large number of channels this can be highly beneficial. For some data
30 sets, such as those using the Wenner array or the Lambayanna field data set
31 (following section), it can be slower. The expected reduction (or increase) in
32 computer time using this technique can be estimated by calculating the number of
33 unique C-P pairs versus the number of data points.
34
35
36
37
38
39
40
41
42
43
44
45
46
47
48
49
50

51 These techniques to reduce the Jacobian matrix calculation time for parallel
52 measurements are general in nature and can also be used for standard inversion using
53 a single mesh, as well as for other geophysical methods such as EM surveys that use a
54 number of receivers for a single source position.
55
56
57
58
59
60

1
2
3 The calculation of the Jacobian matrix requires the largest amount of computer
4 memory during the inversion process. If the number of electrodes used in the survey
5 is n_e and the number of nodes in the mesh is n_m , the total number of potential values is
6 $n_e \cdot n_m$. The synthetic model example used in this paper (following section) has 7406
7 electrodes and the finite-element mesh has 811,980 nodes. If the potentials are stored
8 as 4-byte single precision values, the computer memory needed to store all the
9 potential values is 22.4 GB. If the mesh is divided into 6 segments, the average
10 number of electrodes and nodes in a segment are 1,418 and 267,320 respectively.
11 Thus, the average amount of computer memory required by the segmentation method
12 is about 1.4 GB which is 6.3% of that used by the standard monolithic approach. If
13 the computer memory available is less than that required, it is still possible to
14 calculate the Jacobian values by reading the potential values associated with the 4
15 electrodes used for each data point from the computer hard-disk when required.
16 However, this is much slower than loading all the potential values into the computer
17 memory where they can be accessed more rapidly.
18
19
20
21
22
23
24
25
26
27
28
29
30
31
32
33
34
35
36
37
38
39

40 **Reducing the computer time and memory to solve the least-squares equation**

41
42 The Jacobian matrix \mathbf{J} encountered for large surveys with hundreds of
43 thousands of data points and model cells can have billions of array values. For such
44 large scale problems, the iterative linear conjugate-gradient method is commonly used
45 to solve the least-squares equation (1) to determine the change in the model
46 parameters $\Delta \mathbf{r}_i$. Solving the least-squares equation using the linear conjugate gradient
47 method involves matrix vector multiplications of the form $\mathbf{J}^T \mathbf{a}$ and $\mathbf{J} \mathbf{b}$. The size of the
48 Jacobian matrix presents two computational problems. The first involves the
49 computer time required for the matrix-vector multiplications. The second problem is
50
51
52
53
54
55
56
57
58
59
60

1
2
3 that the size of the Jacobian matrix might exceed the computer memory. Both
4
5 problems were solved by using the wavelet transform to compress the Jacobian matrix
6
7 by retaining only the components with significant amplitudes (Li and Oldenburg
8
9 2003; Davis and Li 2013). The arrangement of model cells used in this research has a
10
11 simple 3-D rectangular pattern (Figure 5) so a simple algorithm can be used to
12
13 optimise the use of the wavelet transform. The sensitivity values associated with an
14
15 electrode measurement configuration is a 3-D function of the (x,y,z) coordinates of the
16
17 model cells. We take advantage of the regular arrangement of the model cells, and the
18
19 property that sensitivity values change in a smooth manner between neighbouring
20
21 cells, to convert the 3-D sensitivity function to a 1-D function of the cell index
22
23 number (Figure 6) so that a simple 1-D wavelet transform can be used. As an
24
25 example, Figure 7a shows the Jacobian vector for a single pole-dipole array on the
26
27 surface of a model with a 15 by 15 m rectangular grid and 7 layers plotted as a 1-D
28
29 function of the cell index number. The Jacobian vector has the largest amplitudes at
30
31 the model cells that are closest to the electrodes, with the amplitudes decreasing with
32
33 each deeper layer. The shift in the position of the sensitivity pattern between layers is
34
35 due to the zigzag model cell numbering scheme used (Figure 6). The fast wavelet
36
37 transform using the Daubechies 4 wavelet (Daubechies 1988; Press *et al.* 2007) was
38
39 used to calculate the wavelet components (Appendix). The wavelet components plot
40
41 (Figure 7d) shows that most of them have very small amplitudes. If components with
42
43 amplitudes of less than 0.5% of the largest are removed, the reconstructed sensitivity
44
45 (using the inverse wavelet transform) plot still closely matches the original plot
46
47 (Figures 7a and 7b). Figure 7c shows a plot of the difference between the original and
48
49 reconstructed Jacobian values. Note the vertical scale used for this plot is 100 times
50
51 smaller compared to Figures 7a and 7b. If the same scale is used, the plot will appear
52
53
54
55
56
57
58
59
60

1
2
3 as a flat line. The maximum amplitude of the difference is about 200 times smaller (or
4
5 0.5%) than the maximum Jacobian value.
6
7

8 For very large models with hundreds of thousands of model cells, the 1-D
9
10 wavelet transform reduces the size of the Jacobian matrix by more than 100 times. As
11
12 an example, the Jacobian matrix for the Lambayanna field data set (following section)
13
14 has 69,464,915,000 elements, or about 259 GB of computer memory (using a 4-byte
15
16 single precision array) which exceeds the memory of the PC used. This was reduced
17
18 to 139,579,108 values if only the wavelet components with amplitudes that exceed
19
20 0.5% of the maximum amplitude are retained. This is nearly 500 times smaller than
21
22 the full Jacobian matrix. The computer memory required is slightly over 1 GB
23
24 (including an auxiliary 4-byte integer array with the index values of the retained
25
26 wavelet components). The time taken by the fast wavelet transform and to solve the
27
28 least-squares equation using the sparse transformed Jacobian matrix is less than 10%
29
30 of the time taken by the finite-element routine to calculate the potentials and Jacobian
31
32 matrix values.
33
34
35
36
37
38
39
40
41

42 **RESULTS**

43 44 45 **Synthetic model test**

46
47 We use a synthetic model with 8 blocks embedded in the upper layer of a two-
48
49 layer medium (Figure 8). The electrodes are arranged in a 1610 by 460 m rectangular
50
51 grid with a 10 m spacing in both the x and y directions for a total of 7,406 electrodes
52
53 (Figure 2). The test data set consists of the dipole-dipole array measurements with the
54
55 dipole length $a=10$ m, and dipole spacing values n of 1 to 10 with only measurements
56
57
58
59
60

made in the x -direction. This gave a data set with 70,610 measurements while the inverse model with 10 layers has 57,600 cells. The main purpose of the synthetic data set is to check the accuracy of the segmentation inversion algorithm compared to the standard single mesh inversion. Gaussian random noise with an amplitude of 0.05 m Ω was added to the calculated resistance values (with a range of 0.54 to 355.18 m Ω) before they were converted to apparent resistivity values (Zhou and Dahlin 2003). This resulted in an average noise level of about 1.5% in the apparent resistivity values. The mesh was divided into 6 segments with the boundaries cutting across blocks 1, 3, 6, 7 and 8.

Figure 9a shows the inverse model using the standard inversion method with a single mesh that has a data misfit of 1.5%, which is the same as the added noise. The inverse model using the segmented mesh (Figure 9b) is nearly identical to that obtained with a single mesh and has the same data misfit. The edges of the segments were extended by 5 cells in both the x and y directions. In algorithms that do not calculate the Jacobian values for all model cells for each data point (Christiansen and Auken 2004; Loke and Lane 2004; Papadopoulos *et al.* 2011), the Jacobian values that are not directly calculated are normally set to zero in advance omitting their respective calculation. In this paper, we also test the results when the Jacobian values for these cells are approximated by using the values for a homogeneous half-space that can be calculated analytically (Loke and Barker 1996).

To numerically assess the accuracy of the segmented mesh model, the percentage relative difference at cell j between the resistivity of the models using standard monolithic (r_1) and segmented mesh (r_2) inversions was calculated using the following equation.

$$\partial(j) = 100 \cdot [r_2(j) - r_1(j)] / r_1(j) \quad (7)$$

The average percentage relative difference (∂_a) was then calculated using the following equation.

$$\partial_a = \left[\sum_1^m |\partial(j)| \right] / m \quad (8)$$

m is the number of model cells. The average difference between the model resistivity values obtained using the segmentation algorithm and normal monolithic inversion is 0.2% (Table 1). The maximum difference of 1.8% occurs in Layer 9 (not shown) which is probably due to the decrease in resolution with depth. There are no visible artefacts where the segment boundaries cut across the blocks in the upper layer. We also carried out an inversion with the fixed segment boundaries (instead of changing the boundaries after each iteration). The resulting model resistivity values also had an average difference of 0.2% but the maximum difference was higher at 2.4%.

Figure 9c shows the inverse model using the segmentation algorithm with the Jacobian values for the cells outside the segments truncated to zero. The average difference in the model values is essentially the same as for Figure 9b (to within 0.05%) but the maximum difference is slightly higher at 2.3%. For the final test, the width of the buffer zone at the edges of the segments was extended to 8 model cells with the Jacobian values outside the segments also truncated to zero (Figure 9d). This gave a maximum difference of 1.6% that is marginally lower (Table 1) compared to that obtained using a buffer zone of 5 model cells and a homogeneous model Jacobian approximation for the external cells.

We note that the models using the segmentation algorithm are visually identical to that obtained using standard monolithic inversion. The average difference of about 0.2% in the model resistivity values is small compared to the noise level of 1.5% added to the data. Padding the Jacobian matrix with approximate values from a

1
2
3 homogeneous half-space does result in a slightly lower maximum difference when a
4 narrower buffer zone is used. In cases where the approximate Jacobian is not suitable
5 and the values are truncated to zero, using a wider buffer zone gave similar results at a
6 cost of a slight increase in computer time (Table 1).
7
8
9
10
11

12 The different implementations of the segmentation algorithm reduce the
13 calculation time by about 30% to 40% (Table 1). This is a relatively small data set
14 with 7,406 electrodes, 70,610 data points and 57,600 model cells. There is a
15 significant overlap between the different segments compared to the overall model grid
16 size so the reduction in the computer time is relatively modest compared to larger data
17 sets.
18
19
20
21
22
23
24
25
26
27

28 **Lambayanna field survey data set**

29
30 Figure 10a shows the layout from a survey in a prehistoric submerged
31 archaeological site in central Greece using a mobile streamer dragged along the sea
32 bottom below the sea surface in a depth ranging from 0.9 m to 5.3 m and an average
33 depth of 2.7 m (Oikonomou *et al.* 2019). The dipole-dipole array with dipole length a
34 = 1 m and n values from 1 to 10 was used. There are 215,875 electrode positions and
35 164,414 data points in this data set. The survey lines, inverse model grid and
36 segments used are shown in Figure 10b. Many of the survey lines crisscross each
37 other such that several electrodes from different survey lines are located close to one
38 another. In cases where the electrode does not coincide with a node in the finite-
39 element mesh, an interpolation method is used (Spitzer *et al.* 1999; Loke *et al.*
40 2013b). The potential at the position of the electrode is estimated from the potentials
41 at the four nearest nodes in the mesh (and similarly a current electrode is replaced by
42 four equivalent current sources). The top 5 levels of the finite-element mesh are used
43
44
45
46
47
48
49
50
51
52
53
54
55
56
57
58
59
60

1
2
3 to model the water layer where the resistivities of the cells are fixed using the
4 measured seawater value of $0.17 \Omega\text{m}$ (Dahlin and Loke 2018). The z position of the
5
6 5th node from the top of the mesh is set at the measured depth of the seabed at the
7
8 particular (x,y) position.
9
10

11
12 The model grid used for the data inversion has 131 by 326 cells with widths of
13
14 1 m in both the x and y directions and 10 layers giving a total of 422,500 model cells.
15
16 The thickness of the first layer is set at the minimum depth of investigation (Edwards
17
18 1977) of the data set. The thickness of each deeper layer is increased by 15% since the
19
20 data resolution decreases with depth. The maximum depth of investigation of the data
21
22 set is used as a guide to set the depth to the bottom layer. Figure 11a shows the top 6
23
24 layers of the model with the standard monolithic inversion approach using a single
25
26 finite-element mesh with 9,675,548 nodes. The mesh has 419, 1004 and 23 nodes
27
28 respectively in the x , y and z directions. Out of the 23 nodes in the z direction, 5
29
30 nodes are used to model the water layer while 7 nodes are used for the bottom section
31
32 of the mesh below the last model layer. The spacing between the 7 bottom mesh lines
33
34 are progressively increased so that the last mesh line is sufficiently far away from the
35
36 electrodes (Dey and Morrison 1979). The remaining 11 nodes are used for the 10
37
38 model layers with the top layer (which is closest to the electrodes) subdivided in two
39
40 mesh lines. Figure 12 shows a 3-D plot of the model for the sediments below the
41
42 water layer. As the water layer resistivity is fixed, it is not shown in the model plots.
43
44 The archaeological features of interest are represented by the higher resistivity
45
46 anomalies on the left side of the sections (that is located further from the shoreline) in
47
48 the top 3 layers. The inversion took about 327,777 seconds (91.0 hours). The data
49
50 misfit of 10.8% is higher than most land surveys using a conventional 'static' multi-
51
52 electrode resistivity meter system with the electrodes planted in the ground. This is
53
54
55
56
57
58
59
60

1
2
3 probably partly due to the challenging marine environment with very conductive
4 seawater and the continuous movement of the cable during the survey. Nevertheless,
5 the resistivity model agrees with known archaeological information and the results
6 from other geophysical surveys (Oikonomou *et al.* 2019).
7
8
9

10
11
12 Figure 11b shows the model obtained using the segmentation algorithm with 8
13 segments. A buffer zone with 8 model cells was used for the segments. It was
14 observed that the sensitivity values for model cells outside the segments calculated
15 using the adjoint equation method (from the single mesh inversion) differ
16 significantly from approximate values using a homogeneous model. This is probably
17 because of the large contrast between the seawater and the subsurface materials. The
18 Jacobian values for the cells outside the segments were thus truncated to zero in the
19 inversion process, and a wider buffer zone was used for the segments. There are no
20 significant differences in the models using the standard monolithic and segmentation
21 inverse method (Figures 11a and 11b) that also has a data misfit of 10.8%. The
22 average difference in the model resistivity values is 0.7%. The maximum difference
23 of 3.9% occurred for a cell in the 9th layer which is probably due to the decrease in the
24 resolution with depth. The calculation time was 52,731 seconds (14.6 hours), or a
25 reduction of about 84% compared to the standard approach. The average number of
26 model cells in a segment is 78,485 (about 19% of the whole model).
27
28
29
30
31
32
33
34
35
36
37
38
39
40
41
42
43
44
45

46
47 We also carry out a test with an alternative approach where the positions of the
48 electrodes were rounded up (Oikonomou *et al.* 2019), or binned, to the nearest 0.5 m
49 (i.e. half the electrode spacing). This reduced the number of electrode positions to
50 87,245 (about 40% of the original data set). An inversion of the data set with the
51 modified electrode positions was carried out using the normal approach with a single
52 finite-element mesh. Figure 11c shows the inverse model which is fairly similar to
53
54
55
56
57
58
59
60

1
2
3 that obtained using the electrodes in their true positions (Figure 11a) with a slightly
4 higher data misfit of 10.9%. The average relative difference in the model values was
5 slightly higher at 1.1% compared to the segmentation method. The largest differences
6 were found in the top layer. A relatively high maximum difference of 46.6% was
7 obtained for a cell in the top layer. This was probably caused by arrays where the
8 electrodes are not equally spaced due to bending of the cable during the survey.
9 Consequently, the electrodes in some configurations were shifted by different
10 amounts with the binning procedure. This resulted in significant changes in the
11 characteristics of the electrode array compared to the true configuration. The binning
12 procedure reduced the calculation time by about 51% which is less than that obtained
13 with the segmentation method.
14
15
16
17
18
19
20
21
22
23
24
25
26
27
28
29
30
31
32

33 **DISCUSSION**

34
35 The use of segments to reduce the calculation time is designed for the
36 inversion of very large data sets with limited computational resources. This situation
37 is frequently encountered by small geophysical companies using personal computers
38 or workstations. In general, a conservative approach is followed that uses the
39 minimum number of segments so that the inversion can be carried out with the
40 available computer resources. It is recommended that the length of a segment should
41 not be less than 5 times the length of the streamer for arrays aligned along the same
42 direction as the side of the segment. As an example, in Figure 11 most of the
43 measurements are in the y -direction using a streamer of 12 metres. Thus, the length of
44 the segments in the y -direction should be at least 60 metres. It is also recommended
45 that the length of a segment in one direction should be not be more than twice the
46
47
48
49
50
51
52
53
54
55
56
57
58
59
60

1
2
3 length in the other direction. However, the size and number of segments that provides
4
5 an optimum balance between reducing the calculation time and accuracy of the results
6
7
8 is an area that requires further research.
9

10 11 12 13 14 **CONCLUSIONS**

15
16
17 Surveys using mobile systems can produce very large data sets with hundreds
18
19 of thousands of electrode positions and data points. The model used can have
20
21 hundreds of thousands of cells with a finite-element mesh of more than one million
22
23 nodes. The segmentation method has proved to be an effective method that reduces
24
25 the calculation time by more than 80% for very large data sets while producing
26
27 models with an average difference of less than 1% from that produced by the standard
28
29 monolithic approach. An alternative method, binning the electrodes to discrete
30
31 positions, has the advantage that it is relatively easy to implement. However, in field
32
33 data sets from mobile surveys where bending of the cable is common, this can cause
34
35 larger errors in parts of the inverse model (particularly near the surface) compared to
36
37 the segmentation method. The segmentation method is faster but more difficult to
38
39 implement. It has been used successfully for surveys with more than half a million
40
41 electrode positions (Unrau 2019). This makes it practical to carry out the inversion of
42
43 very large data sets on common and inexpensive microcomputers used by small
44
45 companies and institutions.
46
47
48
49

50
51 We are currently investigating other techniques to further reduce the
52
53 calculation time such as directly calculating the Jacobian values at selected cells
54
55 within a segment that are likely to have significant amplitudes (Papadopoulos *et al.*
56
57 2011) and using a homogeneous model approximation for the rest. We are also
58
59
60

1
2
3 examining ways to adapt the techniques described in Yang *et al.* (2014), such as the
4 use of local meshes and data subsets, to further reduce the computer time and memory
5 required to process very large resistivity data sets.
6
7
8
9
10
11
12
13

14 **ACKNOWLEDGEMENTS**

15
16 The authors from GeoSat ReSeArch lab express their acknowledgements to Dr. Julien
17 Beck for the fruitful and constructive collaboration in the 2016-2019 during the
18 archaeological project in the Bay of Kiladha which a collaboration between the
19 University of Geneva, under the aegis of the Swiss School of Archaeology in Greece,
20 and the Greek Ephorate of Underwater Antiquities. Wilkinson publishes with the
21 permission of the Executive Director, British Geological Survey (UKRI-NERC). We
22 would like to thank two anonymous reviewers and the Associate Editor for their
23 constructive comments that have helped to improve the paper.
24
25
26
27
28
29
30
31
32
33
34
35
36
37
38
39

40 **References**

- 41
42 Blome, M., Maurer, H. & Greenhalgh, S., 2011. Geoelectric experimental design -
43 Efficient acquisition and exploitation of complete pole-bipole data sets.
44 *Geophysics*, **76**, F15–F26.
45
46
47
48
49 Christiansen A.V., and Auken E., 2004. Optimizing a layered and laterally
50 constrained 2D inversion of resistivity data using Broyden's update and 1D
51 derivatives. *Journal of Applied Geophysics*, **56**, 247-262.
52
53
54
55
56
57
58
59
60

- 1
2
3 Dahlin, T. and Loke, M.H., 2018. Underwater ERT surveying in water with resistivity
4 layering with example of application to site investigation for a rock tunnel in
5 central Stockholm. *Near Surface Geophysics*, **16**, 230-237.
6
7
8
9
10 Daubechies I., 1988. Orthonormal bases of compactly supported wavelets. *Commun.*
11
12 *Pure Appl. Math.*, **41(7)**, 909–996.
13
14
15 Davis K. and Li K., 2013. Efficient 3D inversion of magnetic data via octree-mesh
16 discretization, space-filling curves, and wavelets. *Geophysics*, **78**, 1942-2156.
17
18
19 deGroot-Hedlin C. and Constable S., 1990. Occam's inversion to generate smooth,
20 two-dimensional models from magnetotelluric data. *Geophysics*, **55**, 1613-
21
22 1624.
23
24
25
26 Dey, A. & Morrison, H.F., 1979. Resistivity modeling for arbitrarily shaped three-
27 dimensional structures. *Geophysics*, **44**, 615–632.
28
29
30
31 Edwards L.S., 1977. A modified pseudosection for resistivity and induced-
32 polarization. *Geophysics*. **42**, 1020-1036.
33
34
35
36 Farquharson C.G. and Oldenburg D.W., 1998. Nonlinear inversion using general
37 measures of data misfit and model structure. *Geophysical Journal*
38 *International*, **134**, 213-227.
39
40
41
42 Farquharson C.G. and Oldenburg D.W., 2004. A comparison of automatic techniques
43 for estimating the regularization parameter in non-linear inverse problems.
44
45 *Geophysical Journal International*, **156**, 411-425.
46
47
48
49 Hildes D., Dziuba F. and Power M., 2005. Kimberlite Exploration Using a
50 Capacitive-Coupled Resistivity System. *Proceedings of 2005 CSEG National*
51 *Convention*, May 16-19 2005, Calgary, Canada, 393-395.
52
53
54
55
56 Kuras O., Beamish D., Meldrum P.I., and Ogilvy R.D., 2006. Fundamentals of the
57 capacitive resistivity technique. *Geophysics*, **71**, G135–G152.
58
59
60

- 1
2
3 Li, Y. and Oldenburg, D.W., 2000. 3-D inversion of induced polarization data.
4
5 *Geophysics*, **65**, 1931-1945.
6
7
8 Li Y. and Oldenburg D.W., 2003. Fast Inversion of large-scale magnetic data using
9
10 wavelet transforms and logarithmic barrier method. *Geophysical Journal*
11
12 *International*, **152**, 251 - 265.
13
14
15 Loke M.H. and Barker R.D., 1996. Practical techniques for 3D resistivity surveys and
16
17 data inversion. *Geophysical Prospecting*, **44**, 499-523.
18
19
20 Loke M.H., 2000. Topographic modelling in resistivity imaging inversion. 62nd
21
22 EAGE Conference & Technical Exhibition Extended Abstracts, D-2.
23
24
25 Loke M.H., Acworth I. and Dahlin T., 2003. A comparison of smooth and blocky
26
27 inversion methods in 2D electrical imaging surveys. *Exploration Geophysics*,
28
29 **34**, 182-187.
30
31
32 Loke M.H. and Lane J.W., 2004. Inversion of data from electrical resistivity imaging
33
34 surveys in water-covered areas. *Exploration Geophysics*, **35**, 266-271.
35
36
37 Loke M.H., Chambers J.E., Rucker D. F., Kuras O. and Wilkinson P. B., 2013a.
38
39 Recent developments in the direct-current geoelectrical imaging method.
40
41 *Journal of Applied Geophysics*, **95**, 135-156.
42
43
44 Loke, M.H., Frankcombe, K. and Rucker, D.F., 2013b. The inversion of data from
45
46 complex 3-D resistivity and I.P. surveys. 23rd International Geophysical
47
48 Conference and Exhibition, 11-14 August 2013 - Melbourne, Australia.
49
50
51 Loke M.H., Dahlin T. and Rucker D.F., 2014a. Smoothness-constrained time-lapse
52
53 inversion of data from 3-D resistivity surveys. *Near Surface Geophysics*, **12**,
54
55 5-24.
56
57
58
59
60

- 1
2
3 Loke, M.H., P. B. Wilkinson, P.B., Uhlemann, S.S., Chambers, J.E. and Oxby, L. S.,
4
5 2014b. Computation of optimized arrays for 3-D electrical imaging surveys.
6
7 Geophysical Journal International, **199**, 1751-1764
8
9
10 Loke M.H., Wilkinson P.B., Chambers J.E., Uhlemann S.S. and Sorensen J.P.R.,
11
12 2015. Optimized arrays for 2-D resistivity survey lines with a large number of
13
14 electrodes. *Journal of Applied Geophysics*, **112**, 136-146.
15
16
17 Loke M.H., Wilkinson P.B., Chambers J. E. and Meldrum P.I., 2018. Rapid inversion
18
19 of data from 2-D resistivity surveys with electrodes displacements.
20
21 *Geophysical Prospecting*, **66**, 579-594.
22
23
24 McGillivray P.R. and Oldenburg D.W. 1990. Methods for calculating fréchet
25
26 derivatives and sensitivities for the non-linear inverse problem : a comparative
27
28 study. *Geophysical Prospecting*, **38**, 499-524.
29
30
31 Oikonomou D., Papadopoulos N., Simyrdanis K., Cantoro G., Beck J. and Loke M.H.,
32
33 2019. Processing strategies for 3-D marine dynamic electrical resistivity
34
35 tomography data. 13th International Conference on Archaeological Prospection,
36
37 28 August to 1 September 2019, Sligo, Ireland.
38
39
40 Papadopoulos, N.G., Tsourlos P., Papazachos C., Tsokas G.N., Sarris A. and Kim
41
42 J.H., 2011. An algorithm for fast 3D inversion of surface electrical resistivity
43
44 tomography data: application on imaging buried antiquities. *Geophysical*
45
46 *Prospecting*, **59**, 557-575.
47
48
49 Press, W.H, Teukolsky, S.A., Vetterling, W.T. and Flannery, B.P., 2007. Numerical
50
51 Recipes: The Art of Scientific Computing (3rd Edition). Cambridge University
52
53 Press.
54
55
56 Rucker, D.F., Levitt, M.T. and Greenwood, W.J., 2009. Three-dimensional electrical
57
58 resistivity model of a nuclear waste disposal site. *Journal of Applied*
59
60

- 1
2
3 *Geophysics*, **69**, 150-164.
4
5
6 Rucker D.F. and Noonan G.E., 2013. Using marine resistivity to map geotechnical
7
8 properties: a case study in support of dredging the Panama Canal. *Near*
9
10 *Surface Geophysics*, **11**, 625-637.
11
12 Sasaki Y., 1989, Two-dimensional joint inversion of magnetotelluric and dipole-
13
14 dipole resistivity data. *Geophysics*, **54**, 254-262.
15
16
17 Silvester P.P. and Ferrari R.L., 1990. Finite elements for electrical engineers (2nd.
18
19 ed.). Cambridge University Press.
20
21
22 Simyrdanis K., Papadopoulos N., Kim J.H., Tsourlos P. and Moffat I., 2015.
23
24 Archaeological Investigations in the Shallow Seawater Environment with
25
26 Electrical Resistivity Tomography. *Journal of Near Surface Geophysics*,
27
28 *Integrated geophysical Investigations for Archaeology*. **13**, 601- 611.
29
30
31 Spitzer K., Chouteau M. and Boulanger O. 1999, Grid-independent electrode
32
33 positioning for 3D DC and IP forward modelling. Proc. 2nd. Internat. Sym. 3D
34
35 Electromagnetics, 189–192.
36
37
38 Tsourlos P., Papadopoulos N., Papazachos C., Yi M.Y. and Kim J.H., 2014. Efficient
39
40 2D inversion of long ERT sections. *Journal of Applied Geophysics*, **105**, 213-
41
42 224.
43
44
45 Unrau T., 2019. Towed Capacitively Coupled Resistivity Systems in Arctic
46
47 Exploration - Advances in Equipment Design and Handling of Very Large
48
49 Resistivity Surveys. AGU 100 Fall Meeting, San Francisco, 9-13 Dec. 2019,
50
51 NS22A-07.
52
53
54 Xu, T. and Dunbar, J.A., 2015. Binning method for mapping irregularly distributed
55
56 continuous resistivity profiling data onto a regular grid for 3-D inversion.
57
58 *Journal of Environmental and Engineering Geophysics*, **20**, 1-17.
59
60

1
2
3 Yang, D., Oldenburg, D.W. and Haber, E., 2014. 3-D inversion of airborne
4 electromagnetic data parallelized and accelerated by local mesh and adaptive
5 soundings. *Geophysical Journal International*, **196**, 1492–1507.
6
7

8
9
10 Zhou B. and Dahlin, T., 2003. Properties and effects of measurement errors on 2D
11 resistivity imaging surveying. *Near Surface Geophysics*, **1**, 105-117.
12
13
14

15 16 17 18 19 **Appendix : Using the Discrete Wavelet Transform**

20
21 This section describes the practical use of the Discrete Wavelet Transform (DWT).
22 While the Fast Fourier Transform (FFT) is based on the sine and cosine functions, the
23 DWT is based on the ‘mother wavelet’ function (Daubechies 1992). The sine and
24 cosine functions are localised in frequency (but not in space or time). In comparison,
25 the wavelet functions are localised both in frequency and space. This makes them
26 useful for functions such as the Jacobian data series (Figure 7a) that exhibit a quasi-
27 periodic structure over a limited interval near the electrodes. Press *et al.* (2007) gives
28 a description of the wavelet functions, together with wavelet filter coefficients and
29 computer code to carry out the wavelet transform. Like the FFT, the computer
30 implementation of the DWT is optimized for a data vector where the number of points
31 is an integer power of 2. The number of model cells for the example in Figure 7a is
32 1575. In calculating the DWT, the data series is extended to 2048 by padding the end
33 with zeros. The time taken by the DWT is proportional to $m.\log(m)$ where m is the
34 length of the data vector. The time taken by the DWT to calculate the transform for
35 the Jacobian matrix is only a few percent of the overall time taken to invert the data
36 set. It is in fact less than time taken to read the Jacobian values from (and write the
37 transformed values to) the computer hard-disk.
38
39
40
41
42
43
44
45
46
47
48
49
50
51
52
53
54
55
56
57
58
59
60

List of figure captions

Figure 1. Schematic diagram of a mobile streamer. C1 and C2 are the current electrodes while P1 to P11 are the potential electrodes.

Figure 2. Method used to subdivide a model with 160 by 45 cells (of 10 m width in the x and y directions) in each layer subdivided into 6 segments. (a) Initial subdivision into 6 segments of approximately equal size. The dark blue line marks the region covered by segment 1. (b) Extending the boundary (medium blue line) of segment 1 so that it includes all the electrodes for data points in this segment. (c) Adding a buffer zone around the segment to minimise edge effects. The final region covered by segment 1 is shown by the light blue line.

Figure 3. (a) The initial regions of the model grid covered by the 6 segments used in iteration 1 of the least-squares optimisation algorithm. Note the overlaps between neighbouring segments. (b) Shifting of the boundaries of the segments forwards by 3 model grid lines (compared to those used in iteration 1) in iteration 2. (c) Shifting of the boundaries of the segments backwards by 3 model grid lines (compared to those used in iteration 1) in iteration 3.

Figure 4. (a) 3-D plot of sensitivity values for the dipole-dipole array with $a=1$ m and $n=10$. The electrodes are located at x positions of 0, 1, 11 and 12 along the $y=0$ axis. The isosurface for sensitivity value of 0.01 is shown. (b) Plot of resolution values for a dipole-dipole array survey with $a=1$ m and $n=1$ to 10 with electrodes in a 64 by 23 grid. The 0.005 isosurface is shown. The electrodes are marked by black dots on the surface. (c) Change of resolution with distance from edge of survey grid at the x and y

1
2
3 boundaries. The resolution values of cells at the mid-point of the x and y boundaries
4
5 (which have the highest values) are shown.
6
7
8
9

10 Figure 5. (a) 2-D quadrilateral element with 4 nodes. (b) Example 2-D finite-element
11 mesh with node numbers. (c) 3-D hexahedral element with 8 nodes. (d) Schematic
12 diagram of the structure of the capacitance matrix equation for the 2-D mesh with the
13 non-zero elements. D represents a diagonal element while X represents a non-zero
14 off-diagonal element. The members of the $\frac{\partial \mathbf{C}}{\partial \sigma_k}$ matrix (due to a change in the
15 conductivity of the k mesh cell) that have non-zero values are marked in red.
16
17
18
19
20
21
22
23
24
25
26

27 Figure 6. Numbering of model cells arranged in a 3-D rectangular grid so that the
28 Jacobian matrix which is a 3-D function of (x,y,z) is converted to a continuous 1-D
29 function of the model cell index k .
30
31
32
33
34
35

36 Figure 7. (a) Plot of the Jacobian values for a single pole-dipole array ($a = 2, n = 1$)
37 for a model with $15 \times 15 \times 7$ model cells (each layer has 225 cells). (b) The
38 reconstructed Jacobian values after wavelet components with amplitudes of less than
39 0.5% of the maximum value were removed. (c) Plot of the difference between the
40 original and reconstructed Jacobian values. Note the vertical scale is 100 times
41 smaller than (a) and (b). (d) Plot of the wavelet components. Values in vertical axis in
42 the plots is are dimensionless. The horizontal axis is the model cell index number in
43 (a), (b) and (c), and the wavelet wave number in (d).
44
45
46
47
48
49
50
51
52
53
54
55

56 Figure 8. Synthetic model with 8 blocks in the upper layer of a two-layer medium.
57 The top layer (transparent in the plot) has a resistivity of $30 \Omega.m$ and a thickness of
58
59
60

1
2
3 23.2 m. Blocks 1 to 5 extend from the surface (0.0 m) to a depth of 5.0 m. The top of
4
5 blocks 6 to 8 is at 5.0 m while the bottom is at 10.5 m depth.
6
7
8
9

10 Figure 9. Inverse models of synthetic data set with (a) standard monolithic inversion,
11
12 (b) using 6 segments with buffer zone of 5 model cells and homogeneous Jacobian
13
14 approximation for external cells, (c) using segments with buffer zone of 5 model cells
15
16 and truncated Jacobian for external cells and (d) using segments with buffer zone of 8
17
18 model cells and truncated Jacobian for external cells. The blocks in the synthetic
19
20 model are shown by black outlines in the first 2 layers.
21
22
23
24
25

26 Figure 10. Lambayanna survey (a) map and (b) inverse model grid (segments shown
27
28 by coloured grid lines).
29
30
31
32

33 Figure 11. Lambayanna survey inverse models using (a) standard monolithic
34
35 inversion with a single mesh, (b) 2 by 4 segmented mesh and (c) electrodes binned to
36
37 every 0.5 m.
38
39
40
41

42 Figure 12. 3-D plot of Lambayanna survey inverse model below the water layer.
43
44
45
46
47
48
49
50
51
52
53
54
55
56
57
58
59
60

List of table captions

Table 1. Comparison of different methods for the inversion of the synthetic model data set. All the models have the same data misfit of 1.5%.

Table 2. Comparison of different methods for the inversion of the Lambayanna field data set.

Table 1. Comparison of different methods for the inversion of the synthetic model data set. All the models have the same data misfit of 1.5%.

Inverse method	Inversion Time (s)	% model difference Average (max)	Memory required by adjoint-equation method (GB)
Single mesh	3,449		22.4
Segments with homogeneous Jacobian approximation for external model cells	2,140	0.2 (1.8)	1.4
Segments with truncated Jacobian for external model cells	2,025	0.2 (2.3)	1.4
Segments with wider buffer zone and truncated Jacobian for external model cells	2,512	0.2 (1.6)	1.6

Table 2. Comparison of different methods for the inversion of the Lambayanna field data set.

Inverse method	Number of electrodes	Inversion Time (s)	% model difference Average (max)	Data misfit (%)
Single mesh	215,873	327,777		10.8
Segments with 8 m buffer zone	215,873	52,731	0.7 (3.9)	10.8
Single mesh with 0.5 m electrodes binning	87,245	159,656	1.1 (46.6)	10.9

1
2
3
4
5
6
7
8
9
10
11
12
13
14
15
16
17
18
19
20
21
22
23
24
25
26
27
28
29
30
31
32
33
34
35
36
37
38
39
40
41
42
43
44
45
46
47
48
49
50
51
52
53
54
55
56
57
58
59
60

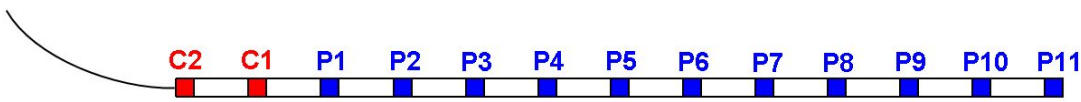


Figure 1. Schematic diagram of a mobile streamer. C1 and C2 are the current electrodes while P1 to P11 are the potential electrodes.

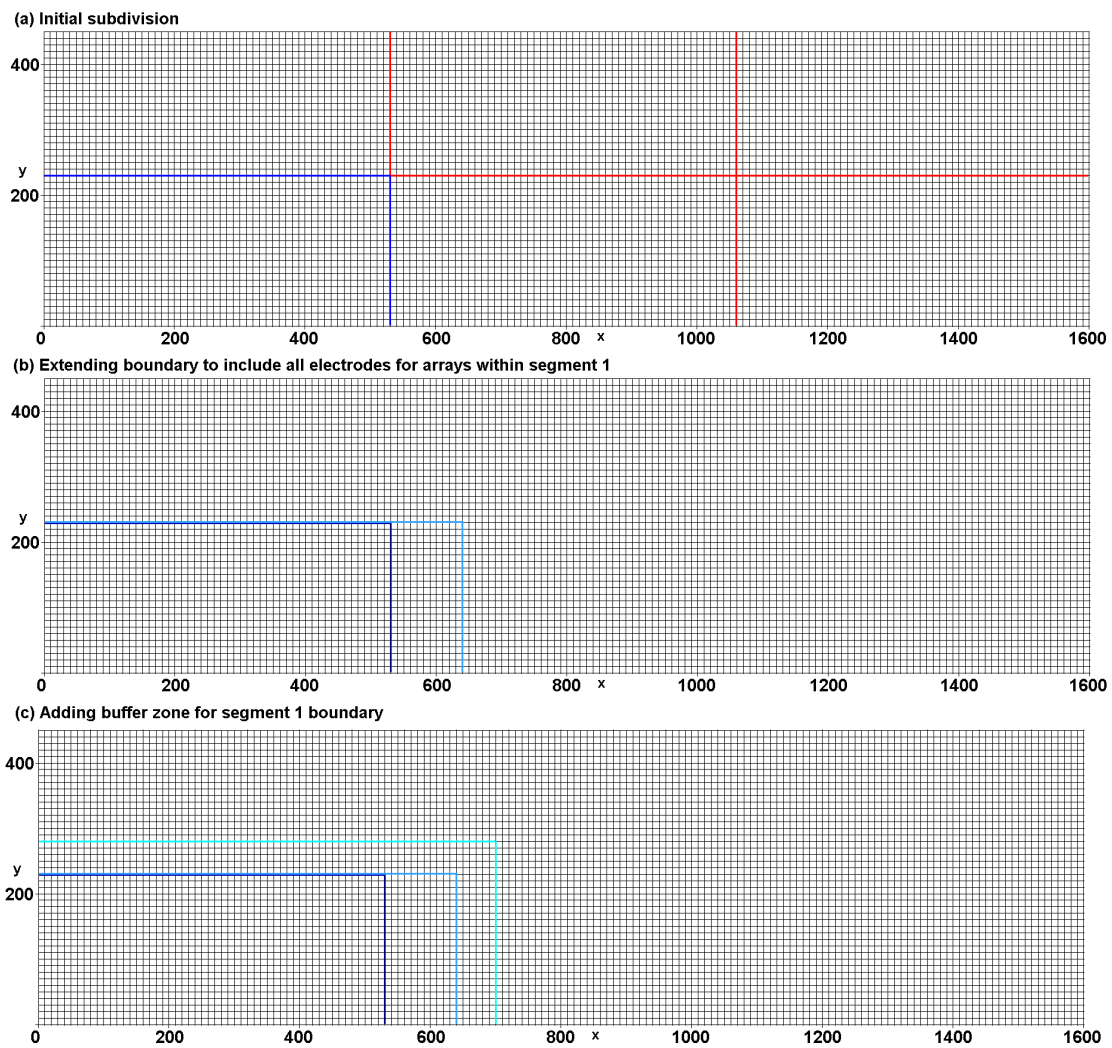


Figure 2. Method used to subdivide a model with 160 by 45 cells (of 10 m width in the x and y directions) in each layer subdivided into 6 segments. (a) Initial subdivision into 6 segments of approximately equal size. The dark blue line marks the region covered by segment 1. (b) Extending the boundary (medium blue line) of segment 1 so that it includes all the electrodes for data points in this segment. (c) Adding a buffer zone around the segment to minimise edge effects. The final region covered by segment 1 is shown by the light blue line.

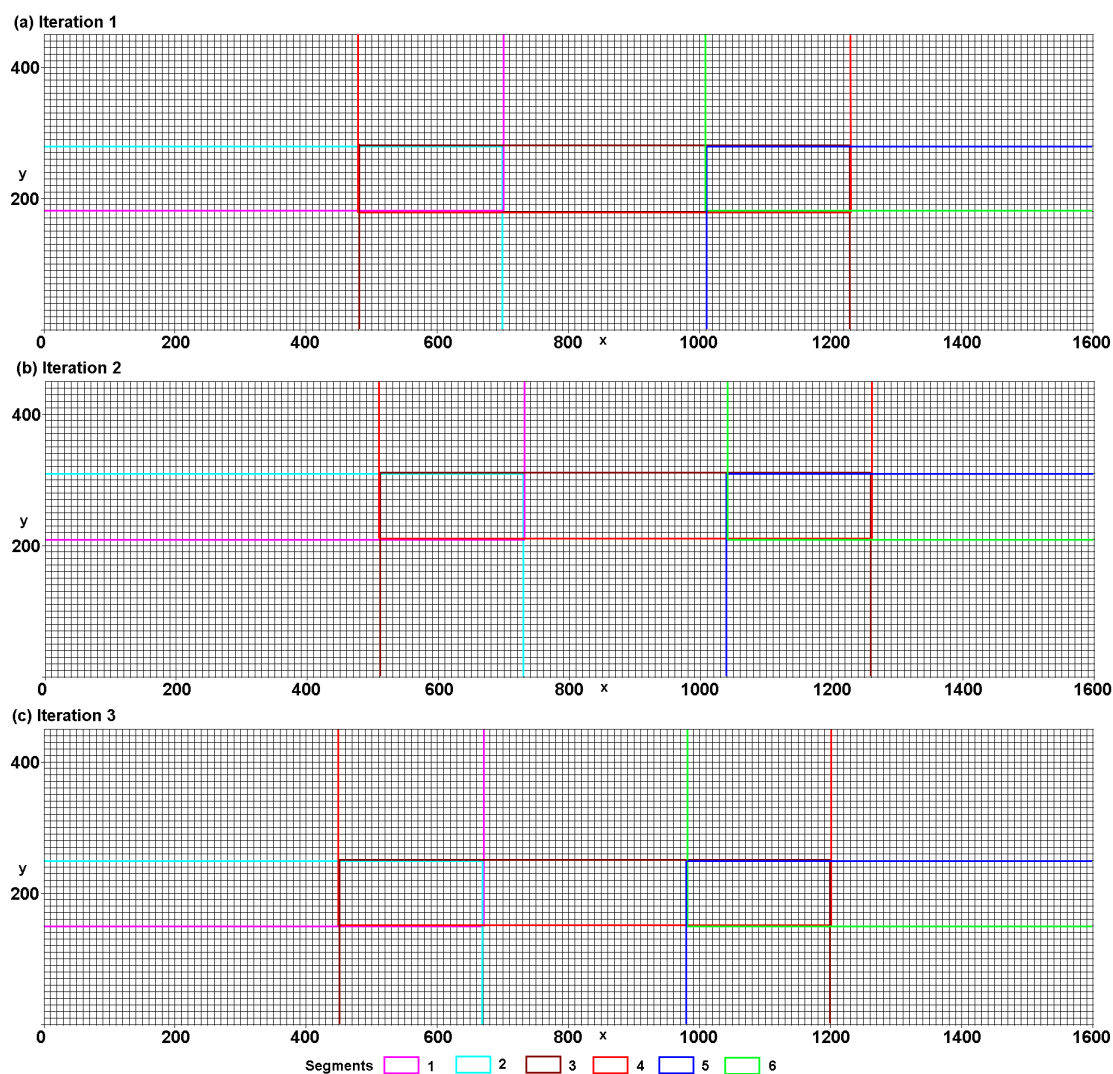


Figure 3. (a) The initial regions of the model grid covered by the 6 segments used in iteration 1 of the least-squares optimisation algorithm. Note the overlaps between neighbouring segments. (b) Shifting of the boundaries of the segments forwards by 3 model grid lines (compared to those used in iteration 1) in iteration 2. (c) Shifting of the boundaries of the segments backwards by 3 model grid lines (compared to those used in iteration 1) in iteration 3.

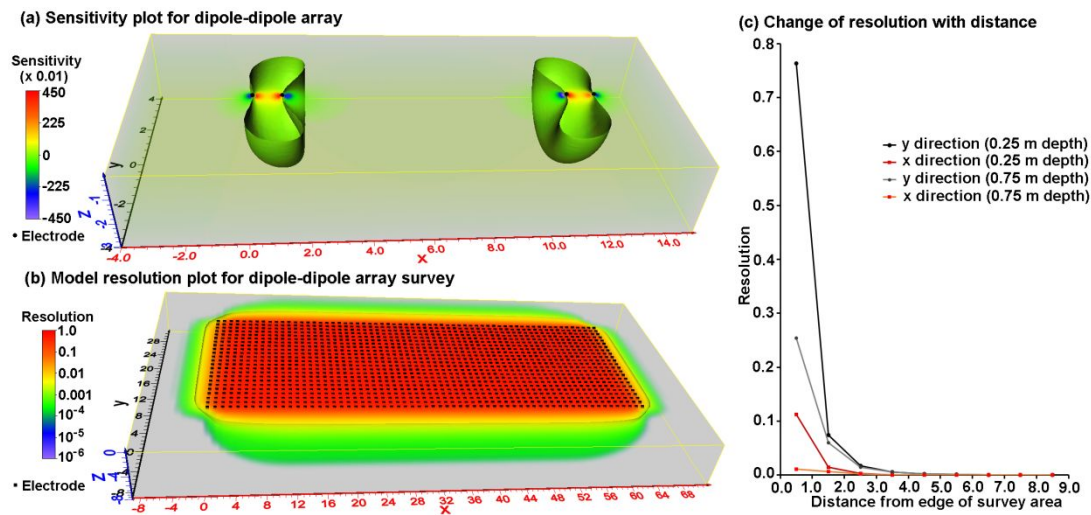


Figure 4. (a) 3-D plot of sensitivity values for the dipole-dipole array with $a=1$ m and $n=10$. The electrodes are located at x positions of 0, 1, 11 and 12 along the $y=0$ axis. The isosurface for sensitivity value of 0.01 is shown. (b) Plot of resolution values for a dipole-dipole array survey with $a=1$ m and $n=1$ to 10 with electrodes in a 64 by 23 grid. The 0.005 isosurface is shown. The electrodes are marked by black dots on the surface. (c) Change of resolution with distance from edge of survey grid at the x and y boundaries. The resolution values of cells at the mid-point of the x and y boundaries (which have the highest values) are shown.

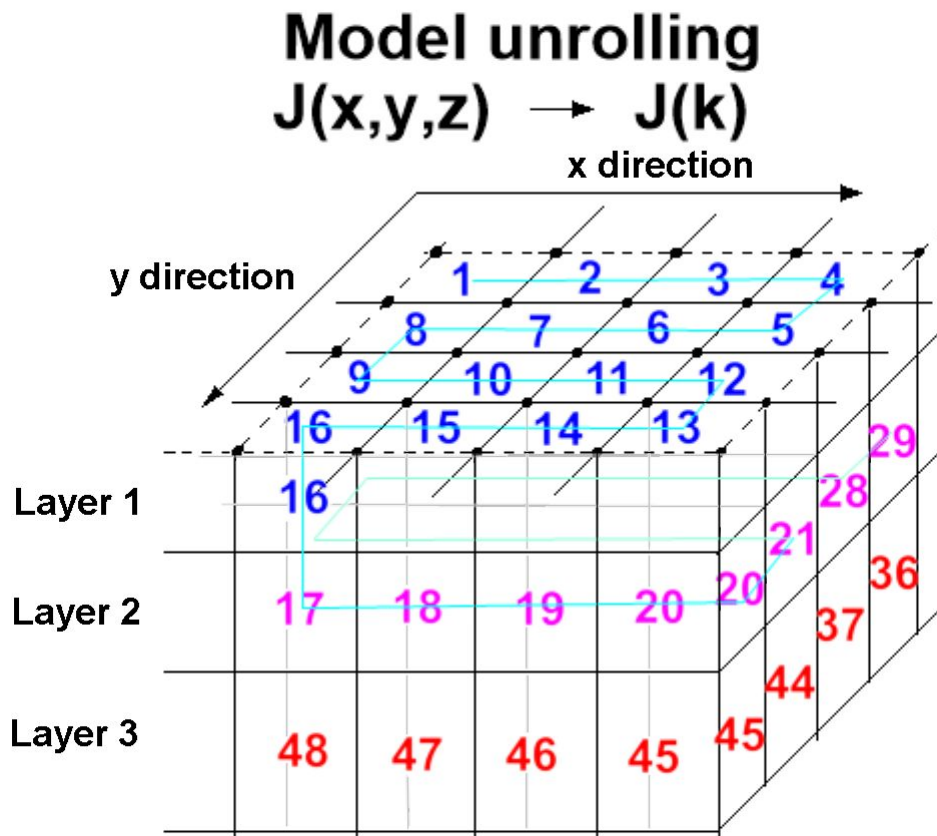


Figure 6. Numbering of model cells arranged in a 3-D rectangular grid so that the Jacobian matrix which is a 3-D function of (x,y,z) is converted to a continuous 1-D function of the model cell index k .

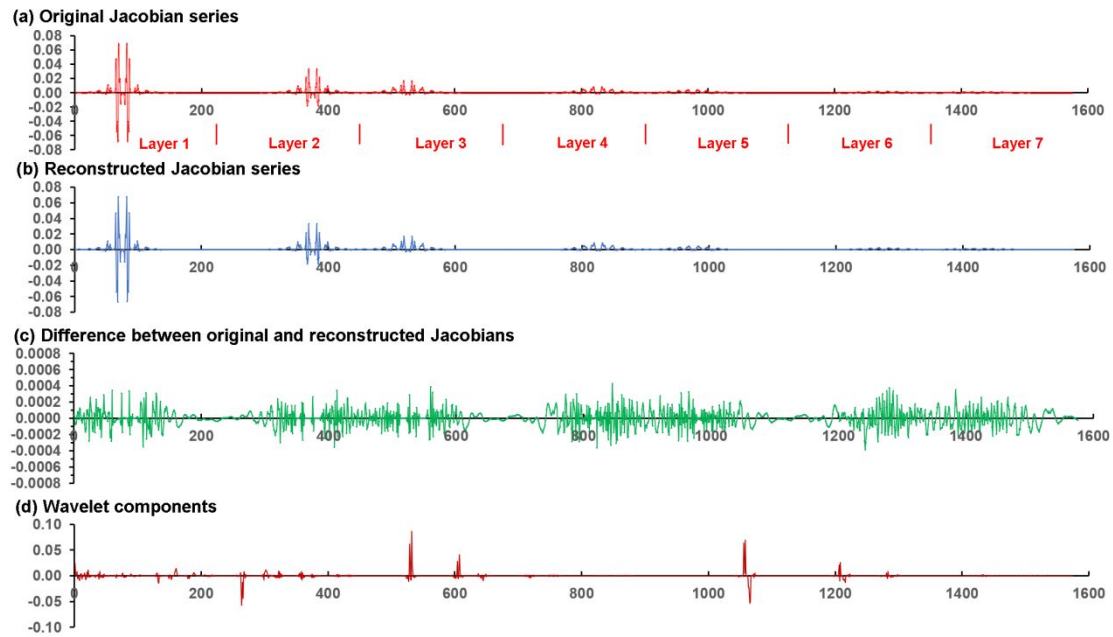


Figure 7. (a) Plot of the Jacobian values for a single pole-dipole array ($a=2$, $n=1$) for a model with $15 \times 15 \times 7$ model cells (each layer has 225 cells). (b) The reconstructed Jacobian values after wavelet components with amplitudes of less than 0.5% of the maximum value were removed. (c) Plot of the difference between the original and reconstructed Jacobian values. Note the vertical scale is 100 times smaller than (a) and (b). (d) Plot of the wavelet components. Values in vertical axis in the plots are dimensionless while the horizontal axis is the model cell index number in (a), (b) and (c), and the wavelet wave number in (d).

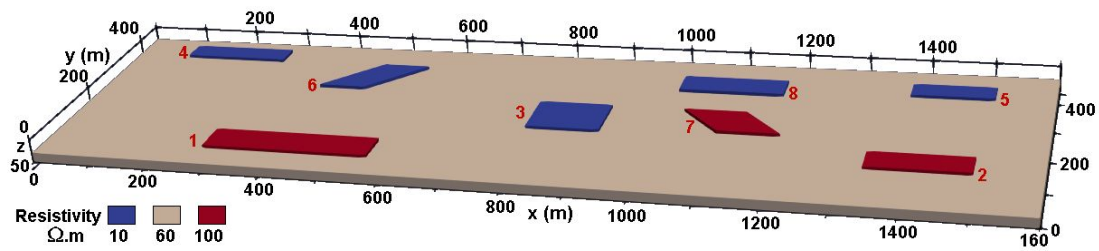


Figure 8. Synthetic model with 8 blocks in the upper layer of a two-layer medium.

The top layer (transparent in the plot) has a resistivity of $30 \Omega.m$ and a thickness of $23.2 m$. Blocks 1 to 5 extend from the surface ($0.0 m$) to a depth of $5.0 m$. The top of blocks 6 to 8 is at $5.0 m$ while the bottom is at $10.5 m$ depth.

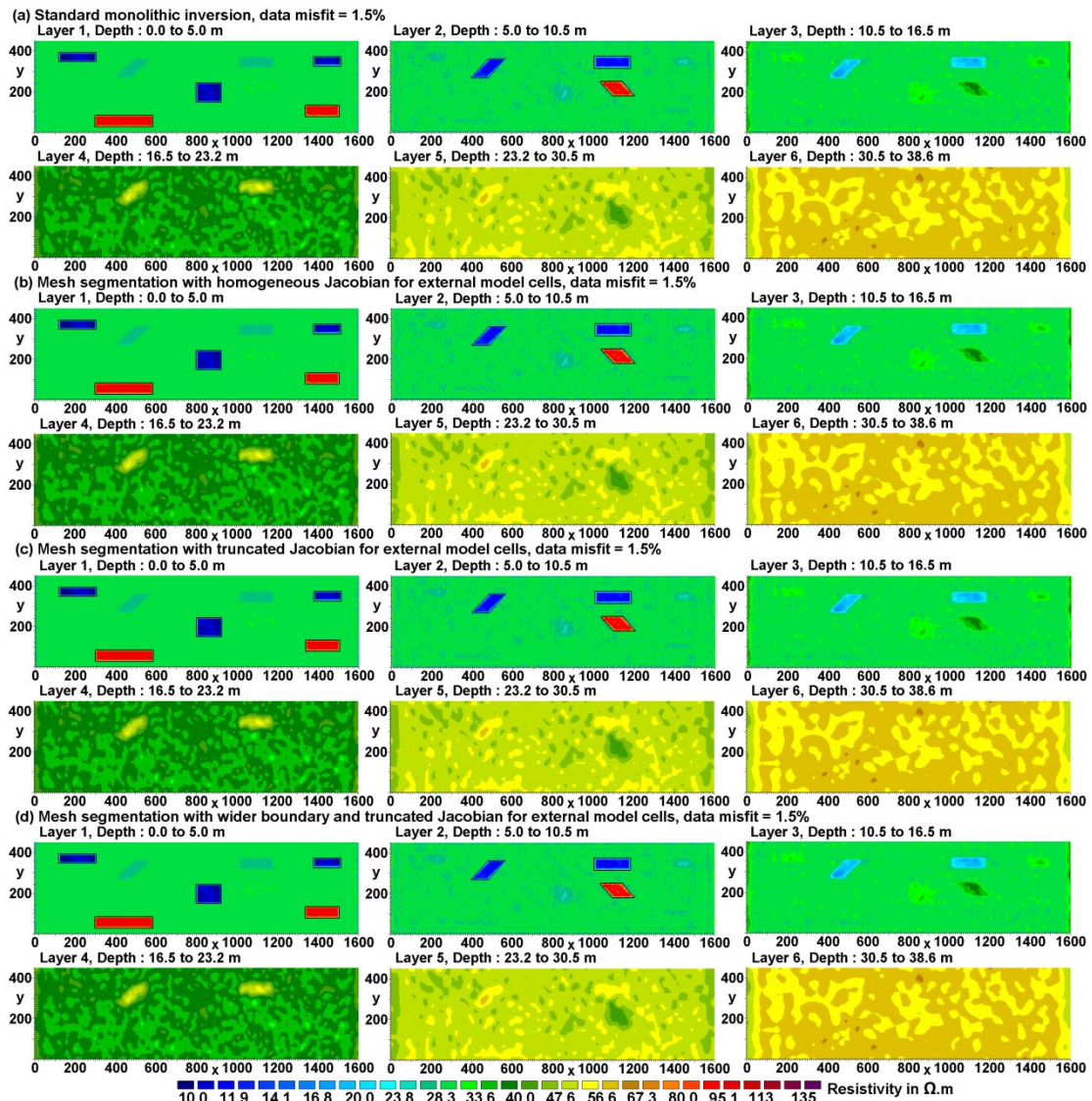


Figure 9. Inverse models of synthetic data set with (a) standard monolithic inversion, (b) using 6 segments with buffer zone of 5 model cells and homogeneous Jacobian approximation for external cells, (c) using segments with buffer zone of 5 model cells and truncated Jacobian for external cells and (d) using segments with buffer zone of 8 model cells and truncated Jacobian for external cells. The blocks in the synthetic model are shown by black outlines in the first 2 layers.

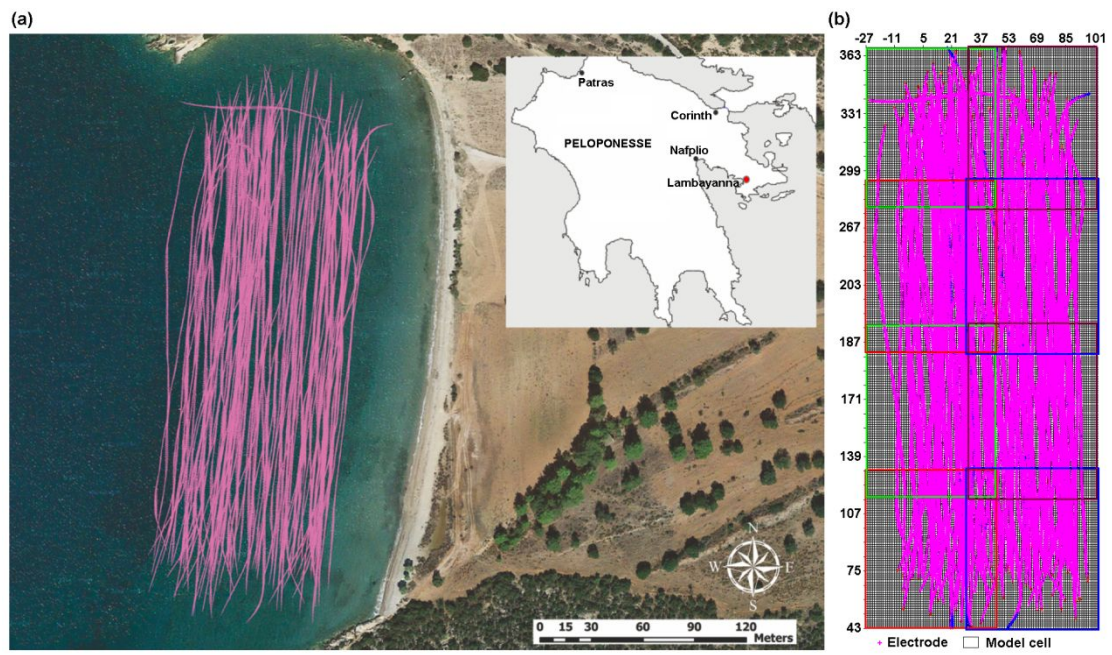


Figure 10. Lambayanna survey (a) map (survey location marked by red circle) and (b) inverse model grid (segments shown by coloured grid lines).

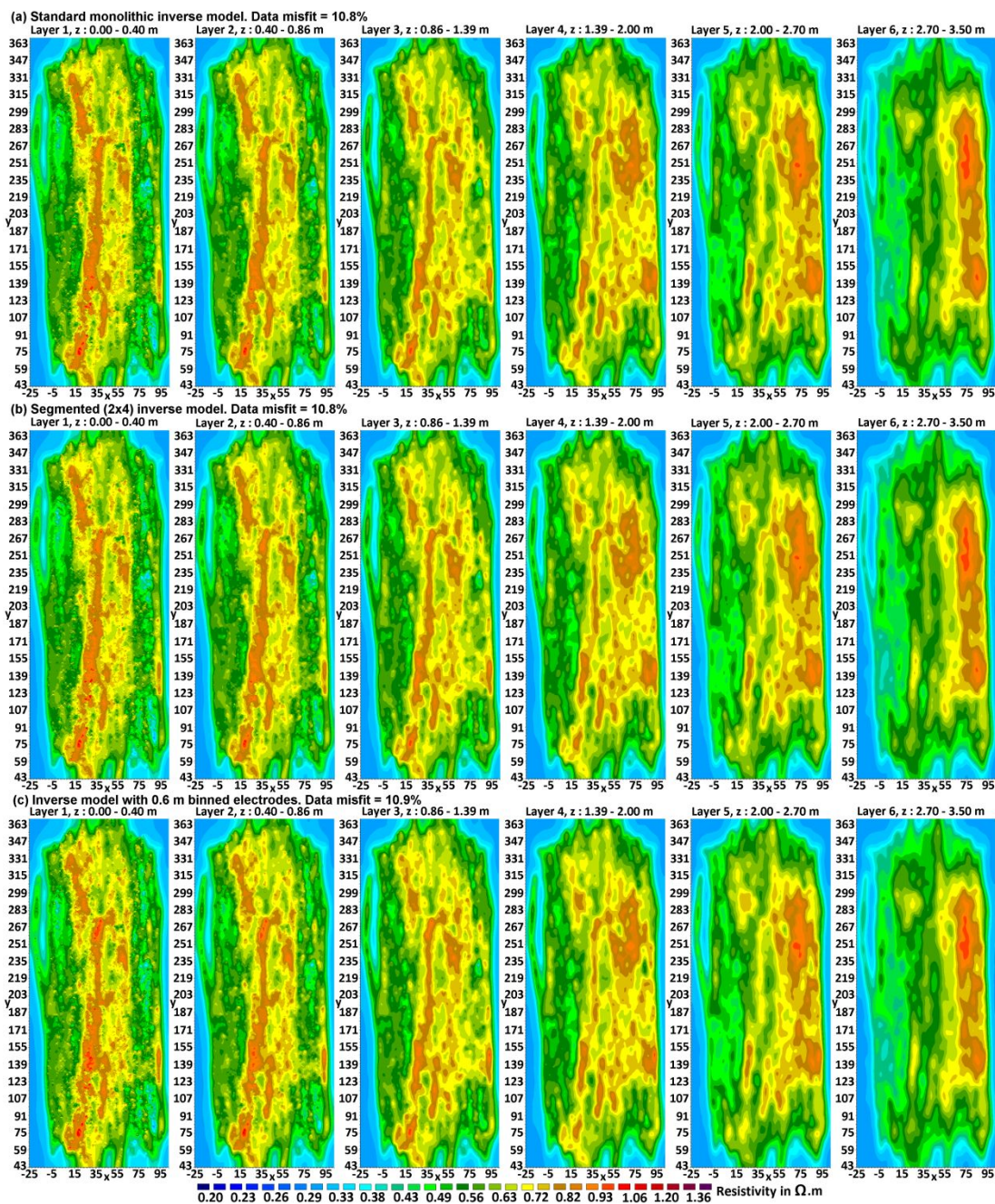


Figure 11. Lambayanna survey inverse models using (a) standard monolithic inversion with a single mesh, (b) 2 by 4 segmented mesh and (c) electrodes binned to every 0.5 m.

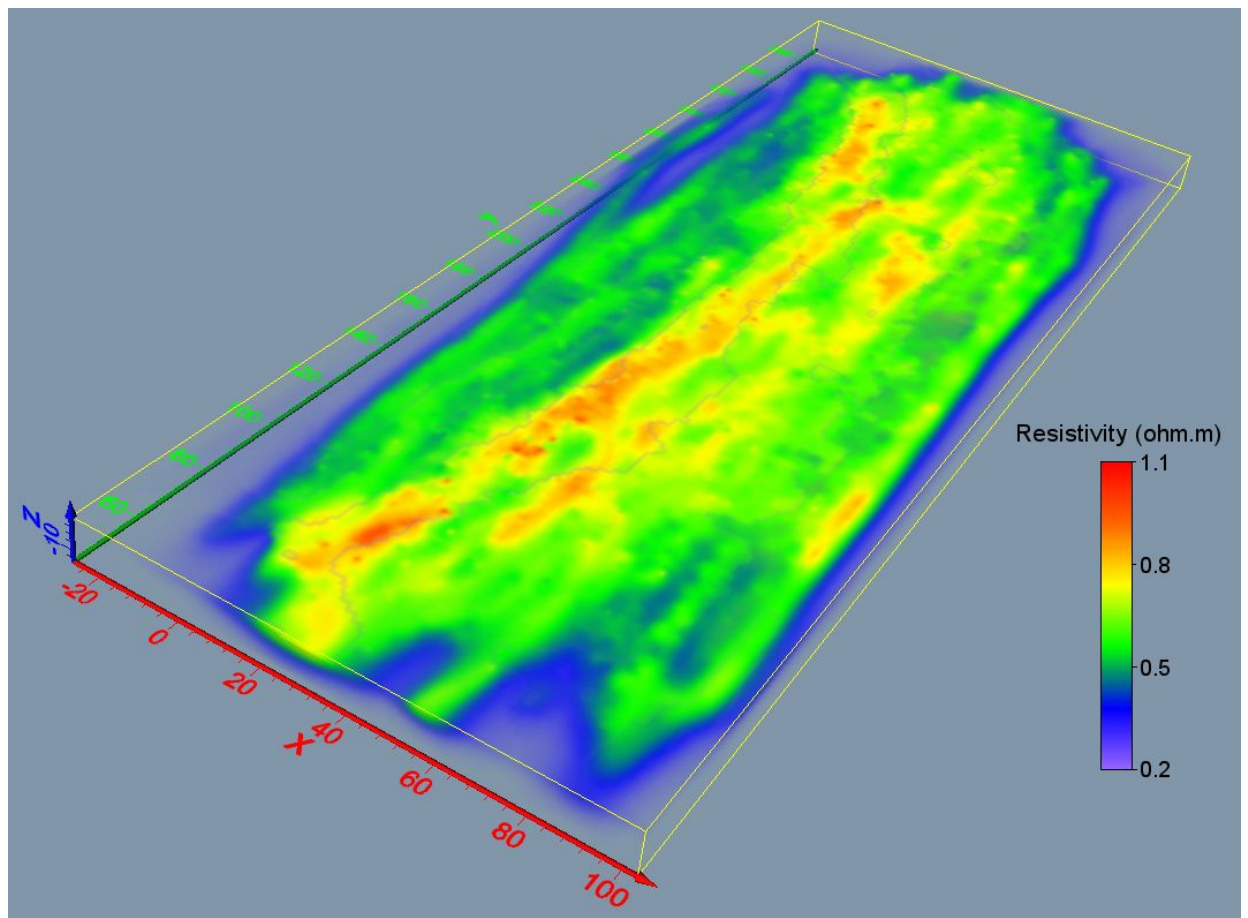


Figure 12. 3-D plot of Lambayanna survey inverse model below the water layer.

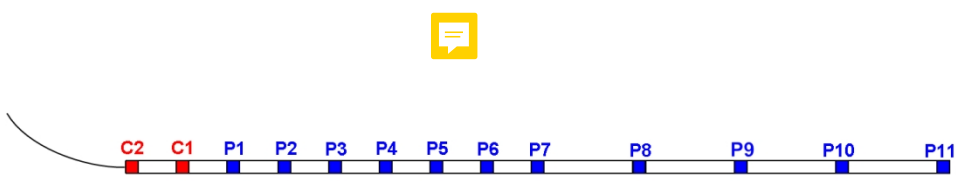


Figure 1. Schematic diagram of a mobile streamer. C1 and C2 are the current electrodes while P1 to P11 are the potential electrodes.

1
2
3
4
5
6
7
8
9
10
11
12
13
14
15
16
17
18
19
20
21
22
23
24
25
26
27
28
29
30
31
32
33
34
35
36
37
38
39
40
41
42
43
44
45
46
47
48
49
50
51
52
53
54
55
56
57
58
59
60

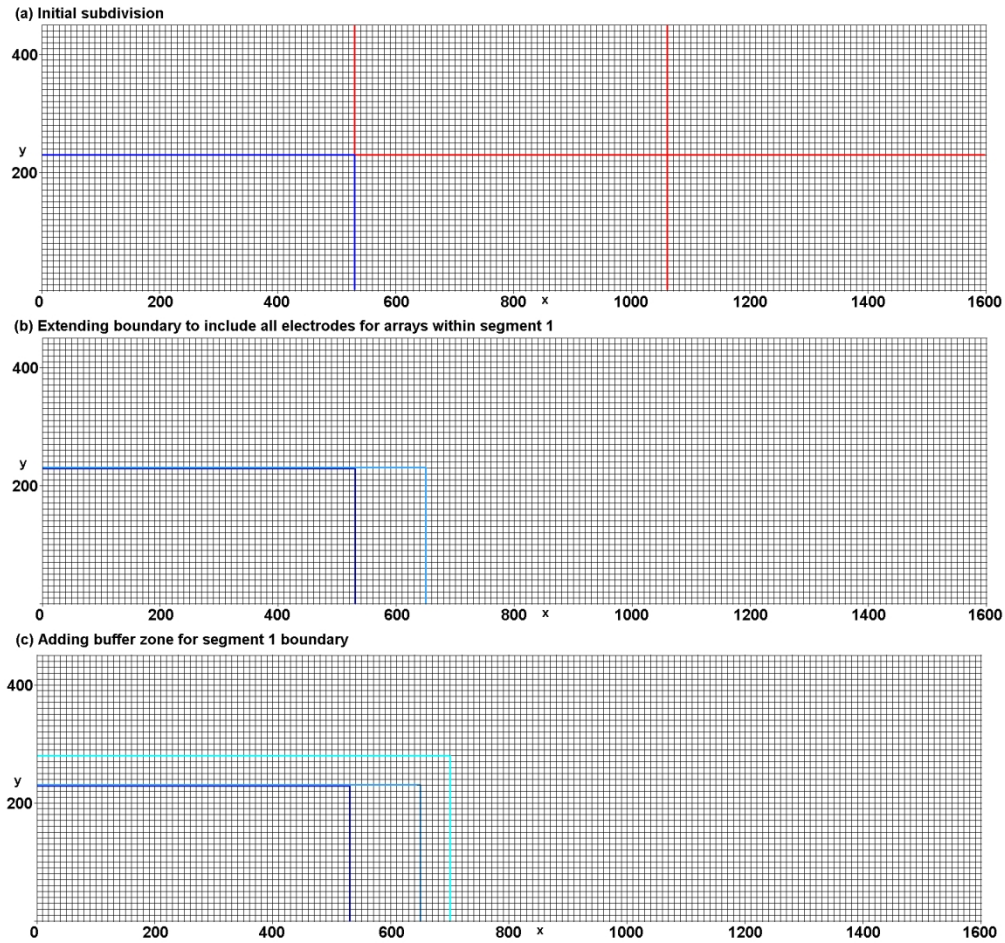


Figure 2. Method used to subdivide a model with 160 by 45 cells (of 10 m width in the x and y directions) in each layer subdivided into 6 segments. (a) Initial subdivision into 6 segments of approximately equal size. The dark blue line marks the region covered by segment 1. (b) Extending the boundary (medium blue line) of segment 1 so that it includes all the electrodes for data points in this segment. (c) Adding a buffer zone around the segment to minimise edge effects. The final region covered by segment 1 is shown by the light blue line.

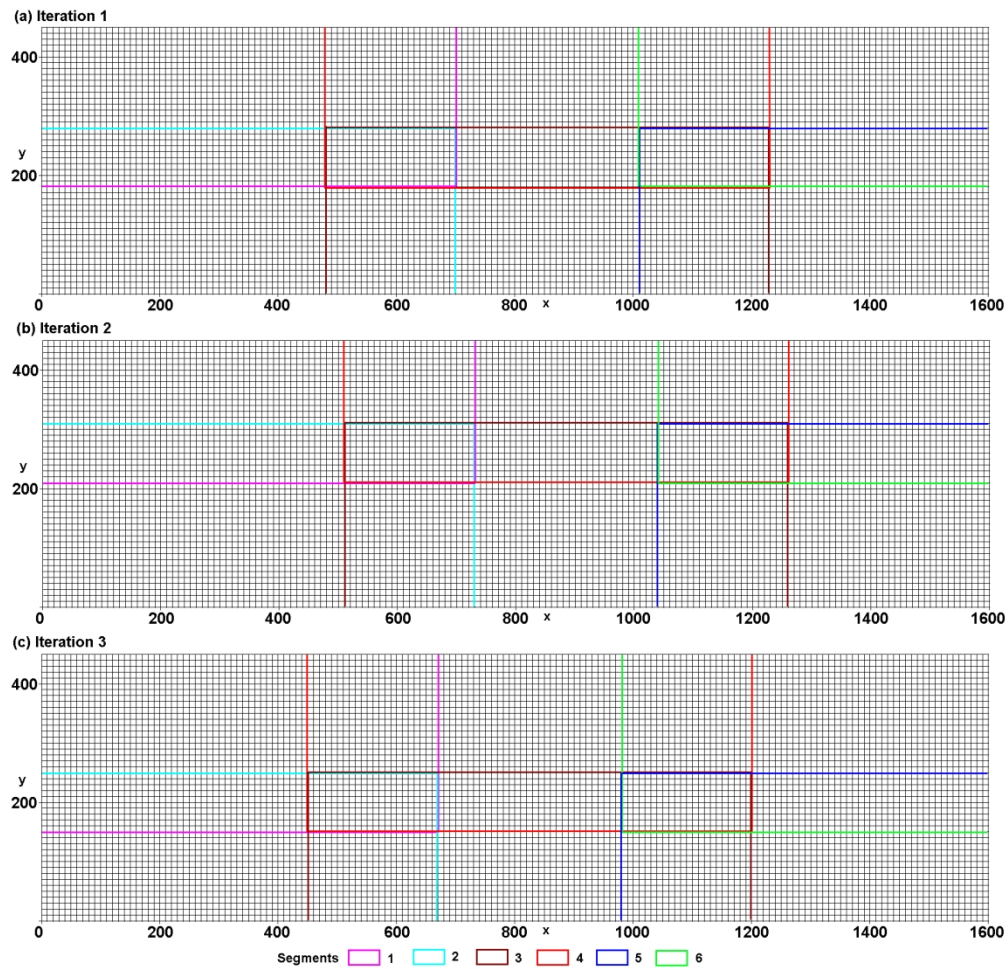


Figure 3. (a) The initial regions of the model grid covered by the 6 segments used in iteration 1 of the least-squares optimisation algorithm. Note the overlaps between neighbouring segments. (b) Shifting of the boundaries of the segments forwards by 3 model grid lines (compared to those used in iteration 1) in iteration 2. (c) Shifting of the boundaries of the segments backwards by 3 model grid lines (compared to those used in iteration 1) in iteration 3.

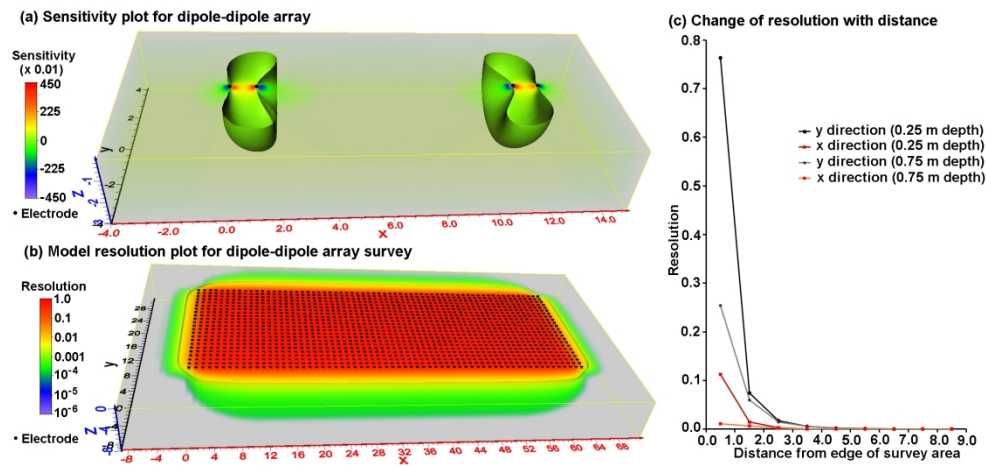


Figure 4. (a) 3-D plot of sensitivity values for the dipole-dipole array with $a=1$ m and $n=10$. The electrodes are located at x positions of 0, 1, 11 and 12 along the $y=0$ axis. The isosurface for sensitivity value of 0.01 is shown. (b) Plot of resolution values for a dipole-dipole array survey with $a=1$ m and $n=1$ to 10 with electrodes in a 64 by 23 grid. The 0.005 isosurface is shown. The electrodes are marked by black dots on the surface. (c) Change of resolution with distance from edge of survey grid at the x and y boundaries. The resolution values of cells at the mid-point of the x and y boundaries (which have the highest values) are shown.

1
2
3
4
5
6
7
8
9
10
11
12
13
14
15
16
17
18
19
20
21
22
23
24
25
26
27
28
29
30
31
32
33
34
35
36
37
38
39
40
41
42
43
44
45
46
47
48
49
50
51
52
53
54
55
56
57
58
59
60

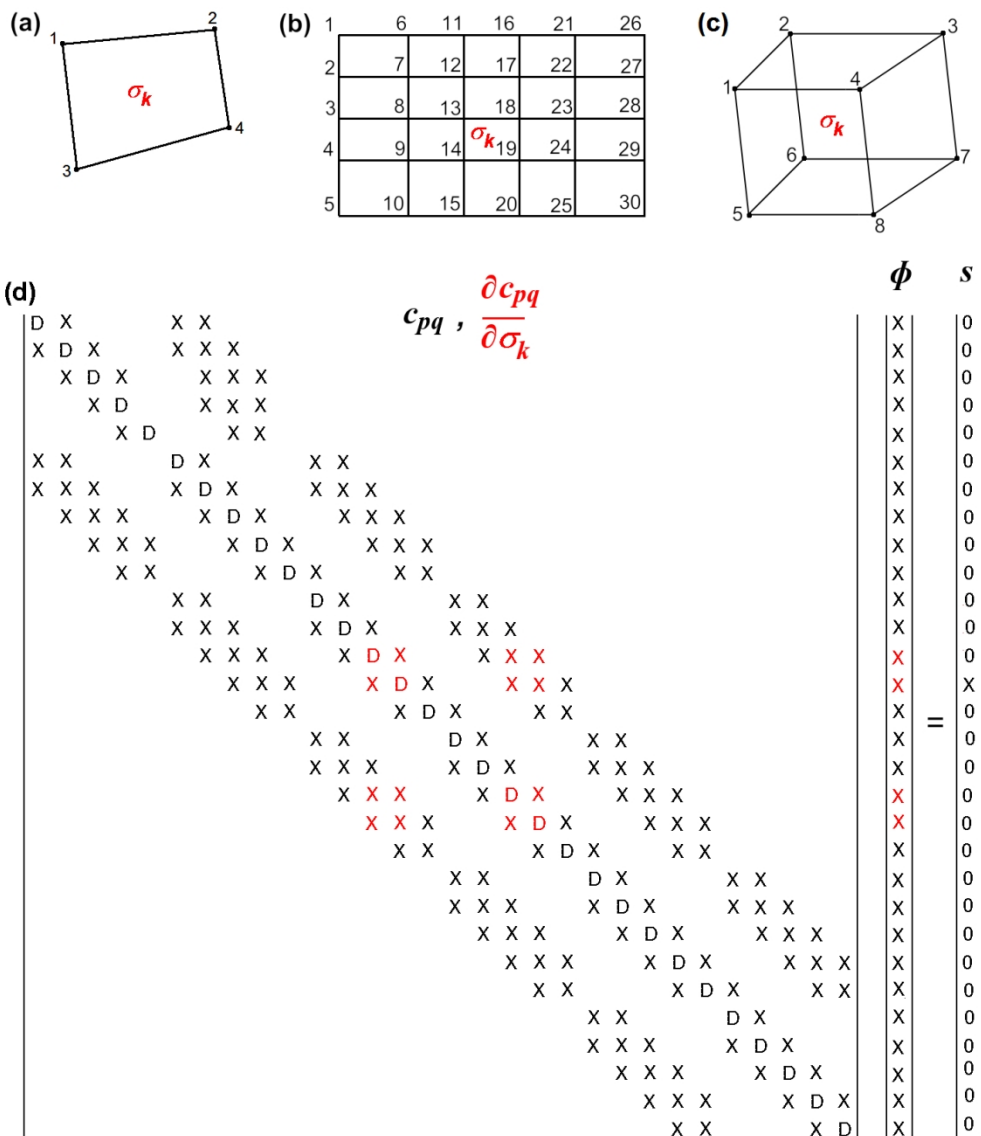


Figure 5. (a) 2-D quadrilateral element with 4 nodes. (b) Example 2-D finite-element mesh with node numbers. (c) 3-D hexahedral element with 8 nodes. (d) Schematic diagram of the structure of the capacitance matrix equation for the 2-D mesh with the non-zero elements. D represents a diagonal element while X represents a non-zero off-diagonal element. The members of the matrix (due to a change in the conductivity of the k mesh cell) that have non-zero values are marked in red.

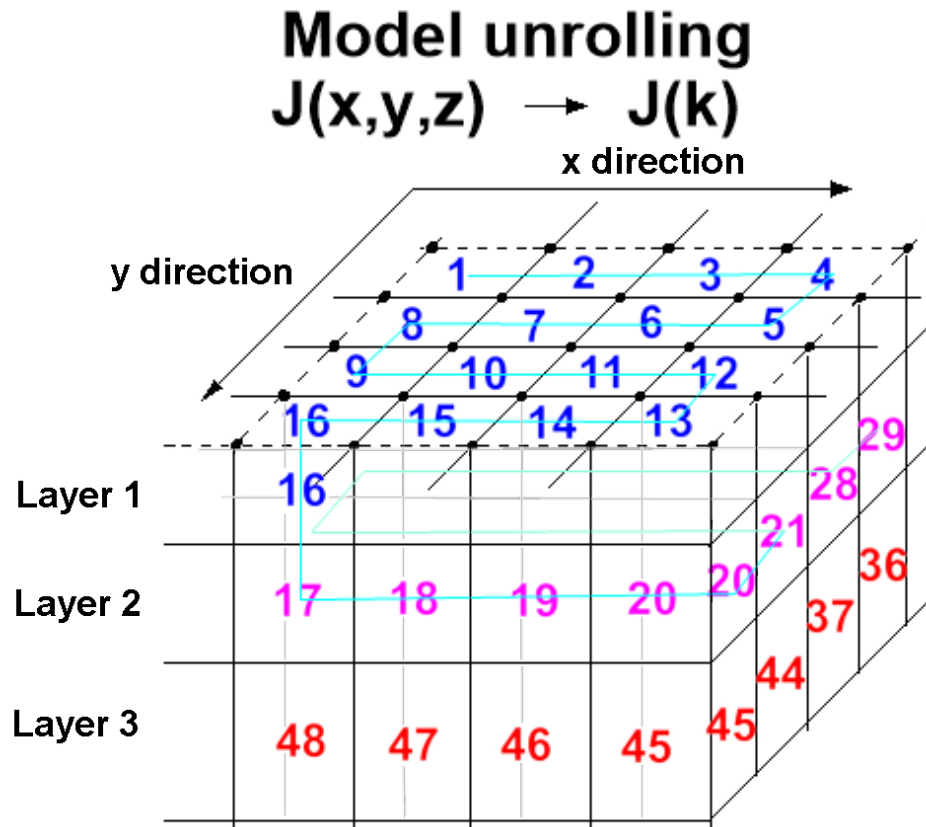


Figure 6. Numbering of model cells arranged in a 3-D rectangular grid so that the Jacobian matrix which is a 3-D function of (x,y,z) is converted to a continuous 1-D function of the model cell index k .

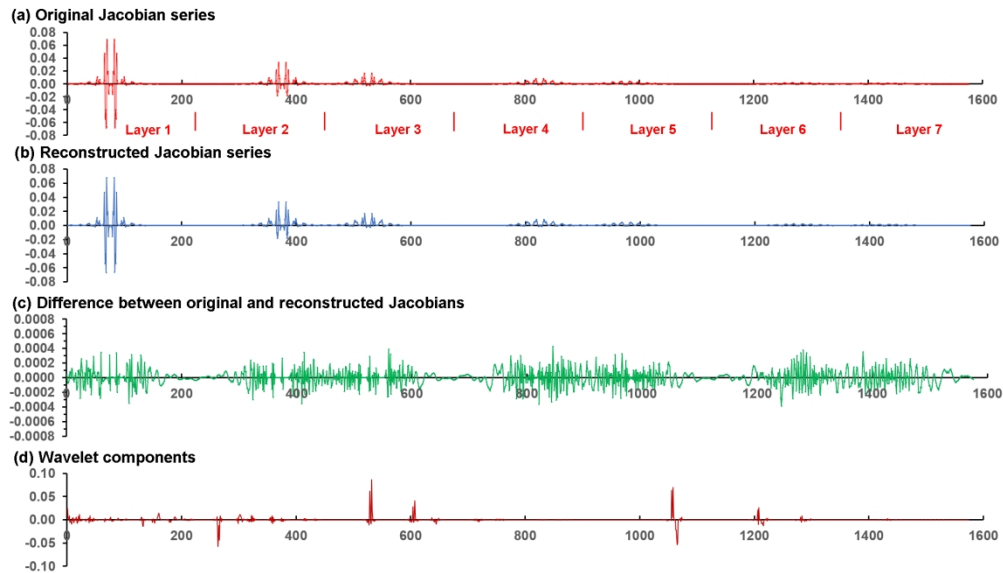


Figure 7. (a) Plot of the Jacobian values for a single pole-dipole array ($a = 2$, $n = 1$) for a model with $15 \times 15 \times 7$ model cells (each layer has 225 cells). (b) The reconstructed Jacobian values after wavelet components with amplitudes of less than 0.5% of the maximum value were removed. (c) Plot of the difference between the original and reconstructed Jacobian values. Note the vertical scale is 100 times smaller than (a) and (b). (d) Plot of the wavelet components. Values in vertical axis in the plots is are dimensionless. The horizontal axis is the model cell index number in (a), (b) and (c), and the wavelet wave number in (d).

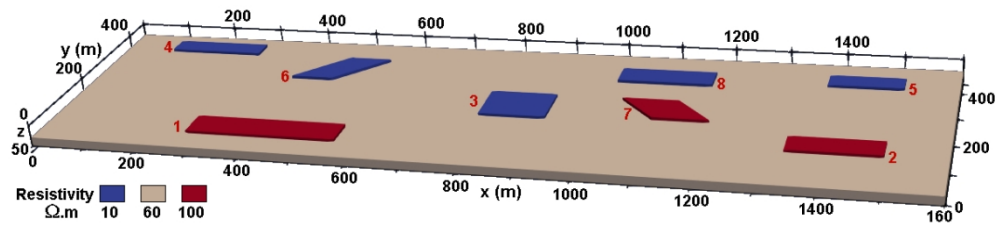


Figure 8. Synthetic model with 8 blocks in the upper layer of a two-layer medium. The top layer (transparent in the plot) has a resistivity of 30 Ω .m and a thickness of 23.2 m. Blocks 1 to 5 extend from the surface (0.0 m) to a depth of 5.0 m. The top of blocks 6 to 8 is at 5.0 m while the bottom is at 10.5 m depth.

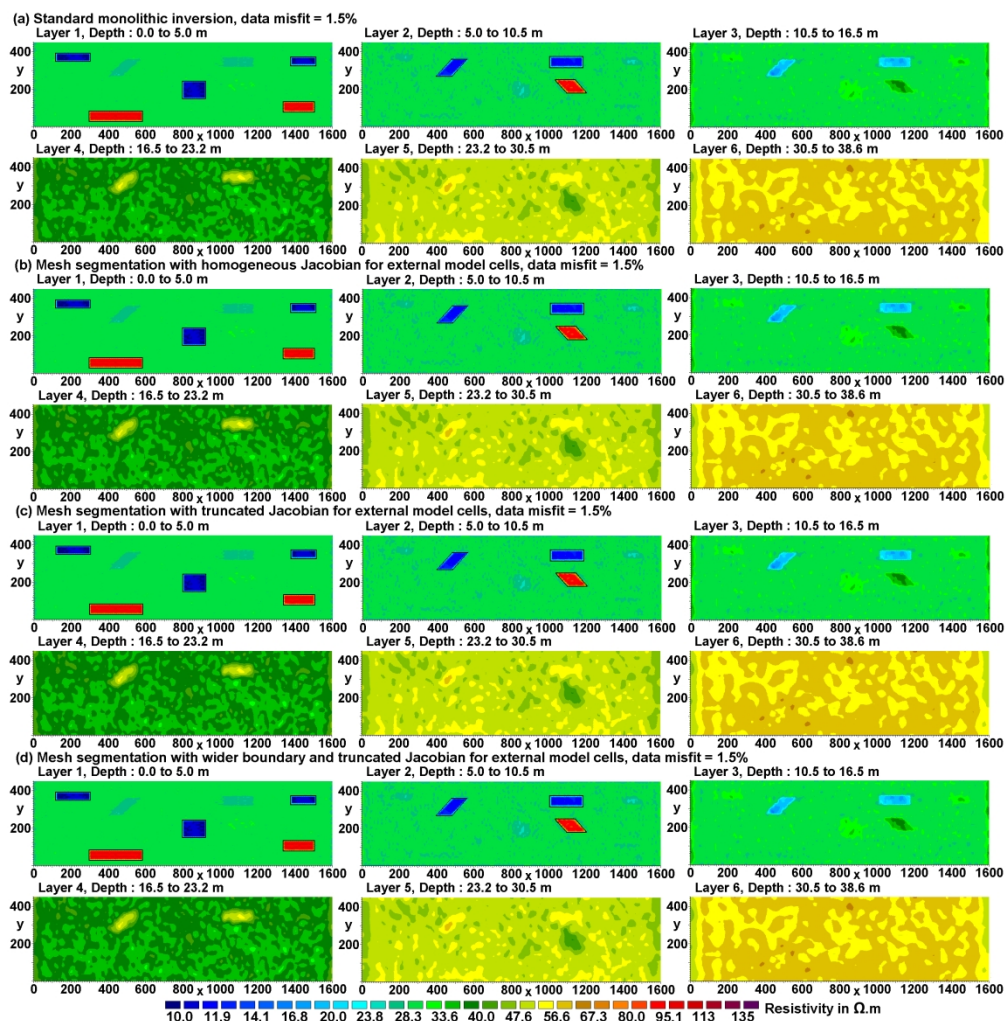


Figure 9. Inverse models of synthetic data set with (a) standard monolithic inversion, (b) using 6 segments with buffer zone of 5 model cells and homogeneous Jacobian approximation for external cells, (c) using segments with buffer zone of 5 model cells and truncated Jacobian for external cells and (d) using segments with buffer zone of 8 model cells and truncated Jacobian for external cells. The blocks in the synthetic model are shown by black outlines in the first 2 layers.

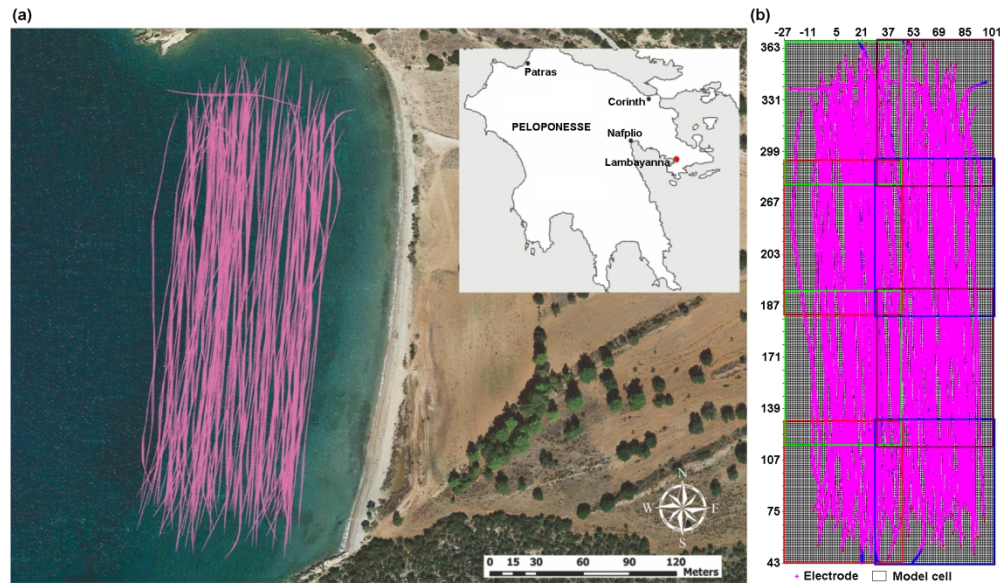


Figure 10. Lambayanna survey (a) map and (b) inverse model grid (segments shown by coloured grid lines).

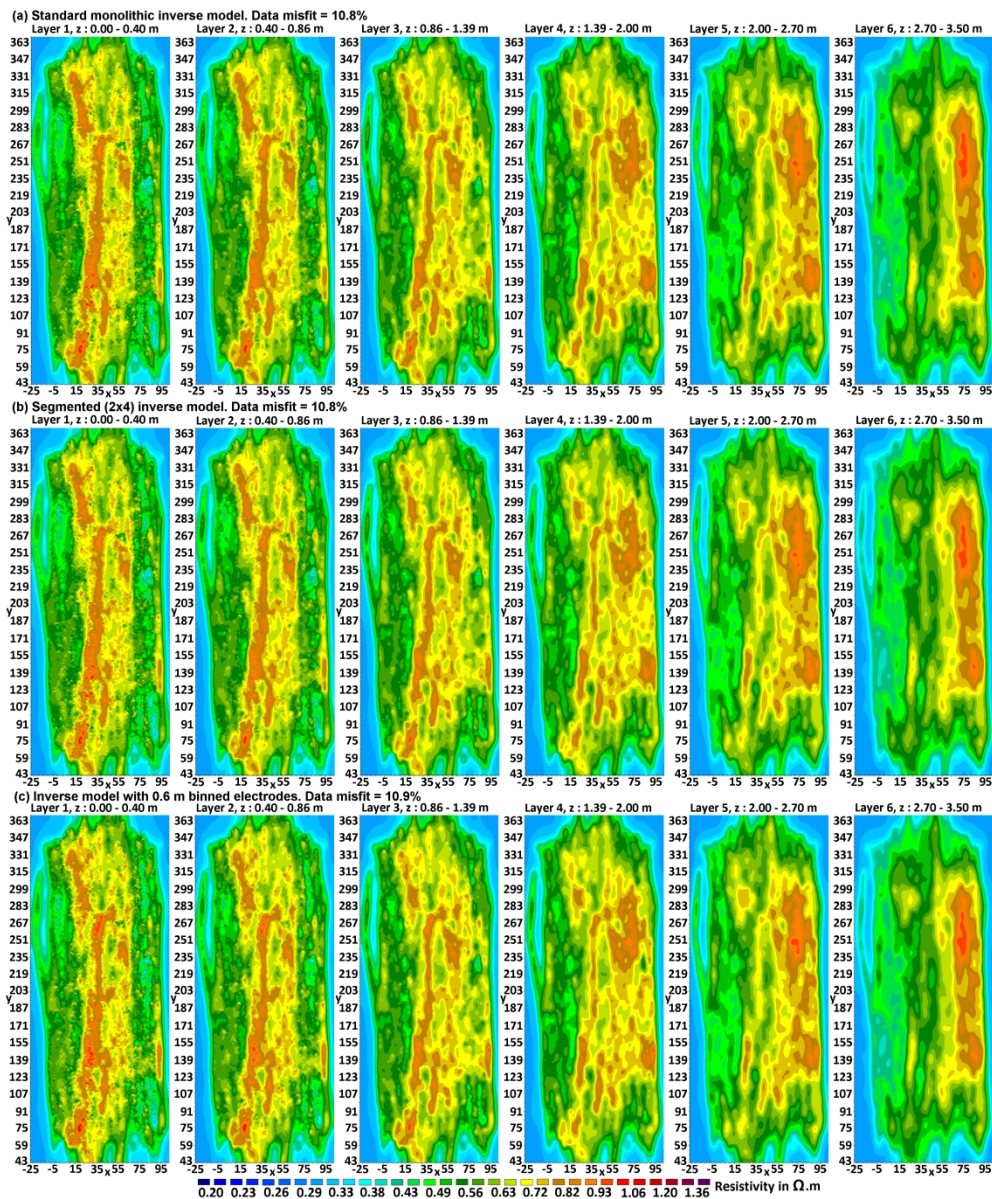


Figure 11. Lambayanna survey inverse models using (a) standard monolithic inversion with a single mesh, (b) 2 by 4 segmented mesh and (c) electrodes binned to every 0.5 m.

1
2
3
4
5
6
7
8
9
10
11
12
13
14
15
16
17
18
19
20
21
22
23
24
25
26
27
28
29
30
31
32
33
34
35
36
37
38
39
40
41
42
43
44
45
46
47
48
49
50
51
52
53
54
55
56
57
58
59
60

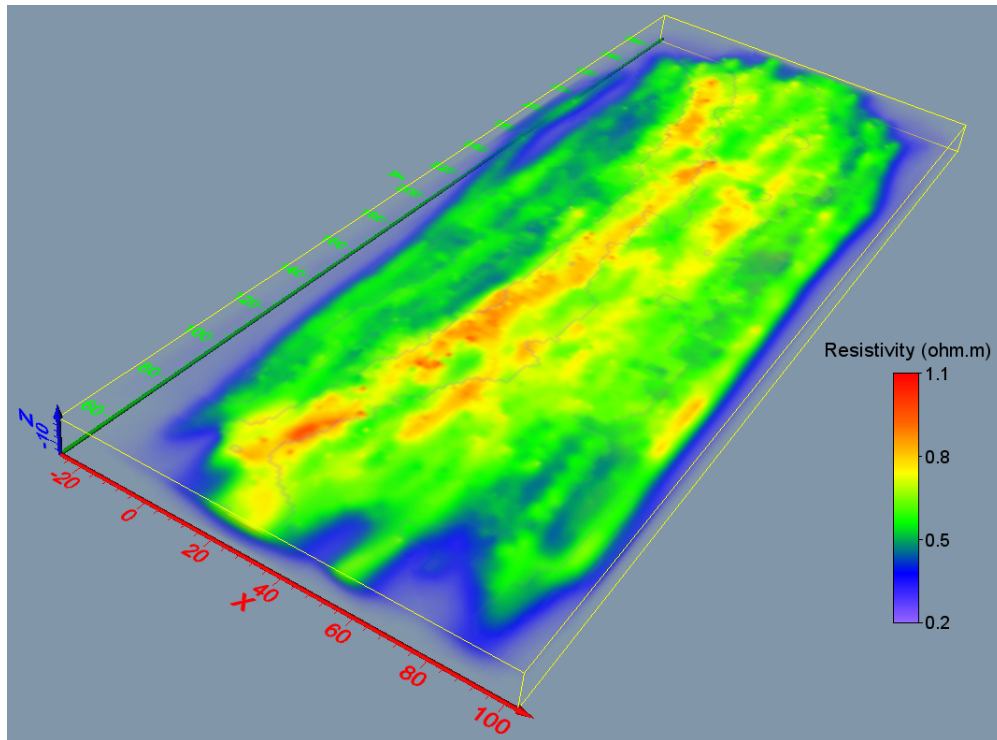


Figure 12. 3-D plot of Lambayanna survey inverse model below the water layer.

The inversion of data from very large 3-D ERT mobile surveys.

M.H. Loke^{1*}, N. Papadopoulos², P.B. Wilkinson³, D. Oikonomou^{2,4}, K. Simyrdanis²
and D. Rucker⁵

¹ Geotomo Software Sdn Bhd, 115 Cangkat Minden Jalan 6, 11700 Gelugor, Penang, Malaysia.

email : drmhloke@yahoo.com

² Laboratory of Geophysical-Remote Sensing & Archaeoenvironment (GeoSat ReSeArch), Institute for Mediterranean Studies, Foundation for Research and Technology Hellas, Nikiforou Foka 130, 74 100 Rethymno, Crete, Greece.

emails : nikos@ims.forth.gr, doikonomou@ims.forth.gr, ksimirda@ims.forth.gr

³ British Geological Survey, Keyworth, Nottingham, NG12 5GG, U.K.

email : pbw@bgs.ac.uk

⁴ Aristotle University of Thessaloniki, Thessaloniki, Greece.

⁵ hydroGEOPHYSICS Inc., 2302 North Forbes Boulevard, Tucson, AZ 85745, U.S.A.

email : druck8240@gmail.com

* Corresponding author

Keywords : Resistivity inversion, 3-D, segmentation

Abstract

New developments in mobile resistivity meter instrumentation have made it possible to survey large areas with dense data coverage. The mobile system usually has a limited number of electrodes attached to a cable that is pulled along behind an operator so that a large area can be covered within a short time. Such surveys can produce 3-D data sets with hundreds of thousands of electrodes positions and data points. Similarly, the inverse model used to interpret the data can have several hundred thousand cells. It is impractical to model such large data sets within a reasonable time on microcomputers used by many small companies employing standard inversion techniques. We describe a model segmentation technique that subdivides the finite-element mesh used to calculate the apparent resistivity and Jacobian matrix values into a number of smaller meshes. A fast technique that optimises the calculation of the Jacobian matrix values for multi-channel systems was also developed. A 1-D wavelet transform method was then used to compress the storage of the Jacobian matrix, in turn reducing the computer time and memory required to solve the least-squares optimisation equation to determine the inverse model resistivity values. The new techniques reduce the calculation time and memory required by more than 80% while producing models that differ by less than 1% from that obtained using the standard inversion technique with a single mesh. We present results using a synthetic model and a field data set that illustrates the effectiveness of the proposed techniques.

Data Availability Statement

The data that support the findings of this study are available from the corresponding author upon reasonable request.

INTRODUCTION

3-D ERT (Electrical Resistivity Tomography) surveys are now widely used to map areas with complex geology (Loke *et al.* 2013a). Most surveys use multi-channel resistivity meter systems with the electrodes planted in the ground. A system with 32 to 128 electrodes linked by multi-core cables to the resistivity meter is frequently used. The number of unique electrode positions used in the survey usually does not exceed a few thousand. Compared to normal 'static' resistivity meter systems, 'mobile' systems use a cable with a more limited number of electrodes (4 to 12) that is pulled along the surface. Some surveys use a normal galvanic resistivity-meter system with a streamer pulled behind a boat in a water-covered area (Rucker and Noonan 2013; Simyrdanis *et al.* 2015). In land surveys capacitively coupled systems (Hildes *et al.* 2005; Kuras *et al.* 2006; Unrau 2019) can be used that avoid direct galvanic contact with the ground where a limited number of measurements are simultaneously made at approximately regular intervals. Both types use a GPS receiver attached to a computerised central system to trace the position of the line and subsequently estimate the actual position of the electrodes with a certain accuracy based on specific assumptions (Oikonomou *et al.* 2019). The streamer is pulled to and fro [crisscrossing](#) the survey area to get dense data coverage. In some surveys, the number of unique electrode positions can exceed a hundred thousand. A 3-D finite-element mesh is used to model the resistivity data so that topography can be directly incorporated into the inverse model (Loke 2000). To accurately model the data from such large surveys, a dense mesh with more than one million nodes is sometimes used. The combination of a large number of electrode positions together with a large mesh presents computational problems in terms of computer execution time and high memory demands.

1
2
3 To reduce these computational issues, some researchers in the past have
4 resorted to shortcuts, such as binning electrode positions, nudging electrode positions
5 and subdomains. Xu and Dunbar (2015) took methods from marine-based streaming
6 seismic acquisition through data binning. The technique of binning converts a series
7 of closely spaced 2-D profiles into a quasi-3-D survey through combining scattered
8 data points onto regular grids and then conducting 3-D inversion. The survey is
9 divided into multiple rectangular horizontal zones called bins on the surface and each
10 measurement is assigned to a bin according to the midpoint between the source and
11 the receiver. The apparent resistivity measurements are sorted into bins based on the
12 centre points of each four-electrode configuration and there will typically be multiple
13 measurements placed into a single bin. The bin size is selected based on the data
14 density and the required resolution of the 3-D inversion, balanced with the time
15 required to complete the resulting 3-D inversion. Rucker *et al.* (2009) used a concept
16 called nudging to move the electrode positions for ease of modelling. To decrease the
17 number of unique electrode positions, thereby reducing the number of mesh nodes
18 needed for inversion, they nudged electrodes to the nearest 3 m. The initial survey
19 design was established on a 3 m grid, but a few of the electrode coordinates for non-
20 orthogonal lines had to be repositioned to reduce memory storage. Their justification
21 for nudging was a trade-off between accuracy and expediency, for what was at the
22 time, the largest published 3-D modelling study with over 7,000 electrode positions.
23
24
25
26
27
28
29
30
31
32
33
34
35
36
37
38
39
40
41
42
43
44
45
46
47
48

49 Rucker *et al.* (2009) also experimented with manually dividing the large
50 model domain into individually processed, smaller subdomains in order to reduce the
51 computer memory usage; computer memory was generally quite low at the time of the
52 study relative to today. Experiments with the subdomains included increasing the
53 amount of overlap for adjacent models. Four sets of model overlap were tested
54
55
56
57
58
59
60

1
2
3 including: 15 m (6 total model domains), 50 m (8 total model domains), 100 m (15
4 total model domains), and 150 m (50 total model domains). The results of modelling
5
6 total model domains), and 150 m (50 total model domains). The results of modelling
7
8 with a large number of subdomains were undesirable, showing mismatches in target
9
10 shape and values in the areas of overlap.

11
12 In this paper we describe techniques to reduce the computer time and memory
13
14 needed so that the data inversion to produce a 3-D model can be completed within a
15
16 reasonable time with common personal computers. We use a method similar to
17
18 Rucker *et al.* (2009) in creating subdomains. Here, we refer to it as mesh
19
20 segmentation. The difference in the methodology, however, is that the overlap from
21
22 one domain is accommodated in the other domains to ensure continuity in model
23
24 values. While the potentials and sensitivity values are calculated individually for each
25
26 segment (similar to the subdomain technique), a single unified model inversion step is
27
28 carried out that covers the entire survey area. This greatly reduces mismatches in the
29
30 areas of overlap.
31
32
33
34

35 We test the new mesh segmentation method on synthetic and field data sets
36
37 and demonstrate that the results are nearly identical to modelling all of the data using
38
39 a single mesh. The advantage, however, is the significantly reduced computer time
40
41 and memory.
42
43
44
45
46
47
48

49 **DATA INVERSION METHOD**

50
51 For 3-D ERT data sets, the smoothness-constrained least-squares optimisation
52
53 method is widely used (Li and Oldenburg 2000, Loke *et al.* 2013a). The linearised
54
55 least-squares equation that gives the relationship between the model parameters (\mathbf{r})
56
57 and the data misfit (\mathbf{g}) is given below.
58
59
60

$$\left[\mathbf{J}_i^T \mathbf{R}_d \mathbf{J}_i + \lambda_i \mathbf{W}^T \mathbf{R}_m \mathbf{W} \right] \Delta \mathbf{r}_i = \mathbf{J}_i^T \mathbf{R}_d \mathbf{g}_i - \lambda_i \mathbf{W}^T \mathbf{R}_m \mathbf{W} (\mathbf{r}_{i-1} - \mathbf{r}_m) \quad (1)$$

The Jacobian matrix \mathbf{J} contains the partial derivatives of the measured data (apparent resistivities) with respect to the model resistivity. The inversion procedure is stabilised through the roughness filter \mathbf{W} (deGroot-Hedlin and Constable 1990) with a damping factor λ . $\Delta \mathbf{r}_i$ is the required change in the model parameters (the logarithms of the model resistivity values) to reduce the data misfit \mathbf{g} while \mathbf{r}_{i-1} is the resistivity model from the previous iteration. The vector \mathbf{r}_m is a reference background model. \mathbf{R}_d and \mathbf{R}_m are weighting matrices used by the L1-norm inversion method (Farquharson and Oldenburg 1998) applied to the data misfit and model roughness. The inversion algorithm usually takes 3 to 6 iterations to converge. In the tests with the data sets carried out in this paper, we used the L1-norm for both the data misfit and model roughness. Further details on the practical use of the least-squares iterative method, such as the use of different norms and selection of the damping factor, can be found in the references (Farquharson and Oldenburg 1998; Loke *et al.* 2003; Farquharson and Oldenburg 2004; Loke *et al.* 2014a).

Each iteration requires the calculation of the model response (calculated apparent resistivity values) using the finite-element method and the Jacobian matrix using the adjoint-equation method (McGillivray and Oldenburg 1990). The least-squares equation (1) then needs to be solved to determine the change in the model parameters ($\Delta \mathbf{r}_i$) to reduce the data misfit. The calculation time increases non-linearly with the finite-element mesh size and the number of data points and model parameters. In surveys using a mobile measuring system where the electrodes are on a streamer, the number of electrode positions, data points and model parameters can exceed more than a hundred thousand and the finite-element mesh used might have

1
2
3 more than one million nodes. The calculation of the apparent resistivity and Jacobian
4 matrix for each iteration can exceed a day on inexpensive PCs used by small
5 companies and institutions. The complete inversion of a data set might take more than
6 a week using standard techniques. To reduce the calculation time, we use a ‘divide
7 and conquer’ strategy that subdivides the mesh in a number of smaller meshes
8 (Christiansen and Auken 2004; Loke and Lane 2004).
9

10
11
12
13
14
15
16
17 Another computational problem is the size of the Jacobian matrix \mathbf{J} and the time
18 taken to solve the least-squares equation (1). The \mathbf{J} matrix has n times m array
19 elements, where n is the number of data points and m is the number of model
20 parameters. As an example, a data set with 200,000 data points and a model with
21 150,000 model cells will have a Jacobian matrix with 30,000,000,000 array values. To
22 solve the least-squares equation for such large matrices, the linear conjugate-gradient
23 method together with a data compression technique (using wavelet transforms) is
24 commonly used (Li and Oldenburg 2003; Davis and Li 2013). The inverse models
25 used in this research have a simple arrangement with the model cells arranged in a 3-
26 D rectangular pattern. We describe a simple technique to optimise the wavelet
27 transform method for the model structure used in this research.
28
29
30
31
32
33
34
35
36
37
38
39
40
41
42
43
44
45
46

47 **METHODS TO REDUCE COMPUTER TIME AND MEMORY**

48
49 In this section, we described various methods used to reduce the computer time
50 and memory required for the inversion of very large data sets with hundreds of
51 thousands of electrode positions and data points. The calculations were carried out
52 using a PC with an 18-core Intel W-2195 CPU and 256 GB of RAM.
53
54
55
56
57
58
59
60

Mesh segmentation

Surveys conducted with a mobile resistivity meter system are characterised by arrays having a limited footprint that is proportional to the length of the streamer. Figure 1 shows a schematic diagram of a streamer cable for a 10-channel resistivity meter system using a dipole-dipole arrangement. If the unit electrode spacing is 1 m, the furthest distance between a current and potential electrode is 12 m. The footprint of the system (Tsourlos *et al.* 2014) can be much smaller than the survey area which might be several hundred meters in length. Unlike a survey with a static resistivity meter system, where an array can have electrodes that extend across the entire survey line, the region of the subsurface that affects a measurement using a cable of limited length has a more limited lateral extent compared to the total length of the survey line. This property was previously used (Christiansen and Auken 2004; Loke and Lane 2004; Tsourlos *et al.* 2014) to reduce the calculation time for the inversion of data from long 2-D survey lines. We note that in some surveys a larger spacing might be used between the potential electrodes towards the ~~right end of the line~~ **end of the streamer (such as between electrodes P9 to P11 in Figure 1)** to obtain a stronger signal strength. However, the footprint of the system is still limited by the maximum length of the cable. We extend the segmentation technique to 3-D surveys.

As an example, Figure 2 shows the algorithm used to subdivide a rectangular model grid with 160 by 45 cells in the x and y directions. In the first step (Figure 2a), the model grid is subdivided in 6 approximately equal segments. Next, we mark the data points with at least one electrode in segment 1. The electrode arrays near the boundaries of the segment are likely to have one or more electrodes outside the segment. The boundaries of the segment are next extended (Figure 2b) so that it covers all the electrodes that are used by data points marked earlier. In this example,

1
2
3 the measurements are only made in the x direction, so only the x boundary is
4
5 extended. In surveys with measurements in the y direction, the y boundary is similarly
6
7 extended. In the final step, the boundaries in both the x and y directions are extended
8
9 by 5 to 10 model grid lines (Figure 2c) so that the effect of model cells near edges of
10
11 the segment are included in the calculation of the apparent resistivity and Jacobian
12
13 matrix values for the data points that were marked for this segment. Next, the same
14
15 procedure is used for segment 2 (Figure 2a). The data points that were marked for
16
17 segment 1 are removed from the data set used for determining the data points that fall
18
19 within segment 2 (as well as other segments). Next the boundaries for the remaining
20
21 segments are set one by one using the same procedure. Note this procedure allocates a
22
23 data point to only one segment in the calculation of the apparent resistivity and
24
25 Jacobian matrix values. Figure 3a shows the final boundaries of the 6 segments. There
26
27 is an overlap of 10 model grid lines at the boundaries of the neighbouring segments.
28
29 The overlap minimises discontinuities in the calculated apparent resistivity and
30
31 Jacobian matrix values near the boundaries.
32
33
34
35
36

37
38 To avoid the build-up of artefacts near the edges of the segments, the
39
40 boundaries of the segments are changed after each iteration. In the second iteration of
41
42 the least-squares optimisation method (Figure 3b), the boundaries for segment 1 are
43
44 pushed forward in the x and y directions by 3 model grid lines. At the same time, the
45
46 lower y boundary for segment 2 is pushed upwards in the y direction by 3 model grid
47
48 lines. In the same way, the left x boundary for segment 3 is moved to the right by 3
49
50 model grid lines. In the third iteration (Figure 3c), the boundaries for segment 1 are
51
52 pushed backwards in the x and y directions by 3 model grid lines from the positions in
53
54 the first iteration. In the fourth iteration, the boundaries in the first iteration are used.
55
56
57
58 The algorithm uses the alternating positions of the boundaries in a cyclic manner.
59
60

1
2
3 The segmentation algorithm extends the final boundaries of the segments by at
4 least 5 model grid lines. The widths of the model cells are usually set to be the same
5 as the minimum distance between adjacent electrodes in the streamer. Extending the
6 boundaries to a larger distance should increase the accuracy of the model obtained by
7 the segmentation method (compared to a normal single mesh inversion) but at the cost
8 of larger computer memory and time. To estimate the optimum distance to extend the
9 boundary, we first examine the sensitivity values for a dipole-dipole array survey
10 similar to that used in the synthetic model and field survey discussed in this paper.
11 Figure 4a shows a 3-D plot of the sensitivity values (Fréchet derivative) for a dipole-
12 dipole array with $a=1$ m and $n=10$ for a homogeneous medium that can be calculated
13 analytically (Loke and Barker 1996). The regions with the highest sensitivity values
14 are located near the electrodes. The isosurface plot shows the regions with significant
15 sensitivity values are located near the dipoles and elongated in the direction
16 perpendicular to the axis of the array. Figure 4a shows the model sensitivity
17 distribution for a single array. To study the characteristics of a data set that consists of
18 many arrays, the model resolution is used (Loke *et al.* 2014b). The resolution value of
19 a model cell is limited to between 0.0 (no resolution) to 1.0 (perfect resolution). We
20 calculate the resolution values for a data set from a survey grid with 64 by 23
21 electrodes (Figure 4b), with all the possible dipole-dipole measurements with $a=1$ m
22 and $n=1$ to 10 in the x -direction only (giving a total of 12995 data points). The survey
23 grid and number of electrodes is similar to a single segment in Figure 2. Figure 4b
24 shows a 3-D plot of the resolution values. The subsurface is divided into uniform cells
25 with dimensions of $1.0 \times 1.0 \times 0.5$ m. The maximum resolution value at the surface near
26 the centre of the survey grid is about 0.84. The resolution values gradually decrease
27 with increasing distance from the edge of the survey grid. The band with significant
28
29
30
31
32
33
34
35
36
37
38
39
40
41
42
43
44
45
46
47
48
49
50
51
52
53
54
55
56
57
58
59
60

1
2
3 resolution values is wider at the y boundaries compared to the x boundaries. This is
4
5 because the measurements are only made in the x direction, and the zone with higher
6
7 sensitivity values are elongated in the direction perpendicular to the array axis. Figure
8
9 4c shows the change in the resolution values at the x and y boundaries with distance
10
11 from the boundaries. For the y boundary, the cell at the surface immediately next to
12
13 the boundary has significant resolution value of 0.76. The resolution rapidly decreases
14
15 with distance to about 0.002 at 4.5 m. So, extending the segment boundary up to 5
16
17 times the unit electrode spacing should include all the regions with significant
18
19 resolution values. Figure 4c also shows that the resolution values are lower at the x
20
21 boundary, and also decreases with depth. Field data sets sometimes have
22
23 measurements in both directions, so the boundary is normally extended by the same
24
25 distance in both directions. Most conventional arrays have sensitivity patterns that do
26
27 not extend as far out as the dipole-dipole array (Loke *et al.* 2014b). So, extending the
28
29 segment boundaries to about 5 times the unit electrode spacing is a conservative
30
31 approach that should cover most field surveys situations.
32
33
34
35
36

37
38 The time and taken by the finite-element method increases nonlinearly with
39
40 the number of nodes in the mesh (Christiansen and Auken 2004; Loke and Lane
41
42 2004). Calculating the apparent resistivity values for all the data points using a
43
44 number of smaller sub-meshes takes less time than using a single large mesh for very
45
46 large models that might have more than a million nodes. Another benefit of using
47
48 segments is the reduction in the calculation of the Jacobian matrix values. In the
49
50 standard monolithic inversion approach, the sensitivity values for all the model cells
51
52 are calculated for each data point. In the segmented inversion approach, the sensitivity
53
54 values for only the model cells that fall within the segment are calculated for each
55
56 data point. The average number of model cells in a segment for the grid in Figure 3a
57
58
59
60

1
2
3 is 14960 which is about 26% of the entire model with 57600 cells (with 10 layers).
4
5 For larger model grids, with grid sizes much larger than the overlap between adjacent
6
7 segments, the Jacobian matrix calculation time is usually reduced to about 20%
8
9 compared to the standard single mesh inversion method.
10
11
12
13

14 **Optimising the Jacobian matrix computations for multi-channel systems**

15
16
17 The Jacobian matrix is frequently calculated using the adjoint-equation
18
19 method for resistivity problems (Sasaki 1989; McGillivray and Oldenburg 1990).
20
21 Many modern resistivity meter systems have multi-channel capability where a number
22
23 of simultaneous potential measurements are made for a single injection of the current.
24
25 As an example, the arrangement in Figure 1 makes 10 measurements using the same
26
27 C1-C2 current dipole. This feature can be used to reduce the numerical calculations
28
29 required by the adjoint-equation method to calculate the sensitivity values for the 10
30
31 data points that share the same current electrodes positions. The finite-element
32
33 method is commonly used to calculate the apparent resistivity values for surveys over
34
35 areas with topography (Loke 2000). The potentials are calculated by solving the
36
37 following capacitance matrix equation (Sasaki 1989; Silvester and Ferrari 1990; Loke
38
39 *et al.* 2018).
40
41
42
43

$$44 \quad \mathbf{C}\Phi = \mathbf{s} \quad (2)$$

45
46
47 Φ is a vector that contains the potentials at the nodes of the finite-element grid while \mathbf{s}
48
49 is the current source vector. \mathbf{C} is the capacitance matrix that contains the positions of
50
51 the nodes and the model conductivity values. Figures 5a and 5c show the quadrilateral
52
53 and hexahedral elements used for 2-D and 3-D models. For the following discussion,
54
55 we use the 2-D mesh (Figure 5b) as an example as the matrix structure (Figure 5d) is
56
57
58
59
60

easier to visualise. However, the matrix equations for both the 2-D and 3-D finite-element methods are essentially the same.

Differentiating the capacitance matrix equation (2) with respect to the model cell conductivity σ_k leads to the following relationship.

$$\mathbf{C} \frac{\partial \Phi}{\partial \sigma_k} = - \frac{\partial \mathbf{C}}{\partial \sigma_k} \Phi \quad (3)$$

This equation has the same form as equation (2). All the information required to calculate the sensitivity $\frac{\partial \Phi}{\partial \sigma_k}$ is available in the process of solving equation (2) to calculate the potentials. The matrix $\frac{\partial \mathbf{C}}{\partial \sigma_k}$ is very sparse with only 16 non-zero terms for a 2-D trapezoidal element (Figure 5d). The terms in the capacitance matrix \mathbf{C} consists of the coupling coefficients between the nodes in each element in the mesh (Silvester and Ferrari 1990) and the conductivity of the element. The coupling coefficient between two nodes in an element (Figure 5a) has the following form.

$$c_{pq} = d_{pq}(x, z) \sigma_k \quad (4)$$

The function $d_{pq}(x, z)$ depends only on the coordinates of the four nodes at the corners of the trapezoidal element. The derivative of the coupling coefficient with respect to the element conductivity is thus given by

$$\frac{\partial c_{pq}}{\partial \sigma_k} = d_{pq}(x, z). \quad (5)$$

As the $d_{pq}(x, z)$ terms are calculated in the process of constructing the capacitance matrix \mathbf{C} in equation (2), so it is not necessary to recalculate them for the $\frac{\partial \mathbf{C}}{\partial \sigma_k}$ matrix. In terms of computer program implementation, calculating a member of the $\frac{\partial \Phi}{\partial \sigma_k}$ vector, basically involves the multiplication of a 4 by 4 non-zero sub-matrix

(containing the d_{pq} terms for the mesh element) by the potentials (Φ) at the nodes due to current sources located at the positions of the current electrodes used in the measurement (Figure 5d). This is represented by the following equation.

$$\mathbf{e} = \frac{\partial \mathbf{C}}{\partial \sigma_k} \Phi \quad (6)$$

This produces a vector (\mathbf{e}) with 4 non-zero values that is in turn multiplied by the potentials at the nodes due to current sources located at the positions of the potential electrodes. The calculation of the \mathbf{e} vector requires 16 multiply-add operations for a 2-D quadrilateral element. In total 20 multiply-add operations are required for each mesh element.

For a 3-D hexahedral element, calculating the \mathbf{e} vector involves the multiplication of an 8 by 8 non-zero sub-matrix with a vector which requires 64 multiply-add operations. It is then followed by 8 multiply-add operations to add the potentials at the 8 nodes of the element due to current sources at the potential electrodes giving a total of 72 multiply-add operations. We note that for both the 2-D and 3-D problems, the most time-consuming part is in the calculation of the \mathbf{e} vector in equation (6).

However, the \mathbf{e} vector only involves the current electrodes and is independent of the position of the potential electrodes used in a measurement. If there is a series of measurements that use the same positions of the current electrodes, it is only necessary to calculate the \mathbf{e} vector once and store the values in a temporary array in the computer memory. The temporary array is then used to calculate the Jacobian matrix values for subsequent measurements that use the same current electrodes. As an example, the electrodes arrangement in Figure 1 uses the same C1-C2 current dipole for 10 different measurements. Thus, it is only necessary to directly calculate

1
2
3 the \mathbf{e} vector for the first measurement that uses the C1-C2-P1-P2 electrodes. For the 9
4 subsequent data points (using the C1-C2-P2-P3 until C1-C2-P10-P11 configurations)
5
6 it is not necessary to directly calculate the \mathbf{e} vector which can be retrieved from the
7
8 computer memory. This means that while ~~that~~ the calculation of a **the** sensitivity value
9
10 for the first measurement requires 72 multiply-add operations, the sensitivity values
11
12 for the 9 subsequent measurements require only 8 multiply-add operations each. This
13
14 reduces the total number of multiply-add operations for the 10 data points from 720 to
15
16 144 which reduces the calculation time by about 80% for 3-D problems.
17
18
19
20

21 It was noted by Loke *et al.* (2015) in the study of optimised arrays that for
22 some data sets the number of independent current-potential (C-P) pairs can be much
23
24 less than the number of data points. This was used to greatly reduce the calculation
25
26 time to generate the optimised arrays. The same technique can be used to further
27
28 reduce the calculation time for the Jacobian matrix for data sets where the number of
29
30 unique C-P pairs is much less than the number of data points. However, the benefit of
31
32 using this technique is highly data dependent. For surveys that use the same current
33
34 electrodes for a large number of data points (Blome *et al.* 2011) using a resistivity
35
36 meter with a large number of channels this can be highly beneficial. For some data
37
38 sets, such as those using the Wenner array or the Lambayana field data set
39
40 (following section), it can be slower. The expected reduction (or increase) in
41
42 computer time using this technique can be estimated by calculating the number of
43
44 unique C-P pairs versus the number of data points.
45
46
47
48
49
50

51 These techniques to reduce the Jacobian matrix calculation time for parallel
52
53 measurements are general in nature and can also be used for standard inversion using
54
55 a single mesh, as well as for other geophysical methods such as EM surveys that use a
56
57 number of receivers for a single source position.
58
59
60

1
2
3 The calculation of the Jacobian matrix requires the largest amount of computer
4 memory during the inversion process. If the number of electrodes used in the survey
5 is n_e and the number of nodes in the mesh is n_m , the total number of potential values is
6 $n_e \cdot n_m$. The synthetic model example used in this paper (following section) has 7406
7 electrodes and the finite-element mesh has 811,980 nodes. If the potentials are stored
8 as 4-byte single precision values, the computer memory needed to store all the
9 potential values is 22.4 GB. If the mesh is divided into 6 segments, the average
10 number of electrodes and nodes in a segment are 1,418 and 267,320 respectively.
11 Thus, the average amount of computer memory required by the segmentation method
12 is about 1.4 GB which is 6.3% of that used by the standard monolithic approach. If
13 the computer memory available is less than that required, it is still possible to
14 calculate the Jacobian values by reading the potential values associated with the 4
15 electrodes used for each data point from the computer hard-disk when required.
16 However, this is much slower than loading all the potential values into the computer
17 memory where they can be accessed more rapidly.
18
19
20
21
22
23
24
25
26
27
28
29
30
31
32
33
34
35
36
37
38
39

40 **Reducing the computer time and memory to solve the least-squares equation**

41
42 The Jacobian matrix \mathbf{J} encountered for large surveys with hundreds of
43 thousands of data points and model cells can have billions of array values. For such
44 large scale problems, the iterative linear conjugate-gradient method is commonly used
45 to solve the least-squares equation (1) to determine the change in the model
46 parameters $\Delta \mathbf{r}_i$. Solving the least-squares equation using the linear conjugate gradient
47 method involves matrix vector multiplications of the form $\mathbf{J}^T \mathbf{a}$ and $\mathbf{J} \mathbf{b}$. The size of the
48 Jacobian matrix presents two computational problems. The first involves the
49 computer time required for the matrix-vector multiplications. The second problem is
50
51
52
53
54
55
56
57
58
59
60

1
2
3 that the size of the Jacobian matrix might exceed the computer memory. Both
4
5 problems were solved by using the wavelet transform to compress the Jacobian matrix
6
7 by retaining only the components with significant amplitudes (Li and Oldenburg
8
9 2003; Davis and Li 2013). The arrangement of model cells used in this research has a
10
11 simple 3-D rectangular pattern (Figure 5) so a simple algorithm can be used to
12
13 optimise the use of the wavelet transform. The sensitivity values associated with an
14
15 electrode measurement configuration is a 3-D function of the (x,y,z) coordinates of the
16
17 model cells. We take advantage of the regular arrangement of the model cells, and the
18
19 property that sensitivity values change in a smooth manner between neighbouring
20
21 cells, to convert the 3-D sensitivity function to a 1-D function of the cell index
22
23 number (Figure 6) so that a simple 1-D wavelet transform can be used. As an
24
25 example, Figure 7a shows the Jacobian vector for a single pole-dipole array on the
26
27 surface of a model with a 15 by 15 m rectangular grid and 7 layers plotted as a 1-D
28
29 function of the cell index number. The Jacobian vector has the largest amplitudes at
30
31 the model cells that are closest to the electrodes, with the amplitudes decreasing with
32
33 each deeper layer. The shift in the position of the sensitivity pattern between layers is
34
35 due to the zigzag model cell numbering scheme used (Figure 6). The fast wavelet
36
37 transform using the Daubechies 4 wavelet (Daubechies 1988; Press *et al.* 2007) was
38
39 used to calculate the wavelet components (Appendix). The wavelet components plot
40
41 (Figure 7d) shows that most of them have very small amplitudes. If components with
42
43 amplitudes of less than 0.5% of the largest are removed, the reconstructed sensitivity
44
45 (using the inverse wavelet transform) plot still closely matches the original plot
46
47 (Figures 7a and 7b). Figure 7c shows a plot of the difference between the original and
48
49 reconstructed Jacobian values. Note the vertical scale used for this plot is 100 times
50
51 smaller compared to Figures 7a and 7b. If the same scale is used, the plot will appear
52
53
54
55
56
57
58
59
60

1
2
3 as a flat line. The maximum amplitude of the difference is about 200 times smaller (or
4
5 0.5%) than the maximum Jacobian value.
6
7

8 For very large models with hundreds of thousands of model cells, the 1-D
9
10 wavelet transform reduces the size of the Jacobian matrix by more than 100 times. As
11
12 an example, the Jacobian matrix for the Lambayanna field data set (following section)
13
14 has 69,464,915,000 elements, or about 259 GB of computer memory (using a 4-byte
15
16 single precision array) which exceeds the memory of the PC used. This was reduced
17
18 to 139,579,108 values if only the wavelet components with amplitudes that exceed
19
20 0.5% of the maximum amplitude are retained. This is nearly 500 times smaller than
21
22 the full Jacobian matrix. The computer memory required is slightly over 1 GB
23
24 (including an auxiliary 4-byte integer array with the index values of the retained
25
26 wavelet components). The time taken by the fast wavelet transform and to solve the
27
28 least-squares equation using the sparse transformed Jacobian matrix is less than 10%
29
30 of the time taken by the finite-element routine to calculate the potentials and Jacobian
31
32 matrix values.
33
34
35
36
37
38
39
40
41

42 **RESULTS**

43 44 45 **Synthetic model test**

46
47 We use a synthetic model with 8 blocks embedded in the upper layer of a two-
48
49 layer medium (Figure 8). The electrodes are arranged in a 1610 by 460 m rectangular
50
51 grid with a 10 m spacing in both the x and y directions for a total of 7,406 electrodes
52
53 (Figure 2). The test data set consists of the dipole-dipole array measurements with the
54
55 dipole length $a=10$ m, and dipole spacing values n of 1 to 10 with only measurements
56
57
58
59
60

made in the x -direction. This gave a data set with 70,610 measurements while the inverse model with 10 layers has 57,600 cells. The main purpose of the synthetic data set is to check the accuracy of the segmentation inversion algorithm compared to the standard single mesh inversion. Gaussian random noise with an amplitude of 0.05 m Ω was added to the calculated resistance values (with a range of 0.54 to 355.18 m Ω) before they were converted to apparent resistivity values (Zhou and Dahlin 2003). This resulted in an average noise level of about 1.5% in the apparent resistivity values. The mesh was divided into 6 segments with the boundaries cutting across blocks 1, 3, 6, 7 and 8.

Figure 9a shows the inverse model using the standard inversion method with a single mesh that has a data misfit of 1.5%, which is the same as the added noise. The inverse model using the segmented mesh (Figure 9b) is nearly identical to that obtained with a single mesh and has the same data misfit. The edges of the segments were extended by 5 cells in both the x and y directions. In algorithms that do not calculate the Jacobian values for all model cells for each data point (Christiansen and Auken 2004; Loke and Lane 2004; Papadopoulos *et al.* 2011), the Jacobian values that are not directly calculated are normally set to zero in advance omitting their respective calculation. In this paper, we also test the results when the Jacobian values for these cells are approximated by using the values for a homogeneous half-space that can be calculated analytically (Loke and Barker 1996).

To numerically assess the accuracy of the segmented mesh model, the percentage relative difference at cell j between the resistivity of the models using standard monolithic (r_1) and segmented mesh (r_2) inversions was calculated using the following equation.

$$\partial(j) = 100 \cdot [r_2(j) - r_1(j)] / r_1(j) \quad (7)$$

The average percentage relative difference (∂_a) was then calculated using the following equation.

$$\partial_a = \left[\sum_1^m |\partial(j)| \right] / m \quad (8)$$

m is the number of model cells. The average difference between the model resistivity values obtained using the segmentation algorithm and normal monolithic inversion is 0.2% (Table 1). The maximum difference of 1.8% occurs in Layer 9 (not shown) which is probably due to the decrease in resolution with depth. There are no visible artefacts where the segment boundaries cut across the blocks in the upper layer. We also carried out an inversion with the fixed segment boundaries (instead of changing the boundaries after each iteration). The resulting model resistivity values also had an average difference of 0.2% but the maximum difference was higher at 2.4%.

Figure 9c shows the inverse model using the segmentation algorithm with the Jacobian values for the cells outside the segments truncated to zero. The average difference in the model values is essentially the same as for Figure 9b (to within 0.05%) but the maximum difference is slightly higher at 2.3%. For the final test, the width of the buffer zone at the edges of the segments was extended to 8 model cells with the Jacobian values outside the segments also truncated to zero (Figure 9d). This gave a maximum difference of 1.6% that is marginally lower (Table 1) compared to that obtained using a buffer zone of 5 model cells and a homogeneous model Jacobian approximation for the external cells.

We note that the models using the segmentation algorithm are visually identical to that obtained using standard monolithic inversion. The average difference of about 0.2% in the model resistivity values is small compared to the noise level of 1.5% added to the data. Padding the Jacobian matrix with approximate values from a

1
2
3 homogeneous half-space does result in a slightly lower maximum difference when a
4 narrower buffer zone is used. In cases where the approximate Jacobian is not suitable
5 and the values are truncated to zero, using a wider buffer zone gave similar results at a
6 cost of a slight increase in computer time (Table 1).
7
8
9
10

11
12 The different implementations of the segmentation algorithm reduce the
13 calculation time by about 30% to 40% (Table 1). This is a relatively small data set
14 with 7,406 electrodes, 70,610 data points and 57,600 model cells. There is a
15 significant overlap between the different segments compared to the overall model grid
16 size so the reduction in the computer time is relatively modest compared to larger data
17 sets.
18
19
20
21
22
23
24
25
26
27

28 **Lambayanna field survey data set**

29
30 Figure 10a shows the layout from a survey in a prehistoric submerged
31 archaeological site in central Greece using a mobile streamer dragged along the sea
32 bottom below the sea surface in a depth ranging from 0.9 m to 5.3 m and an average
33 depth of 2.7 m (Oikonomou *et al.* 2019). The dipole-dipole array with dipole length a
34 = 1 m and n values from 1 to 10 was used. There are 215,875 electrode positions and
35 164,414 data points in this data set. The survey lines, inverse model grid and
36 segments used are shown in Figure 10b. Many of the survey lines crisscross each
37 other such that several electrodes from different survey lines are located close to one
38 another. In cases where the electrode does not coincide with a node in the finite-
39 element mesh, an interpolation method is used (Spitzer *et al.* 1999; Loke *et al.*
40 2013b). The potential at the position of the electrode is estimated from the potentials
41 at the four nearest nodes in the mesh (and similarly a current electrode is replaced by
42 four equivalent current sources). The top 5 levels of the finite-element mesh are used
43
44
45
46
47
48
49
50
51
52
53
54
55
56
57
58
59
60

1
2
3 to model the water layer where the resistivities of the cells are fixed using the
4 measured seawater value of $0.17 \Omega\text{m}$ (Dahlin and Loke 2018). The z position of the
5
6 measured seawater value of $0.17 \Omega\text{m}$ (Dahlin and Loke 2018). The z position of the
7
8 5th node from the top of the mesh is set at the measured depth of the seabed at the
9
10 particular (x,y) position.
11

12 The model grid used for the data inversion has 131 by 326 cells with widths of
13
14 1 m in both the x and y directions and 10 layers giving a total of 422,500 model cells.
15
16 The thickness of the first layer is set at the minimum depth of investigation (Edwards
17
18 1977) of the data set. The thickness of each deeper layer is increased by 15% since the
19
20 data resolution decreases with depth. The maximum depth of investigation of the data
21
22 set is used as a guide to set the depth to the bottom layer. Figure 11a shows the top 6
23
24 layers of the model with the standard monolithic inversion approach using a single
25
26 finite-element mesh with 9,675,548 nodes. The mesh has 419, 1004 and 23 nodes
27
28 respectively in the x , y and z directions. Out of the 23 nodes in the z direction, 5
29
30 nodes are used to model the water layer while 7 nodes are used for the bottom section
31
32 of the mesh below the last model layer. The spacing between the 7 bottom mesh lines
33
34 are progressively increased so that the last mesh line is sufficiently far away from the
35
36 electrodes (Dey and Morrison 1979). The remaining 11 nodes are used for the 10
37
38 model layers with the top layer (which is closest to the electrodes) subdivided in two
39
40 mesh lines. Figure 12 shows a 3-D plot of the model for the sediments below the
41
42 water layer. As the water layer resistivity is fixed, it is not shown in the model plots.
43
44 The archaeological features of interest are represented by the higher resistivity
45
46 anomalies on the left side of the sections (that is located further from the shoreline) in
47
48 the top 3 layers. The inversion took about 327,777 seconds (91.0 hours). The data
49
50 misfit of 10.8% is higher than most land surveys using a conventional 'static' multi-
51
52 electrode resistivity meter system with the electrodes planted in the ground. This is
53
54
55
56
57
58
59
60

1
2
3 probably partly due to the challenging marine environment with very conductive
4 seawater and the continuous movement of the cable during the survey. Nevertheless,
5 the resistivity model agrees with known archaeological information and the results
6 from other geophysical surveys (Oikonomou *et al.* 2019).
7
8
9

10
11
12 Figure 11b shows the model obtained using the segmentation algorithm with 8
13 segments. A buffer zone with 8 model cells was used for the segments. It was
14 observed that the sensitivity values for model cells outside the segments calculated
15 using the adjoint equation method (from the single mesh inversion) differ
16 significantly from approximate values using a homogeneous model. This is probably
17 because of the large contrast between the seawater and the subsurface materials. The
18 Jacobian values for the cells outside the segments were thus truncated to zero in the
19 inversion process, and a wider buffer zone was used for the segments. There are no
20 significant differences in the models using the standard monolithic and segmentation
21 inverse method (Figures 11a and 11b) that also has a data misfit of 10.8%. The
22 average difference in the model resistivity values is 0.7%. The maximum difference
23 of 3.9% occurred for a cell in the 9th layer which is probably due to the decrease in the
24 resolution with depth. The calculation time was 52,731 seconds (14.6 hours), or a
25 reduction of about 84% compared to the standard approach. The average number of
26 model cells in a segment is 78,485 (about 19% of the whole model).
27
28
29
30
31
32
33
34
35
36
37
38
39
40
41
42
43
44
45

46
47 We also carry out a test with an alternative approach where the positions of the
48 electrodes were rounded up (Oikonomou *et al.* 2019), or binned, to the nearest 0.5 m
49 (i.e. half the electrode spacing). This reduced the number of electrode positions to
50 87,245 (about 40% of the original data set). An inversion of the data set with the
51 modified electrode positions was carried out using the normal approach with a single
52 finite-element mesh. Figure 11c shows the inverse model which is fairly similar to
53
54
55
56
57
58
59
60

1
2
3 that obtained using the electrodes in their true positions (Figure 11a) with a slightly
4 higher data misfit of 10.9%. The average relative difference in the model values was
5 slightly higher at 1.1% compared to the segmentation method. The largest differences
6 were found in the top layer. A relatively high maximum difference of 46.6% was
7 obtained for a cell in the top layer. This was probably caused by arrays where the
8 electrodes are not equally spaced due to bending of the cable during the survey. This
9 caused ~~Consequently~~, the electrodes in some configurations ~~to be~~ were shifted by
10 different amounts with the binning procedure. This ~~causes~~ resulted in significant
11 changes in the characteristics of the electrode array compared to the true
12 configuration. The binning procedure reduced the calculation time by about 51%
13 which is less than that obtained with the segmentation method.
14
15
16
17
18
19
20
21
22
23
24
25
26
27
28
29
30
31
32

33 DISCUSSION

34
35 The use of segments to reduce the calculation time is designed for the
36 inversion of very large data sets with limited computational resources. This situation
37 is frequently encountered by small geophysical companies using personal computers
38 or workstations. In general, a conservative approach is followed that uses the
39 minimum number of segments so that the inversion can be carried out with the
40 available computer resources. It is recommended that the length of a segment should
41 not be less than 5 times the ~~maximum distance between two electrodes in an array~~
42 length of the streamer for arrays aligned along the same direction as the side of the
43 segment. As an example, in Figure 11 most of the measurements are in the y-direction
44 using a streamer of 12 metres. Thus, the length of the segments in the y-direction
45 should be at least 60 metres. It is also recommended that the length of a segment in
46
47
48
49
50
51
52
53
54
55
56
57
58
59
60

1
2
3 one direction should be not be more than twice the length in the other direction.
4

5 However, the size and number of segments that provides an optimum balance
6
7 between reducing the calculation time and accuracy of the results is an area that
8
9 requires further research.
10
11
12
13
14
15
16

17 CONCLUSIONS

18
19 Surveys using mobile systems can produce very large data sets with hundreds
20
21 of thousands of electrode positions and data points. The model used can have
22
23 hundreds of thousands of cells with a finite-element mesh of more than one million
24
25 nodes. The segmentation method has proved to be an effective method that reduces
26
27 the calculation time by more than 80% for very large data sets while producing
28
29 models with an average difference of less than 1% from that produced by the standard
30
31 monolithic approach. An alternative method, binning the electrodes to discrete
32
33 positions, has the advantage that it is relatively easy to implement. However, in field
34
35 data sets from mobile surveys where bending of the cable is common, this can cause
36
37 larger errors in parts of the inverse model (particularly near the surface) compared to
38
39 the segmentation method. The segmentation method is faster but more difficult to
40
41 implement. It has been used successfully for surveys with more than half a million
42
43 electrode positions (Unrau 2019). This makes it practical to carry out the inversion of
44
45 very large data sets on common and inexpensive microcomputers used by small
46
47 companies and institutions.
48
49
50
51
52
53

54 We are currently investigating other techniques to further reduce the
55
56 calculation time such as directly calculating the Jacobian values at selected cells
57
58 within a segment that are likely to have significant amplitudes (Papadopoulos *et al.*
59
60

1
2
3 2011) and using a homogeneous model approximation for the rest. We are also
4 examining ways to adapt the techniques described in Yang *et al.* (2014), such as the
5 use of local meshes and data subsets, to further reduce the computer time and memory
6 required to process very large resistivity data sets.
7
8
9
10
11
12
13
14
15
16

17 ACKNOWLEDGEMENTS

18
19 The authors from GeoSat ReSeArch lab express their acknowledgements to Dr. Julien
20 Beck for the fruitful and constructive collaboration in the 2016-2019 during the
21 archaeological project in the Bay of Kiladha which a collaboration between the
22 University of Geneva, under the aegis of the Swiss School of Archaeology in Greece,
23 and the Greek Ephorate of Underwater Antiquities. The collection of the marine ERT
24 data in Lambayanna was completed in 2018 under the collaboration of the GeoSat
25 ReSeArch Lab with the Ephorate of Underwater Antiquities, the Swiss
26 Archaeological School and the University of Geneva. Wilkinson publishes with the
27 permission of the Executive Director, British Geological Survey (UKRI-NERC). We
28 would like to thank two anonymous reviewers and the Associate Editor for their
29 constructive comments that have helped to improve the paper.
30
31
32
33
34
35
36
37
38
39
40
41
42
43
44
45
46
47
48

49 References

50
51 Blome, M., Maurer, H. & Greenhalgh, S., 2011. Geoelectric experimental design -
52 Efficient acquisition and exploitation of complete pole-bipole data sets.
53 *Geophysics*, **76**, F15–F26.
54
55
56
57
58
59
60

- 1
2
3 Christiansen A.V., and Auken E., 2004. Optimizing a layered and laterally
4 constrained 2D inversion of resistivity data using Broyden's update and 1D
5 derivatives. *Journal of Applied Geophysics*, **56**, 247-262.
6
7
8
9
10 Dahlin, T. and Loke, M.H., 2018. Underwater ERT surveying in water with resistivity
11 layering with example of application to site investigation for a rock tunnel in
12 central Stockholm. *Near Surface Geophysics*, **16**, 230-237.
13
14
15
16
17 Daubechies I., 1988. Orthonormal bases of compactly supported wavelets. *Commun.*
18 *Pure Appl. Math.*, **41(7)**, 909–996.
19
20
21
22 Davis K. and Li K., 2013. Efficient 3D inversion of magnetic data via octree-mesh
23 discretization, space-filling curves, and wavelets. *Geophysics*, **78**, 1942-2156.
24
25
26 deGroot-Hedlin C. and Constable S., 1990. Occam's inversion to generate smooth,
27 two-dimensional models from magnetotelluric data. *Geophysics*, **55**, 1613-
28 1624.
29
30
31
32
33 Dey, A. & Morrison, H.F., 1979. Resistivity modeling for arbitrarily shaped three-
34 dimensional structures. *Geophysics*, **44**, 615–632.
35
36
37
38 Edwards L.S., 1977. A modified pseudosection for resistivity and induced-
39 polarization. *Geophysics*. **42**, 1020-1036.
40
41
42
43 Farquharson C.G. and Oldenburg D.W., 1998. Nonlinear inversion using general
44 measures of data misfit and model structure. *Geophysical Journal*
45 *International*, **134**, 213-227.
46
47
48
49 Farquharson C.G. and Oldenburg D.W., 2004. A comparison of automatic techniques
50 for estimating the regularization parameter in non-linear inverse problems.
51 *Geophysical Journal International*, **156**, 411-425.
52
53
54
55
56
57
58
59
60

- 1
2
3 Hildes D., Dziuba F. and Power M., 2005. Kimberlite Exploration Using a
4 Capacitive-Coupled Resistivity System. *Proceedings of 2005 CSEG National*
5
6 *Convention*, May 16-19 2005, Calgary, Canada, 393-395.
7
8
9
10 Kuras O., Beamish D., Meldrum P.I., and Ogilvy R.D., 2006. Fundamentals of the
11
12 capacitive resistivity technique. *Geophysics*, **71**, G135–G152.
13
14
15 Li, Y. and Oldenburg, D.W., 2000. 3-D inversion of induced polarization data.
16
17 *Geophysics*, **65**, 1931-1945.
18
19
20 Li Y. and Oldenburg D.W., 2003. Fast Inversion of large-scale magnetic data using
21
22 wavelet transforms and logarithmic barrier method. *Geophysical Journal*
23
24 *International*, **152**, 251 - 265.
25
26
27 Loke M.H. and Barker R.D., 1996. Practical techniques for 3D resistivity surveys and
28
29 data inversion. *Geophysical Prospecting*, **44**, 499-523.
30
31
32 Loke M.H., 2000. Topographic modelling in resistivity imaging inversion. 62nd
33
34 EAGE Conference & Technical Exhibition Extended Abstracts, D-2.
35
36
37 Loke M.H., Acworth I. and Dahlin T., 2003. A comparison of smooth and blocky
38
39 inversion methods in 2D electrical imaging surveys. *Exploration Geophysics*,
40
41 **34**, 182-187.
42
43
44 Loke M.H. and Lane J.W., 2004. Inversion of data from electrical resistivity imaging
45
46 surveys in water-covered areas. *Exploration Geophysics*, **35**, 266-271.
47
48
49 Loke M.H., Chambers J.E., Rucker D. F., Kuras O. and Wilkinson P. B., 2013a.
50
51 Recent developments in the direct-current geoelectrical imaging method.
52
53 *Journal of Applied Geophysics*, **95**, 135-156.
54
55
56 Loke, M.H., Frankcombe, K. and Rucker, D.F., 2013b. The inversion of data from
57
58 complex 3-D resistivity and I.P. surveys. 23rd International Geophysical
59
60 Conference and Exhibition, 11-14 August 2013 - Melbourne, Australia.

1
2
3 Loke M.H., Dahlin T. and Rucker D.F., 2014a. Smoothness-constrained time-lapse
4 inversion of data from 3-D resistivity surveys. *Near Surface Geophysics*, **12**,
5 5-24.
6
7
8

9
10 Loke, M.H., P. B. Wilkinson, P.B., Uhlemann, S.S., Chambers, J.E. and Oxby, L. S.,
11 2014b. Computation of optimized arrays for 3-D electrical imaging surveys.
12 *Geophysical Journal International*, **199**, 1751-1764
13
14

15
16 Loke M.H., Wilkinson P.B., Chambers J.E., Uhlemann S.S. and Sorensen J.P.R.,
17 2015. Optimized arrays for 2-D resistivity survey lines with a large number of
18 electrodes. *Journal of Applied Geophysics*, **112**, 136-146.
19
20
21
22

23
24 Loke M.H., Wilkinson P.B., Chambers J. E. and Meldrum P.I., 2018. Rapid inversion
25 of data from 2-D resistivity surveys with electrodes displacements.
26 *Geophysical Prospecting*, **66**, 579-594.
27
28

29
30 McGillivray P.R. and Oldenburg D.W. 1990. Methods for calculating fréchet
31 derivatives and sensitivities for the non-linear inverse problem : a comparative
32 study. *Geophysical Prospecting*, **38**, 499-524.
33
34
35
36

37
38 Oikonomou D., Papadopoulos N., Simyrdanis K., Cantoro G., Beck J. and Loke M.H.,
39 2019. Processing strategies for 3-D marine dynamic electrical resistivity
40 tomography data. 13th International Conference on Archaeological Prospection,
41 28 August to 1 September 2019, Sligo, Ireland.
42
43
44
45

46
47 Papadopoulos, N.G., Tsourlos P., Papazachos C., Tsokas G.N., Sarris A. and Kim
48 J.H., 2011. An algorithm for fast 3D inversion of surface electrical resistivity
49 tomography data: application on imaging buried antiquities. *Geophysical*
50 *Prospecting*, **59**, 557-575.
51
52
53
54

55
56 Press, W.H, Teukolsky, S.A., Vetterling, W.T. and Flannery, B.P., 2007. Numerical
57 Recipes: The Art of Scientific Computing (3rd Edition). Cambridge University
58
59
60

- 1
2
3 Press.
4
5
6 Rucker, D.F., Levitt, M.T. and Greenwood, W.J., 2009. Three-dimensional electrical
7
8 resistivity model of a nuclear waste disposal site. *Journal of Applied*
9
10 *Geophysics*, **69**, 150-164.
11
12 Rucker D.F. and Noonan G.E., 2013. Using marine resistivity to map geotechnical
13
14 properties: a case study in support of dredging the Panama Canal. *Near*
15
16 *Surface Geophysics*, **11**, 625-637.
17
18 Sasaki Y., 1989, Two-dimensional joint inversion of magnetotelluric and dipole-
19
20 dipole resistivity data. *Geophysics*, **54**, 254-262.
21
22
23 Silvester P.P. and Ferrari R.L., 1990. Finite elements for electrical engineers (2nd.
24
25 ed.). Cambridge University Press.
26
27
28 Simyrdanis K., Papadopoulos N., Kim J.H., Tsourlos P. and Moffat I., 2015.
29
30 Archaeological Investigations in the Shallow Seawater Environment with
31
32 Electrical Resistivity Tomography. *Journal of Near Surface Geophysics*,
33
34 *Integrated geophysical Investigations for Archaeology*. **13**, 601- 611.
35
36
37 Spitzer K., Chouteau M. and Boulanger O. 1999, Grid-independent electrode
38
39 positioning for 3D DC and IP forward modelling. Proc. 2nd. Internat. Sym. 3D
40
41 Electromagnetics, 189–192.
42
43
44 Tsourlos P., Papadopoulos N., Papazachos C., Yi M.Y. and Kim J.H., 2014. Efficient
45
46 2D inversion of long ERT sections. *Journal of Applied Geophysics*, **105**, 213-
47
48 224.
49
50
51 Unrau T., 2019. Towed Capacitively Coupled Resistivity Systems in Arctic
52
53 Exploration - Advances in Equipment Design and Handling of Very Large
54
55 Resistivity Surveys. AGU 100 Fall Meeting, San Francisco, 9-13 Dec. 2019,
56
57 NS22A-07.
58
59
60

Xu, T. and Dunbar, J.A., 2015. Binning method for mapping irregularly distributed continuous resistivity profiling data onto a regular grid for 3-D inversion.

Journal of Environmental and Engineering Geophysics, **20**, 1-17.

Yang, D., Oldenburg, D.W. and Haber, E., 2014. 3-D inversion of airborne electromagnetic data parallelized and accelerated by local mesh and adaptive soundings. *Geophysical Journal International*, **196**, 1492–1507.

Zhou B. and Dahlin, T., 2003. Properties and effects of measurement errors on 2D resistivity imaging surveying. *Near Surface Geophysics*, **1**, 105-117.

Appendix : Using the Discrete Wavelet Transform

This section describes the practical use of the Discrete Wavelet Transform (DWT). While the Fast Fourier Transform (FFT) is based on the sine and cosine functions, the DWT is based on the ‘mother wavelet’ function (Daubechies 1992). The sine and cosine functions are localised in frequency (but not in space or time). In comparison, the wavelet functions are localised both in frequency and space. This makes them useful for functions such as the Jacobian data series (Figure 7a) that exhibit a quasi-periodic structure over a limited interval near the electrodes. Press *et al.* (2007) gives a description of the wavelet functions, together with wavelet filter coefficients and computer code to carry out the wavelet transform. Like the FFT, the computer implementation of the DWT is optimized for a data vector where the number of points is an integer power of 2. The number of model cells for the example in Figure 7a is 1575. In calculating the DWT, the data series is extended to 2048 by padding the end with zeros. The time taken by the DWT is proportional to $m.\log(m)$ where m is the length of the data vector. The time taken by the DWT to calculate the transform for

1
2
3 the Jacobian matrix is only a few percent of the overall time taken to invert the data
4
5 set. It is in fact less than time taken to read the Jacobian values from (and write the
6
7 transformed values to) the computer hard-disk.
8
9
10
11
12
13
14
15
16
17
18
19
20
21
22
23
24
25
26
27
28
29
30
31
32
33
34
35
36
37
38
39
40
41
42
43
44
45
46
47
48
49
50
51
52
53
54
55
56
57
58
59
60

List of figure captions

Figure 1. Schematic diagram of a mobile streamer. C1 and C2 are the current electrodes while P1 to P11 are the potential electrodes.

Figure 2. Method used to subdivide a model with 160 by 45 cells (of 10 m width in the x and y directions) in each layer subdivided into 6 segments. (a) Initial subdivision into 6 segments of approximately equal size. The dark blue line marks the region covered by segment 1. (b) Extending the boundary (medium blue line) of segment 1 so that it includes all the electrodes for data points in this segment. (c) Adding a buffer zone around the segment to minimise edge effects. The final region covered by segment 1 is shown by the light blue line.

Figure 3. (a) The initial regions of the model grid covered by the 6 segments used in iteration 1 of the least-squares optimisation algorithm. Note the overlaps between neighbouring segments. (b) Shifting of the boundaries of the segments forwards by 3 model grid lines (compared to those used in iteration 1) in iteration 2. (c) Shifting of the boundaries of the segments backwards by 3 model grid lines (compared to those used in iteration 1) in iteration 3.

Figure 4. (a) 3-D plot of sensitivity values for the dipole-dipole array with $a=1$ m and $n=10$. The electrodes are located at x positions of 0, 1, 11 and 12 along the $y=0$ axis. The isosurface for sensitivity value of 0.01 is shown. (b) Plot of resolution values for a dipole-dipole array survey with $a=1$ m and $n=1$ to 10 with electrodes in a 64 by 23 grid. The 0.005 isosurface is shown. The electrodes are marked by black dots on the surface. (c) Change of resolution with distance from edge of survey grid at the x and y

1
2
3 boundaries. The resolution values of cells at the mid-point of the x and y boundaries
4
5 (which have the highest values) are shown.
6
7
8
9

10 Figure 5. (a) 2-D quadrilateral element with 4 nodes. (b) Example 2-D finite-element
11 mesh with node numbers. (c) 3-D hexahedral element with 8 nodes. (d) Schematic
12 diagram of the structure of the capacitance matrix equation for the 2-D mesh with the
13 non-zero elements. D represents a diagonal element while X represents a non-zero
14 off-diagonal element. The members of the $\frac{\partial \mathbf{C}}{\partial \sigma_k}$ matrix (due to a change in the
15 conductivity of the k mesh cell) that have non-zero values are marked in red.
16
17
18
19
20
21
22
23
24
25
26

27 Figure 6. Numbering of model cells arranged in a 3-D rectangular grid so that the
28 Jacobian matrix which is a 3-D function of (x,y,z) is converted to a continuous 1-D
29 function of the model cell index k .
30
31
32
33
34
35

36 Figure 7. (a) Plot of the Jacobian values for a single pole-dipole array ($a = 2, n = 1$)
37 for a model with $15 \times 15 \times 7$ model cells (each layer has 225 cells). (b) The
38 reconstructed Jacobian values after wavelet components with amplitudes of less than
39 0.5% of the maximum value were removed. (c) Plot of the difference between the
40 original and reconstructed Jacobian values. Note the vertical scale is 100 times
41 smaller than (a) and (b). (d) Plot of the wavelet components. ~~The quantity~~ Values
42 in vertical axis in the plots is are dimensionless. The horizontal axis is the model cell
43 index number in (a), (b) and (c), and the wavelet wave number in (d).
44
45
46
47
48
49
50
51
52
53
54
55

56 Figure 8. Synthetic model with 8 blocks in the upper layer of a two-layer medium.
57 The top layer (transparent in the plot) has a resistivity of $30 \Omega \cdot \text{m}$ and a thickness of
58
59
60

1
2
3 23.2 m. Blocks 1 to 5 have a depth range of between 0.0 and 5.0 m, while blocks 6 to
4
5 8 have a depth range of 5.0 and 10.5 m. Blocks 1 to 5 extend from the surface (0.0 m)
6
7 to a depth of 5.0 m. The top of blocks 6 to 8 is at 5.0 m while the bottom is at 10.5 m
8
9 depth.
10
11
12
13

14 Figure 9. Inverse models of synthetic data set with (a) standard monolithic inversion,
15
16 (b) using 6 segments with buffer zone of 5 model cells and homogeneous Jacobian
17
18 approximation for external cells, (c) using segments with buffer zone of 5 model cells
19
20 and truncated Jacobian for external cells and (d) using segments with buffer zone of 8
21
22 model cells and truncated Jacobian for external cells. The blocks in the synthetic
23
24 model are shown by black outlines in the first 2 layers.
25
26
27
28
29

30 Figure 10. Lambayanna survey (a) map and (b) inverse model grid (segments shown
31
32 by coloured grid lines).
33
34
35

36
37 Figure 11. Lambayanna survey inverse models using (a) standard monolithic
38
39 inversion with a single mesh, (b) 2 by 4 segmented mesh and (c) electrodes binned to
40
41 every 0.5 m.
42
43
44
45

46 Figure 12. 3-D plot of Lambayanna survey inverse model below the water layer.
47
48
49
50
51
52
53
54
55
56
57
58
59
60

1
2
3 **List of table captions**
4
5
6
7

8 Table 1. Comparison of different methods for the inversion of the synthetic model
9 data set. All the models have the same data misfit of 1.5%.
10
11
12

13
14 Table 2. Comparison of different methods for the inversion of the Lambayanna field
15 data set.
16
17
18
19
20
21
22
23
24
25
26
27
28
29
30
31
32
33
34
35
36
37
38
39
40
41
42
43
44
45
46
47
48
49
50
51
52
53
54
55
56
57
58
59
60

Table 1. Comparison of different methods for the inversion of the synthetic model data set. All the models have the same data misfit of 1.5%.

Inverse method	Inversion Time (s)	% model difference Average (max)	Memory required by adjoint-equation method (GB)
Single mesh	3,449		22.4
Segments with homogeneous Jacobian approximation for external model cells	2,140	0.2 (1.8)	1.4
Segments with truncated Jacobian for external model cells	2,025	0.2 (2.3)	1.4
Segments with wider buffer zone and truncated Jacobian for external model cells	2,512	0.2 (1.6)	1.6

Table 2. Comparison of different methods for the inversion of the Lambayanna field data set.

Inverse method	Number of electrodes	Inversion Time (s)	% model difference Average (max)	Data misfit (%)
Single mesh	215,873	327,777		10.8
Segments with 8 m buffer zone	215,873	52,731	0.7 (3.9)	10.8
Single mesh with 0.5 m electrodes binning	87,245	159,656	1.1 (46.6)	10.9

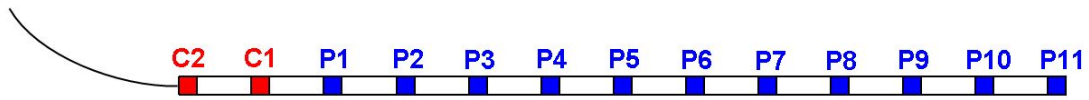


Figure 1. Schematic diagram of a mobile streamer. C1 and C2 are the current electrodes while P1 to P11 are the potential electrodes.

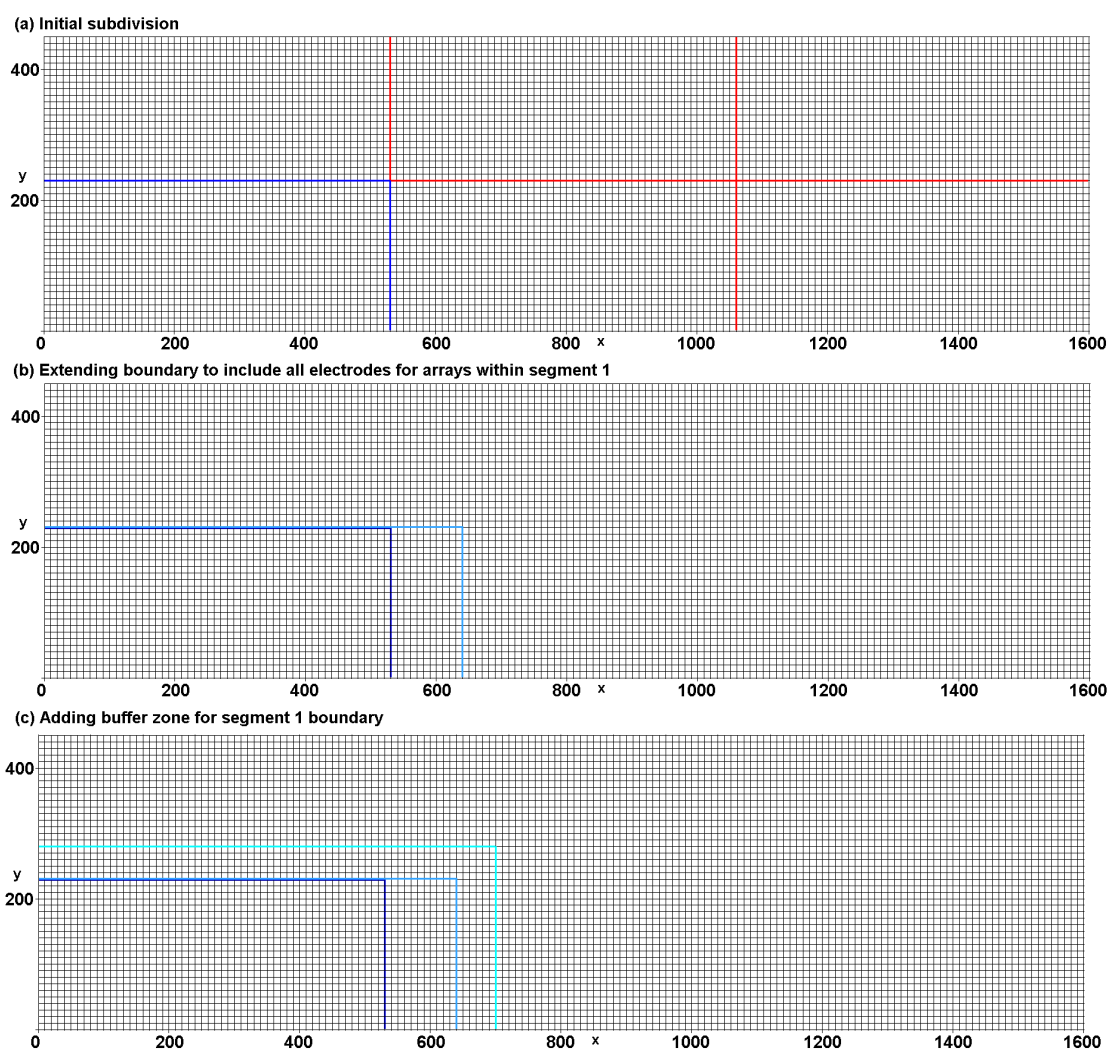


Figure 2. Method used to subdivide a model with 160 by 45 cells (of 10 m width in the x and y directions) in each layer subdivided into 6 segments. (a) Initial subdivision into 6 segments of approximately equal size. The dark blue line marks the region covered by segment 1. (b) Extending the boundary (medium blue line) of segment 1 so that it includes all the electrodes for data points in this segment. (c) Adding a buffer zone around the segment to minimise edge effects. The final region covered by segment 1 is shown by the light blue line.

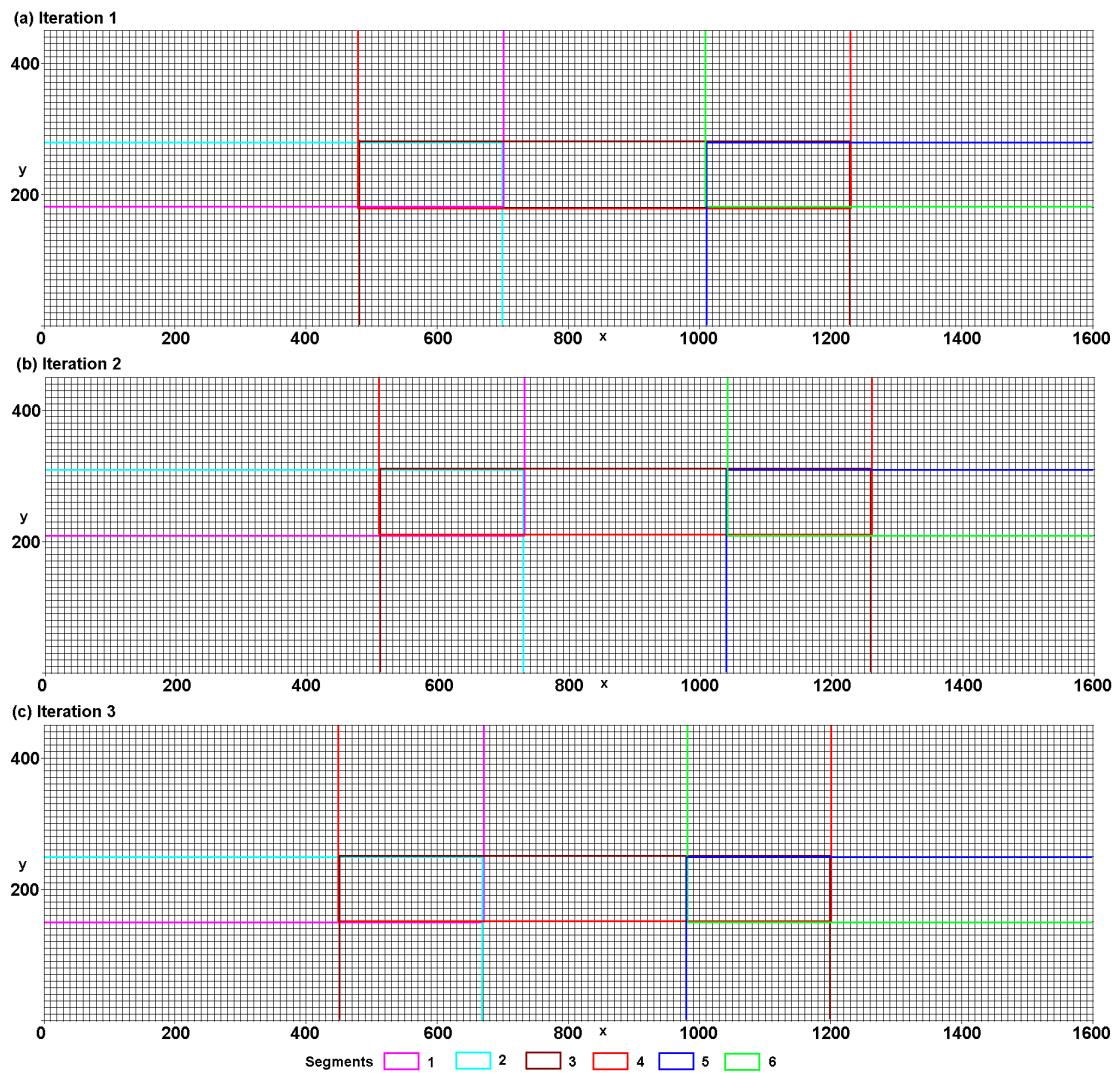


Figure 3. (a) The initial regions of the model grid covered by the 6 segments used in iteration 1 of the least-squares optimisation algorithm. Note the overlaps between neighbouring segments. (b) Shifting of the boundaries of the segments forwards by 3 model grid lines (compared to those used in iteration 1) in iteration 2. (c) Shifting of the boundaries of the segments backwards by 3 model grid lines (compared to those used in iteration 1) in iteration 3.

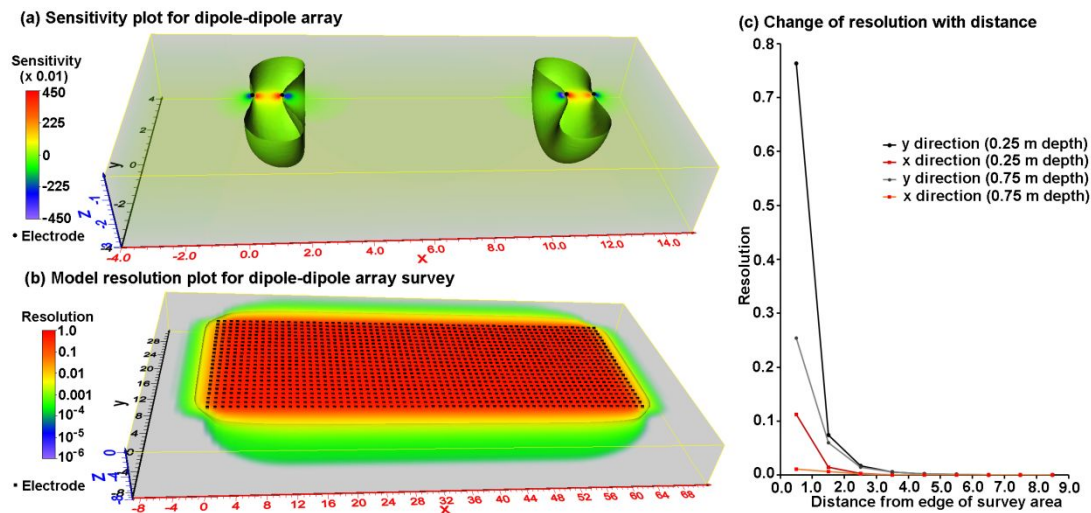


Figure 4. (a) 3-D plot of sensitivity values for the dipole-dipole array with $a=1$ m and $n=10$. The electrodes are located at x positions of 0, 1, 11 and 12 along the $y=0$ axis. The isosurface for sensitivity value of 0.01 is shown. (b) Plot of resolution values for a dipole-dipole array survey with $a=1$ m and $n=1$ to 10 with electrodes in a 64 by 23 grid. The 0.005 isosurface is shown. The electrodes are marked by black dots on the surface. (c) Change of resolution with distance from edge of survey grid at the x and y boundaries. The resolution values of cells at the mid-point of the x and y boundaries (which have the highest values) are shown.

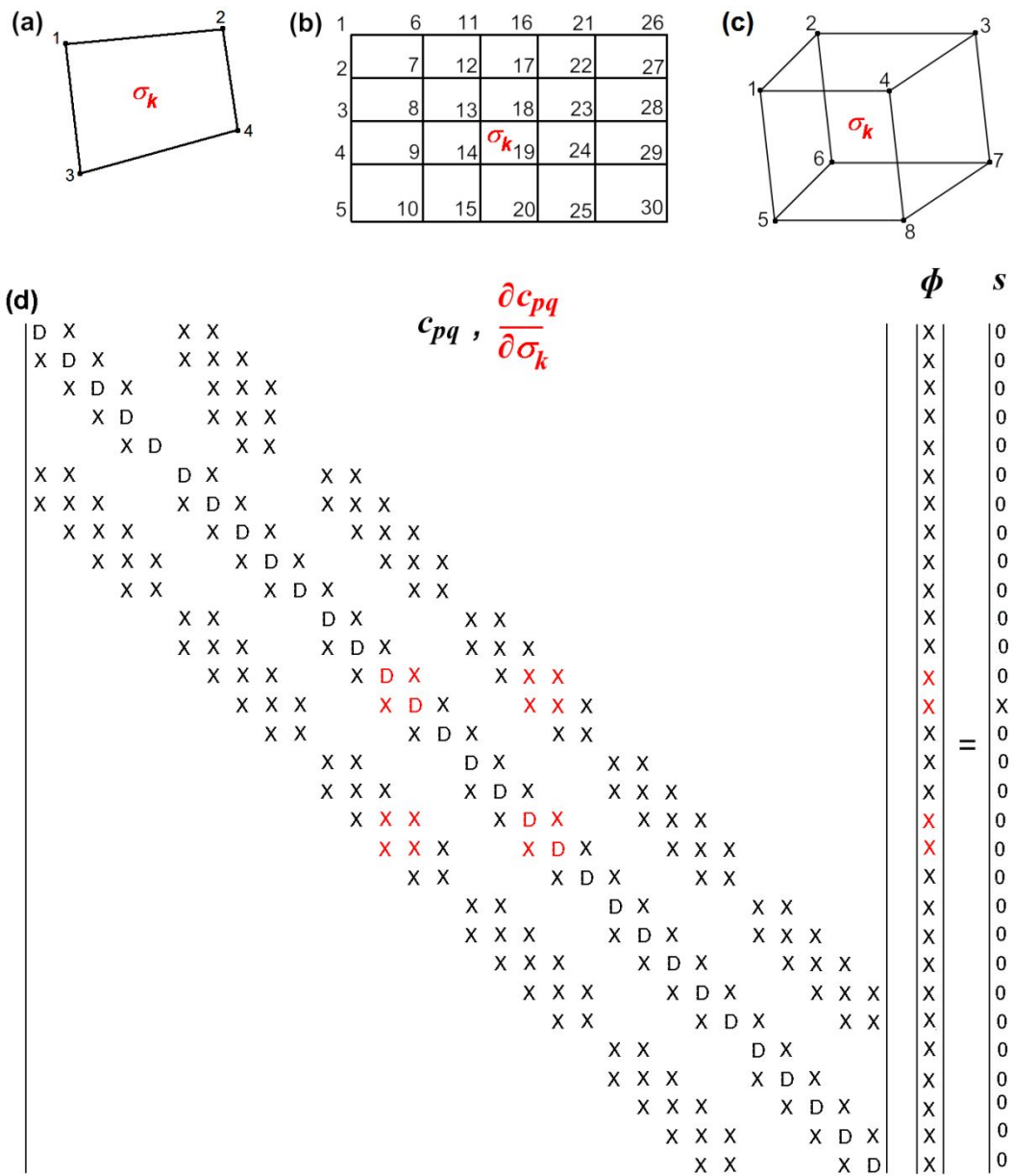


Figure 5. (a) 2-D quadrilateral element with 4 nodes. (b) Example 2-D finite-element mesh with node numbers. (c) 3-D hexahedral element with 8 nodes. (d) Schematic diagram of the structure of the capacitance matrix equation for the 2-D mesh with the non-zero elements. D represents a diagonal element while X represents a non-zero off-diagonal element. The members of the $\frac{\partial C}{\partial \sigma_k}$ matrix (due to a change in the conductivity of the k mesh cell) that have non-zero values are marked in red.

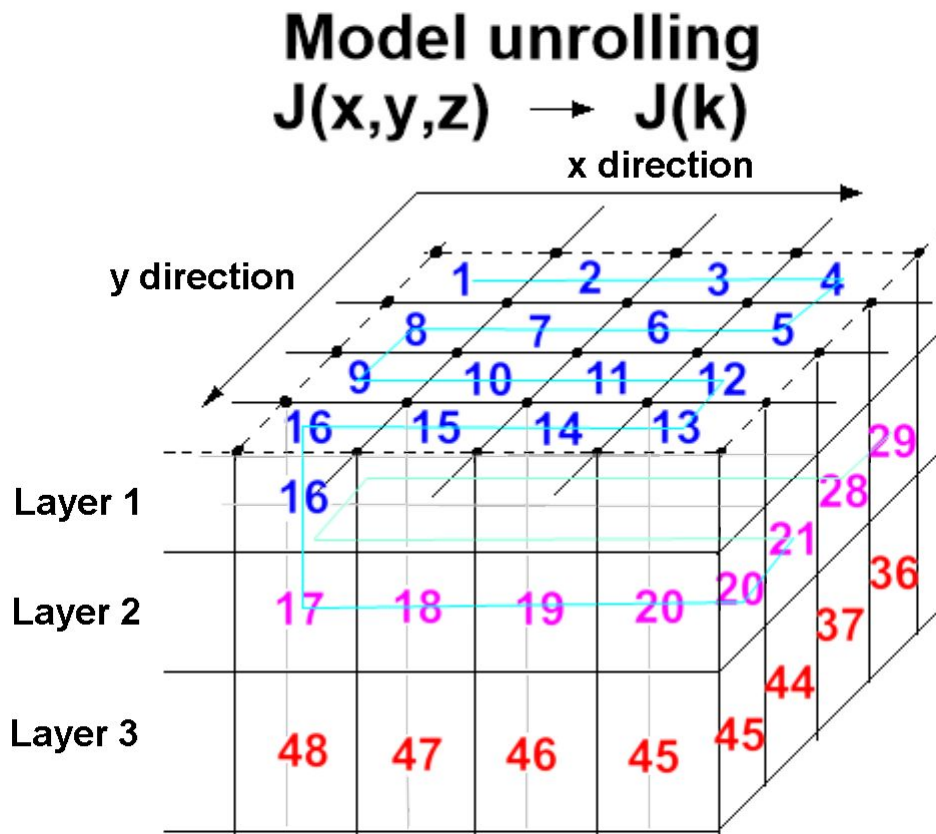


Figure 6. Numbering of model cells arranged in a 3-D rectangular grid so that the Jacobian matrix which is a 3-D function of (x,y,z) is converted to a continuous 1-D function of the model cell index k .

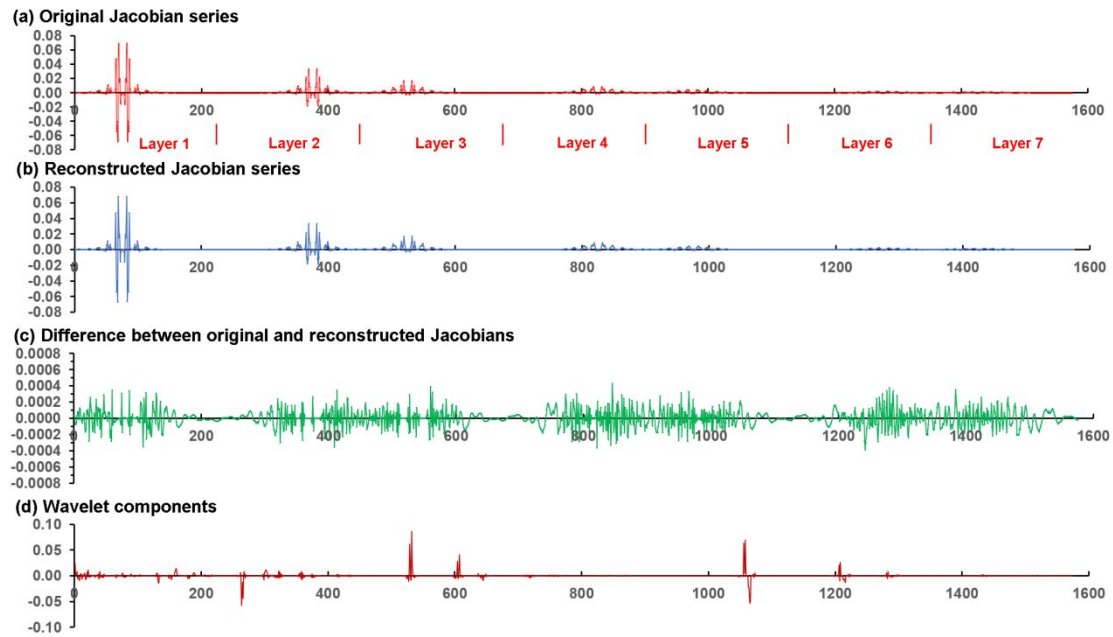


Figure 7. (a) Plot of the Jacobian values for a single pole-dipole array ($a=2$, $n=1$) for a model with $15 \times 15 \times 7$ model cells (each layer has 225 cells). (b) The reconstructed Jacobian values after wavelet components with amplitudes of less than 0.5% of the maximum value were removed. (c) Plot of the difference between the original and reconstructed Jacobian values. Note the vertical scale is 100 times smaller than (a) and (b). (d) Plot of the wavelet components. The quantity Values in vertical axis in the plots is are dimensionless while the horizontal axis is the model cell index number in (a), (b) and (c), and the wavelet wave number in (d).

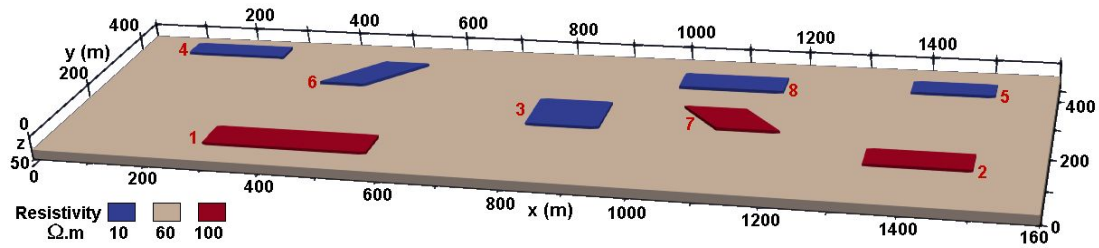


Figure 8. Synthetic model with 8 blocks in the upper layer of a two-layer medium.

The top layer (transparent in the plot) has a resistivity of 30 Ω .m and a thickness of 23.2 m. Blocks 1 to 5 have a depth range of between 0.0 and 5.0 m, while blocks 6 to 8 have a depth range of 5.0 and 10.5 m. Blocks 1 to 5 extend from the surface (0.0 m) to a depth of 5.0 m. The top of blocks 6 to 8 is at 5.0 m while the bottom is at 10.5 m depth.

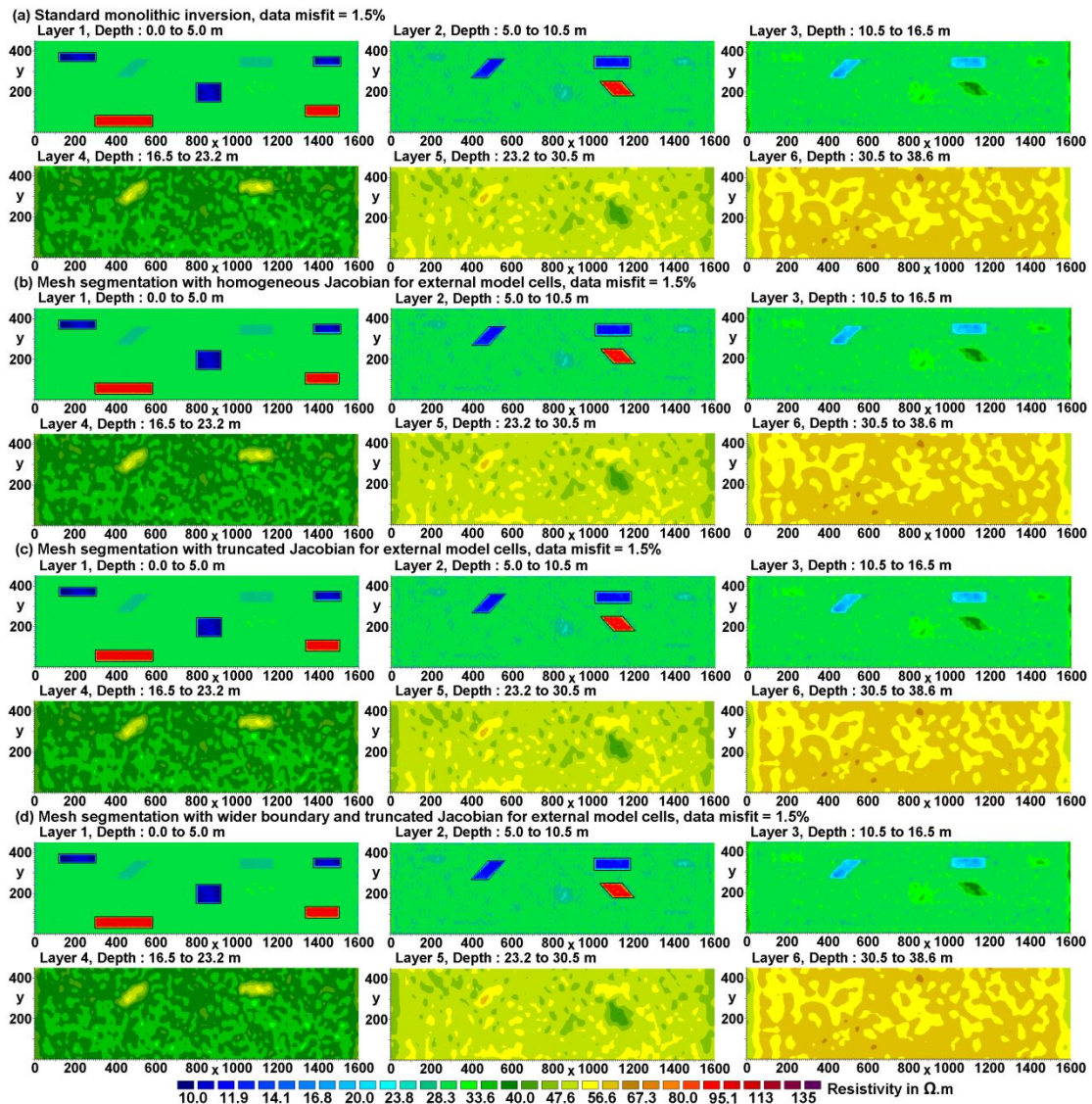


Figure 9. Inverse models of synthetic data set with (a) standard monolithic inversion, (b) using 6 segments with buffer zone of 5 model cells and homogeneous Jacobian approximation for external cells, (c) using segments with buffer zone of 5 model cells and truncated Jacobian for external cells and (d) using segments with buffer zone of 8 model cells and truncated Jacobian for external cells. The blocks in the synthetic model are shown by black outlines in the first 2 layers.

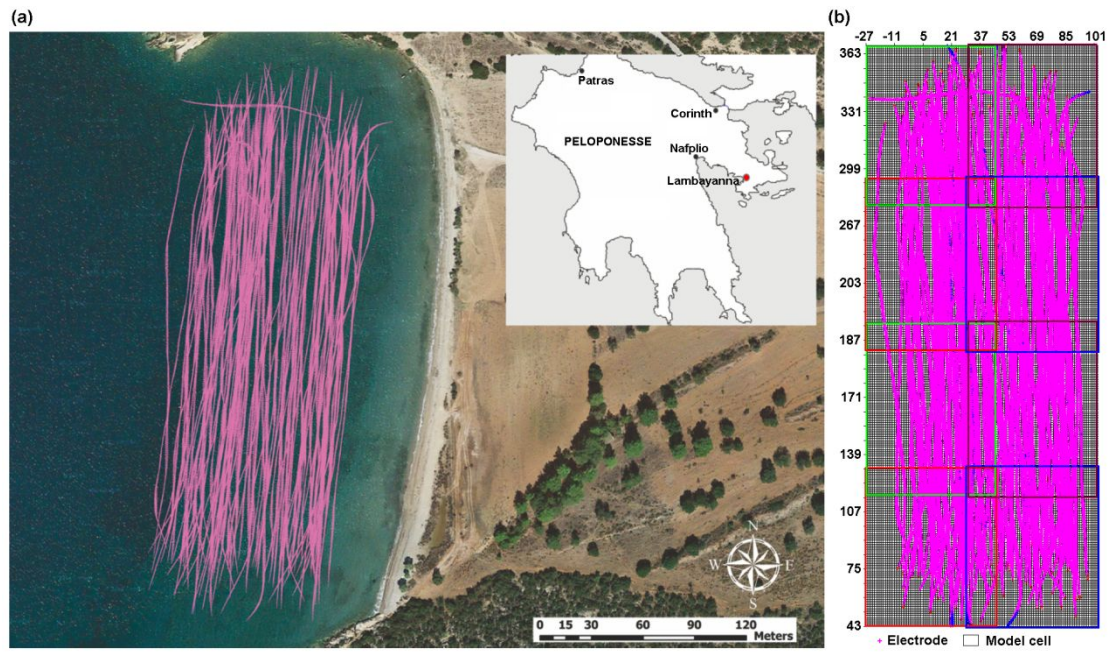


Figure 10. Lambayanna survey (a) map (survey location marked by red circle) and (b) inverse model grid (segments shown by coloured grid lines).

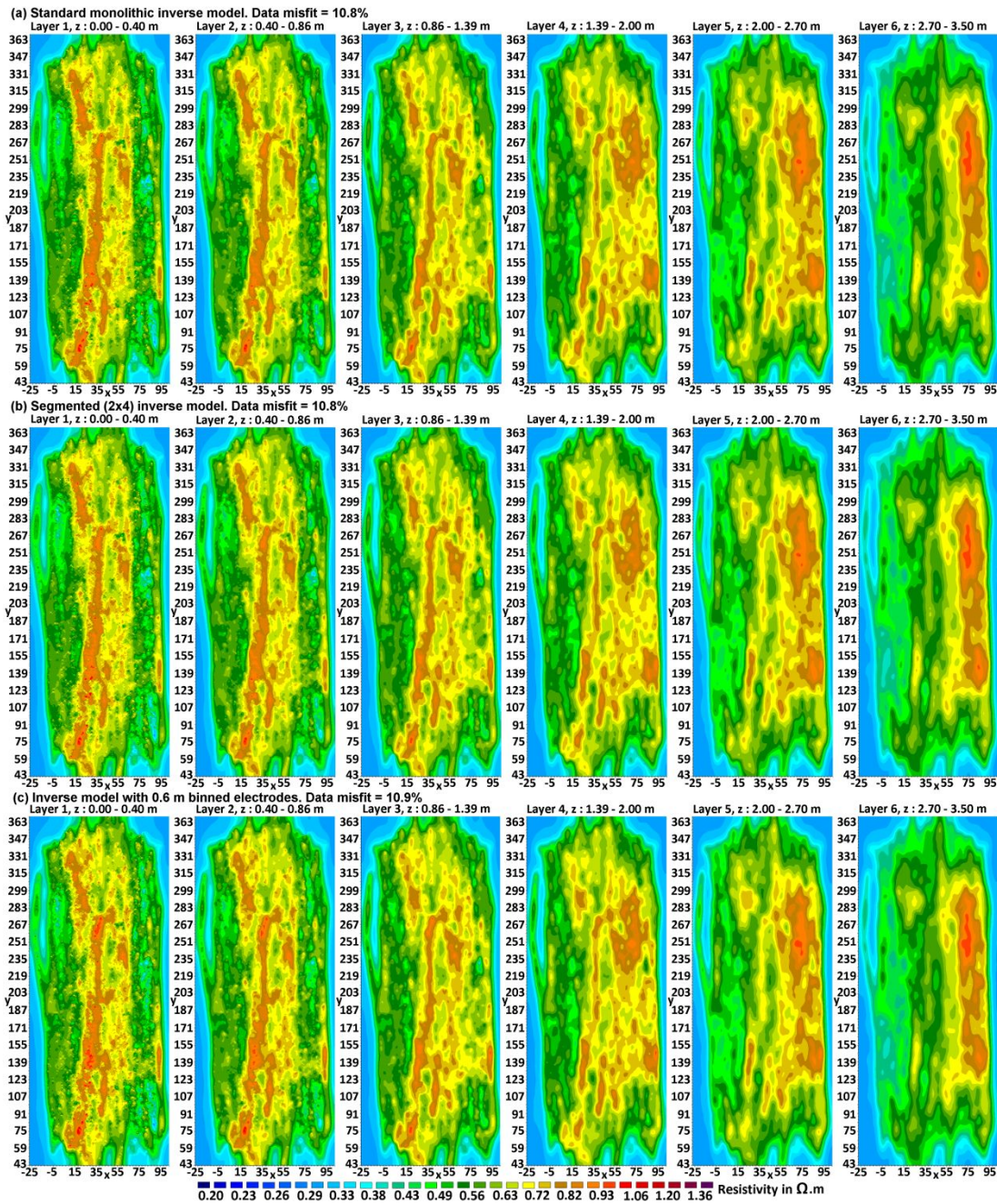


Figure 11. Lambayanna survey inverse models using (a) standard monolithic inversion with a single mesh, (b) 2 by 4 segmented mesh and (c) electrodes binned to every 0.5 m.

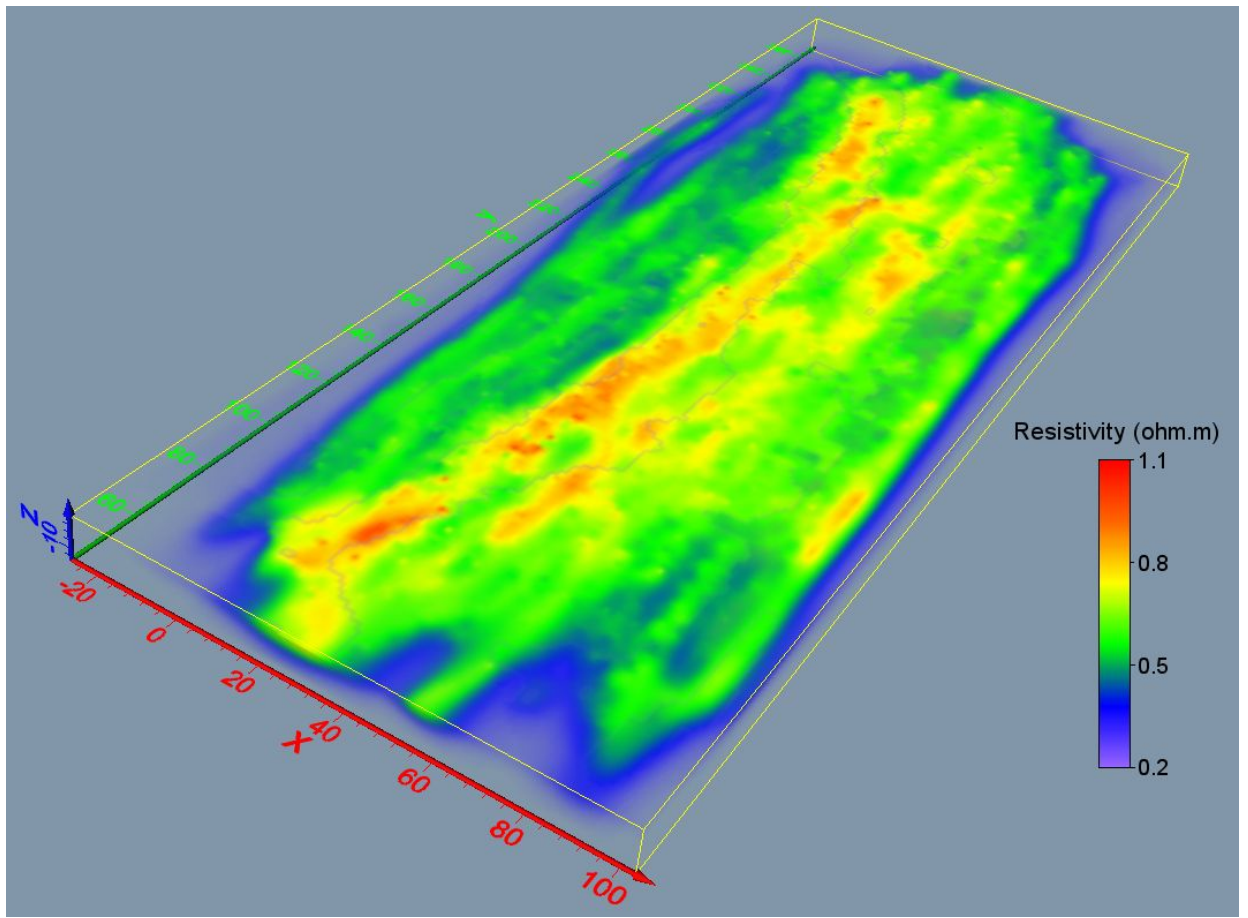


Figure 12. 3-D plot of Lambayanna survey inverse model below the water layer.

Response to reviewers

In the revised manuscript, we have marked the changes made by blue text. In the discussion below, comments by reviewers are in italics while our response are in normal text.

Reviewer 1

Comment

1. The model decomposition method used in this paper is not the best one. I suggest the authors to refer Yang et al.(2014, GJI)'s work. Their method is more practical without dealing with the boundary problem between different sub-meshes. Although their algorithm needs a more complex method to decompose the mesh, the Jacobian matrix is sparser and don't need additional wavelet transform to compress it.

Response

The paper does have some interesting methods that could further reduce the calculation time. The two methods are the most useful are (a) using a series of local meshes with much smaller number of nodes compared to a single mesh (i.e. the monolithic approach in our manuscript) (b) using a subset of the data set instead of the entire data set. The paper is on inversion of AEM surveys that uses a single source-receiver combination for the measurements (i.e. a single point source-receiver), so the techniques will have to be modified to take into account the different setup used in mobile resistivity surveys that uses arrays with the electrodes spread out along a line (i.e. 2 point sources and 2 point receivers for each measurement, and a series of arrays along the streamer for depth information). Below are our initial assessments on the modifications needed.

(a) The paper uses a single local mesh for a single source-receiver measurement, in this case a series of time measurements for depth sounding compared to the resistivity case where different electrode spacings are used. The Lambayanna data set has 164,414 data points or array configurations. Running the calculations for 164,414 local meshes might take a while although the finite element grids are smaller compared to 8 segments. However, for a 10 channel resistivity meter system, 10 measurements are made simultaneously for depth information (compared to different time measurements in AEM). So, the local mesh system probably needs to be modified for 10 arrays with altogether 12 electrodes rather than for 1 array with 4 electrodes. This will reduce it to about 16,441 local meshes. This will also make it possible to use the fast Jacobian matrix calculations for parallel measurements. Another feature of the mobile survey is that the next set of measurements is frequently made close to the previous measurement set, for example after the cable is moved about 1 m in the Lambayanna field survey. So, it might be more efficient to just extend the local mesh by one model grid line to accommodate another set of 10 measurements, rather solve the finite-element equations with a slightly smaller mesh twice. Extending this further to accommodate nearby almost parallel lines as well leads to the segmentation method. As discussed in the reply to Reviewer 2, there is probably an optimum segment size that provides a balance between speed and accuracy which is a topic for further research. It will require some experimentation to determine whether it is more efficient to repeat the calculations for a single streamer with its own local mesh, or group a number of streamer measurements into a larger local mesh. Reducing the number of Jacobian values calculated will have some effect on the model

accuracy, so a study of its effect on the model accuracy (as was done in this manuscript) needs to be carried out. The effect of truncating the Jacobian on the resistivity model would be different from the AEM case as EM fields probably decay more rapidly with distance compared to electrical potentials. In the segmentation method, it is also possible to save the Jacobian values in a sparse matrix format that uses one single-precision float array to store the Jacobian values for model cells within the segment together with the model cell number in an integer index array (Papadopoulos *et al.* 2011), and leave out the values for model cells outside the segment using a compressed data format instead of using wavelet compression. After that, standard sparse matrix numerical routines can be used for the matrix operations. However, as shown for the synthetic model example, there is some benefit in using the approximate Jacobian values for a homogeneous half-space to fill in the Jacobian values for the model cells outside the segment or local mesh instead of assuming they are zero. In this case, it is necessary to use the wavelet compression.

(b) The idea of using a data subset instead of the entire data set is an attractive option as there is some redundancy in the data. However, there are better ways than using a random subset as done by Yang *et al.* (2014), such as by choosing in a systematic manner the subset that gives the most information. This is in fact the reverse of the array optimization problem (Wilkinson *et al.* 2006; Loke *et al.* 2010). In this optimum subset finder algorithm, we start with the model resolution (or an approximation such as the ‘Modified Goodness Function’ which can be calculated rapidly) for the entire data set using the Jacobian values for a homogeneous half-space (which can be calculated analytically for EM and electrical problems). After that, calculate the decrease in the resolution for each data point after it has been removed from the data set. The data points that cause the least reduction in the resolution are then removed from the data set. In this way, only the data points that provide the most information about the subsurface are retained. It will provide a model with the best resolution for the same number of data points.

The above methods are interesting ideas that are worth pursuing but are best left to another paper. To reflect this, we add the following sentence to the end of the Conclusions section.

“We are also examining ways to adapt the techniques described in Yang *et al.* (2014), such as the use of local meshes and data subsets, to further reduce the computer time and memory required to process very large 3-D resistivity data sets.”

Comment

2. *In Figure 5, I think this method may not result in the best 1D array for compression. The author could rearrange the grid according to the value of Jacobian matrix to obtain smoother 1D curve for compression.*

Response

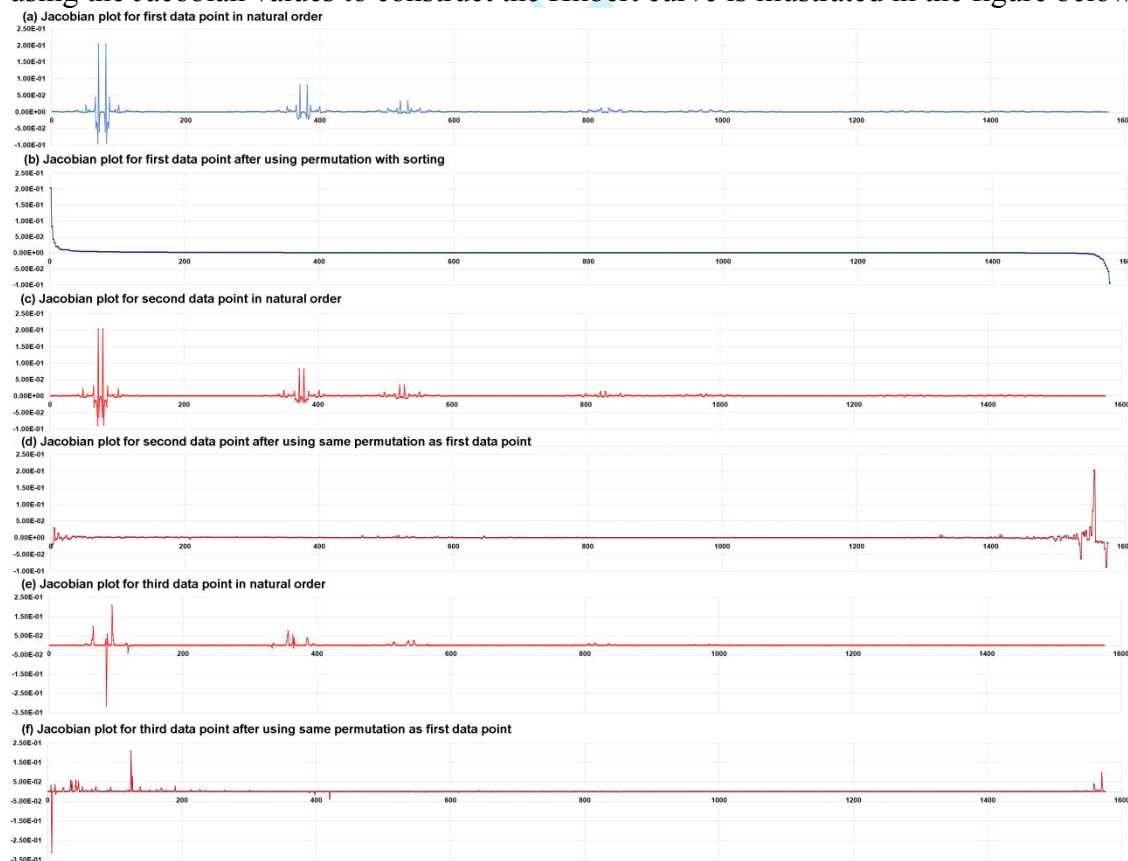
We are not sure how the method proposed by the reviewer would work. Finding a permutation or ordering for the indexing of the model cells in the grid is basically finding a continuous Hilbert curve that maps a 3-D function to a 1-D function (Davis and Li 2013). Figure 5 (Figure 6 in the revised manuscript) shows a simple algorithm to find the Hilbert curve when the model cells are arranged in a rectangular grid. The Hilbert curve must have the following properties.

(a) The same Hilbert curve is used by all the data points.

(b) Neighboring model cells in the 1-D Hilbert curve are also in close proximity in original 3-D grid. For example, cells 16 and 17 (Figure 6 in the revised manuscript) on the Hilbert curve (the light blue line) are also next to each other in the original 3-D grid. The reason for condition (a) is the way the transformed Jacobian is used in the linear conjugate gradient method. In the process of solving equation (1), matrix multiplication multiplications of the form such as $\mathbf{J}\Delta\mathbf{r}$ are used, where \mathbf{J} is the Jacobian matrix and $\Delta\mathbf{r}$ is the parameter change vector. The Jacobian matrix and vector can be represented as

$$\begin{pmatrix} \mathbf{j}_1 \\ \mathbf{j}_2 \\ \dots \\ \mathbf{j}_{n-1} \\ \mathbf{j}_n \end{pmatrix} \Delta\mathbf{r}$$

\mathbf{j}_i is a row vector with m (number of model cells) Jacobian values for the i th data point where the data set has n data points. It is assumed that the Jacobian values for each data point, as well as the elements in the $\Delta\mathbf{r}$ vector, have been rearranged using the same Hilbert curve or permutation vector, such as the numbering in Figure 6 in the revised manuscript. When the wavelet transform is used, the matrix vector multiplication $\mathbf{J}\Delta\mathbf{r}$ becomes $\mathbf{J}\mathbf{A}\mathbf{r}$ where \mathbf{J} is constructed from the transformed Jacobian vectors (\mathbf{j}_i) and $\mathbf{A}\mathbf{r}$ is the parameter change vector after the wavelet transformation. The problem we foresee in using the Jacobian values to construct the Hilbert curve is illustrated in the figure below.



1
2
3 The Jacobian values for the first data point (using the natural ordering in Figure 6) is
4 shown in (a) which shows a continuous 1-D curve. The values can be sorted using a
5 sorting algorithm (such as Quicksort) to rearrange the Jacobian values with decreasing
6 amplitudes such as in (b). This does show a smooth curve, so the wavelet transform
7 should be more compact. The Jacobian for the second data point is shown in (c) that has a
8 different pattern from (a) since the electrodes are at different positions. If we use the
9 same permutation as was used for the first data point (due to the condition that the same
10 permutation or Hilbert curve must be used for all data points), we end up with the curve
11 in (d) which is worse than the original curve (c). In general, we get a random pattern if
12 the permutation that was optimal for the first data point is used for other data points since
13 their Jacobian vectors will have different patterns. For example, (e) and (f) shows the
14 original Jacobian plot for a third data point and the curve after permutation. Note (d) and
15 (f) do not show the simple smooth curve in (b). If we use different permutations or
16 Hilbert curves for different data points, this will lead to several problems. Firstly, we
17 need to store the permutation vector for each data point (instead of just 1 permutation
18 vector) which requires a storage space which is the same as the entire Jacobian matrix.
19 Secondly, if we want to multiply the transformed Jacobian for \mathbf{J} (where different
20 permutations are used for different data points) with the vector $\Delta\mathbf{r}$, we need to carry
21 164,414 wavelet transformations of $\Delta\mathbf{r}$ for the Lambayanna data set instead of just 1 (if
22 we use the same permutation in Figure 6 for all the data points). That is the reason the
23 Hilbert curve or permutation vector is constructed based on the geometrical arrangement
24 of the model cells instead of the Jacobian values, so that a single Hilbert curve can be
25 used for all data points.

26
27 It is possible newer research that we are not aware of that has overcome the restriction of
28 using the same Hilbert curve for all data points without incurring extra storage space and
29 calculation time, but without a reference and for the reasons explained above, we have
30 not made any changes to our method.
31
32
33
34
35

36 Reviewer 2

37 Comment

38
39 1) 1- Mesh: There is no clear explanation on how the selection of the cell size is done.
40 Based on the average data spacing or on the streamer array dimensions or else?

41 Response

42 We thank the reviewer for pointing this out. We have added the following sentence to the
43 “Mesh segmentation” section as part of the new paragraph concerning the buffer zone.

44 “The x and y lengths of the model cells are usually set to be the same as the minimum
45 spacing between adjacent electrodes in the streamer.”

46 We use “minimum spacing between adjacent electrodes” as some streamers might use
47 larger spacings towards the end to get a stronger signal strength (for example in Unrau
48 (2019)), although both examples in the paper use a uniform electrode spacing. Using this
49 electrode spacing to set the x and y dimensions of the model cells seems to be the best
50 compromise to get the best resolution with the minimum computer time and memory. It
51 is possible to use smaller model cells, such as half the electrode spacing but this will
52 increase the number of model cells (and thus the computer time and memory) by four
53 times. Field data sets using mobile systems usually have a significantly higher noise level
54
55
56
57
58
59
60

1
2
3 than conventional static resistivity meters, so it is usually not justified to use a finer
4 model grid.

5 Concerning the thickness of the model layers, particularly for field data sets where the
6 depths to the structures are not known in advance, we added the following sentences to
7 the second paragraph in the “Lambayana field data set” section.

8 “The thickness of the first layer is set at the minimum depth of investigation (Edwards
9 1977) of the data set. The thickness of each deeper layer is increased by 15% since the
10 data resolution decreases with depth. The maximum depth of investigation of the data set
11 is used as a guide to set the depth to the bottom layer.”

12
13 Normally the depth to the bottom layer is set to slightly more than the maximum depth of
14 investigation.

15
16
17 *2- buffer zone between segments: various extensions of segment (buffer zones) have been*
18 *used in the paper. 3, 5 and 8 model cells. What is the decision criteria? trial and error?*
19 *Should not it be selected on the based on the sensitivity (Jacobian) of the buffer cells?*

20 Response

21 This is a valid point that should be discussed in more detail in the paper. We have added
22 a new Figure 4 and the following new paragraph to the ‘Mesh segmentation’ section that
23 discusses the issue in more detail.

24
25 “The segmentation algorithm extends the final boundaries of the segments by at least 5
26 model grid lines. The widths of the model cells are usually set to be the same as the
27 distance between adjacent electrodes in the streamer. Extending the boundaries to a larger
28 distance should increase the accuracy of the model obtained by the segmentation method
29 (compared to a normal single mesh inversion) but at the cost of larger computer memory
30 and time. To estimate the optimum distance to extend the boundary, we first examine the
31 sensitivity values for a dipole-dipole array survey similar to that used in the synthetic
32 model and field survey discussed in this paper. Figure 4a shows a 3-D plot of the
33 sensitivity values (Frechet derivative) for a dipole-dipole array with $a=1$ m and $n=10$ for
34 a homogeneous medium that can be calculated analytically (Loke and Barker 1996). The
35 regions with the highest sensitivity values are located near the electrodes. The isosurface
36 plot shows the regions with significant sensitivity values are located near the dipoles and
37 elongated in the direction perpendicular to the axis of the array. Figure 4a shows the
38 model sensitivity distribution for a single array. To study the characteristics of a data set
39 that consists of many arrays, the model resolution is used (Loke *et al.* 2014b). The
40 resolution value of a model cell is limited to between 0.0 (no resolution) to 1.0 (perfect
41 resolution). We calculate the resolution values for a data set from a survey grid with 64
42 by 23 electrodes (Figure 4b), with all the possible dipole-dipole measurements with $a=1$
43 m and $n=1$ to 10 in the x -direction only (giving a total of 12995 data points). The survey
44 grid and number of electrodes is similar to a single segment in Figure 2. Figure 4b shows
45 a 3-D plot of the resolution values. The subsurface is divided into uniform cells with
46 dimensions of $1.0 \times 1.0 \times 0.5$ m. The maximum resolution value at the surface near the
47 centre of the survey grid is about 0.84. The resolution values gradually decrease with
48 increasing distance from the edge of the survey grid. The band with significant resolution
49 values is wider at the y boundaries compared to the x boundaries. This is because the
50 measurements are only made in the x direction, and the zone with higher sensitivity
51 values are elongated in the direction perpendicular to the array axis. Figure 4c shows the
52
53
54
55
56
57
58
59
60

change in the resolution values at the x and y boundaries with distance from the boundaries. For the y boundary, the cell at the surface immediately next to the boundary has significant resolution value of 0.76. The resolution rapidly decreases with distance to about 0.002 at 4.5 m. So, extending the segment boundary up to 5 times the unit electrode spacing should include all the regions with significant resolution values. Figure 4c also shows that the resolution values are lower at the x boundary, and also decreases with depth. Field data sets sometimes have measurements in both directions, so the boundary is normally extended by the same distance in both directions. Most conventional arrays have sensitivity patterns that do not extend as far out as the dipole-dipole array (Loke *et al.* 2014b). So, extending the segment boundaries to about 5 times the unit electrode spacing is a conservative approach that should cover most field surveys situations.”

Note the plot for the sensitivity in Figure 4a is actually the Frechet derivative which is independent of the model discretization used. The Jacobian is the integral of the Frechet derivative over the volume of the model cell. The model resolution which has a fixed range of between 0 and 1, and is a better measure of how well we can resolve an anomaly. It might be possible to trim the buffer to 4 cells (the resolution for the cell between 4 and 5 m is about 0.002) to save some calculation time, but it is probably not advisable to go down to 3 cells as the resolution for the cell between 3 and 4 m is 0.006. The resolution values are for a homogeneous half-space. If there is a large resistivity contrast, such as a low resistivity structure just outside the boundary, the resolution values there are likely to be higher. So, using a minimum of 5 buffer cells seems to be a safe option. Our approach in the paper is to reduce the calculation time with minimal effect on the accuracy.

I believe the 3 cells is only discussed in relation to shifting the boundary between iterations, not in setting the buffer zone. Padding the Jacobian for cells beyond 5 buffer cells with the Jacobian for a homogeneous medium helps to reduce the errors. The 8 buffer cells option is only recommended when it is not possible to use the homogeneous half-space Jacobian as an approximation. The segmentation technique is likely to be used for very large surveys carried out by field geophysicists/engineers/geologists, so we tend to choose conservative settings that are robust and likely to work in most situations for non-experts rather than those that are absolutely the most computationally efficient.

Comment

3- *The moving of the segment boundaries back and forth at each iteration in the inversion process : the reasons for this strategy is not clearly explained. What are the advantages of doing so? If the boundaries were kept unchanged at each iteration would it be a different result?*

Response

In the paper we did include the following sentence.

“To avoid the build-up of artefacts near the edges of the segments, the boundaries of the segments are changed after each iteration.”

If there are any artefacts, shifting the boundaries should smear out the artefacts thus reducing them. We have conducted a test using fixed boundaries for the synthetic data set. We have added the following sentences to the ‘Synthetic model test’ section.

1
2
3 “We also carried out an inversion with the fixed segment boundaries (instead of changing
4 after each iteration). The resulting model resistivity values also had an average difference
5 of 0.2% but the maximum difference was higher at 2.4%.”

6
7 It did not change the average difference in the inverse model resistivity values much but
8 caused a slight increase in the maximum difference. There is no disadvantage in changing
9 the boundaries after each iteration since the overall mesh size and number of model cells
10 remain the same (as one segment is increased, another is reduced), so we prefer to shift
11 the boundaries as a ‘safer’ option for the general user.
12

13
14 *Comment*

15 *4-The number of segments: what is the criteria, given a large dataset, for the selection of*
16 *the segment size?*

17 *Response*

18 This was actually discussed in the previous manuscript at the end of the ‘Conclusions’
19 section in the following sentences.

20 “In general, a conservative approach is followed that uses the minimum number of
21 segments so that the inversion can be carried out with the available computer resources. It
22 is recommended that the length of a segment should not be less than 5 times the
23 maximum distance between two electrodes in an array aligned along the same direction
24 as the side of the segment. However, the size and number of segments that provides an
25 optimum balance between reducing the calculation time and accuracy of the results is an
26 area that requires further research.”

27
28 Obviously, the length of a segment cannot be less than the length of the streamer. Due to
29 the sensitivity to model cells beyond the streamer, it should preferably be at least several
30 times longer than the streamer (see reply to Reviewer 1 about computational issues in
31 relation to the local mesh size). If there are more segments, the overlap between the
32 segments due to the buffer cells becomes more significant which might increase the
33 computer time beyond a certain limit. In theory the fewer segments that are used, the
34 closer the results should be to that obtained with a single mesh (i.e. 1 segment). The use
35 of segments is in response to a practical computational problem faced by small
36 companies who have to complete the survey report within a limited time frame with
37 normal PCs or workstations. So, at present our recommendation is to use the minimum
38 number of segments so that the calculation can be completed within the time and
39 computer resources available. There is probably an optimum balance in terms of
40 computer time and accuracy in the number of segments for a data set, but as stated in the
41 paper this is still an area of research so we cannot give precise guidelines at present. For
42 the present paper, we move the discussion about setting the number of segments to a new
43 ‘Discussion’ section to make it more prominent as shown below.
44
45

46
47 “The use of segments to reduce the calculation time is designed for the inversion of very
48 large data sets with limited computational resources. This situation is frequently
49 encountered by small geophysical companies using personal computers or workstations.
50 In general, a conservative approach is followed that uses the minimum number of
51 segments so that the inversion can be carried out with the available computer resources. It
52 is recommended that the length of a segment should not be less than 5 times the length of
53 the streamer for arrays aligned along the same direction as the side of the segment. As an
54 example, in Figure 11 most of the measurements are in the y-direction using a streamer of
55
56
57
58
59
60

12 metres. Thus, the length of the segments in the y -direction should be at least 60 metres. It is also recommended that the length of a segment in one direction should be not be more than twice the length in the other direction. However, the size and number of segments that provides an optimum balance between reducing the calculation time and accuracy of the results is an area that requires further research.”

The recommendation that the lengths of the two sides of a segment should not be more than 2 times is to avoid long and thin segments, and also from our observation that it is computationally more efficient to solve the finite-element method for a mesh with a square grid, or at least when the number of nodes in two directions (the x and y) are not greatly different. It would be interesting to conduct research on a more systematic method to setup the number and size of the segments, perhaps including some of the suggestions from Reviewer 1, to get the optimum balance between computer time and model accuracy. This requires an estimation of the number of numerical operations as a function of the number and size (in terms of number of nodes in the finite-element mesh) of the segments. This is a non-trivial issue which we leave to a future paper.

Comment

5-There are some confusion/ambiguities in the application to survey data in Lambayana. The recovered resistivity model from inversion of the dataset do not seem to fit with the mesh description. The first 5 top layers (0 to ~5m) should be the sea water (0.17 ohm.m). In the results shown in Fig 10 the top layers (0-0.4m and deeper) there are changes in resistivities and values are higher than 0.17 ohm.m. I guess that those layers shown in Fig 10 are the first in the sediments below sea water. In that case the description of the selected mesh (10 layers with 5 topmost as sea water) should be changed.

Response

The reviewer is right the model shown in Figure 10 is only for the sediments below the water layer. The number of nodes in the vertical direction in the finite-element mesh is different from the number of layers, excluding the topmost 5 mesh levels for the water layer which is considered a single layer. Firstly, the topmost layer of the model below the water layer is subdivided into 2 vertical nodes, and extra nodes are used below the last layer so that the last mesh line is sufficiently far away so that the mixed boundary condition can be used. To remove that ambiguity, we add sentences to that section to as follows.

“The mesh has 419, 1004 and 23 nodes respectively in the x , y and z directions. Out of the 23 nodes in the z direction, 5 nodes are used to model the water layer while 7 nodes are used for the bottom section of the mesh below the last model layer. The spacing between the 7 bottom mesh lines are progressively increased so that the last mesh line is sufficiently far away from the electrodes (Dey and Morrison 1979). The remaining 11 nodes are used for the 10 model layers with the top layer (which is closest to the electrodes) subdivided in two mesh lines. Figure 12 shows a 3-D plot of the model for the sediments below the water layer. As the water layer resistivity is fixed, it is not shown in the model plots.”

Comment

6-Figures 8 and 10: the color bar and legend should be enlarged. It is difficult to read colors and numbers.

Response

Larger fonts are used for the text and larger boxes are used for the legend in the revised figures.

Comment

7- Figure 9: The inserted map (of Peloponnesus in Greece?) has detailed names of places that cannot be read. The survey location is poorly indicated (green mark). Just show the contour of the same area with one or two known cities and a clear mark (square, dot, circle) for the survey area.

Response

We have modified the small insert with a black outline showing the section of Greece near the survey area with a few cities marked and a small red circle for the survey area.

Comment

Some typo errors and orthographic corrections are also suggested in the annotated manuscript.

Response

We thank the reviewer for his careful reading of the manuscript. We have corrected the typos and made slight modifications to the text in sections that are not clear.

Associate Editor

Comment

Although it is not essential you may give some information about the Daubechies wavelet (the original paper is too long, 88 pages, to find wavelet 4) and numerical values of dilation and translations parameters. If you want to give detailed information about the application of wavelets in your problem you can include an appendix.

Response

We have added a short Appendix with the practical details on using the wavelet transform. We assume most readers will be more interested in implementing it rather than the theoretical details, so we direct the reader to Press et al. (2007) that has a short and more readable description of the wavelet transform, as well as the numerical values for the transform coefficients and a computer code. As most geophysicists are probably more familiar with the FFT, we try to relate the DWT to the FFT.

References

- Davis K. and Li K., 2013. Efficient 3D inversion of magnetic data via octree-mesh discretization, space-filling curves, and wavelets. *Geophysics*, **78**, 1942-2156.
- Loke, M.H., Wilkinson, P. and Chambers, J., 2010. Fast computation of optimized electrode arrays for 2D resistivity surveys. *Computers & Geosciences*, **36**, 1414-1426.
- Papadopoulos, N.G., Tsourlos P., Papazachos C., Tsokas G.N., Sarris A. and Kim J.H., 2011. An algorithm for fast 3D inversion of surface electrical resistivity tomography data: application on imaging buried antiquities. *Geophysical Prospecting*, **59**, 557-575.

- 1
2
3 Press, W.H, Teukolsky, S.A., Vetterling, W.T. and Flannery, B.P., 2007. Numerical
4 Recipes: The Art of Scientific Computing (3rd Edition). Cambridge University
5 Press.
6
7 Unrau T., 2019. Towed Capacitively Coupled Resistivity Systems in Arctic Exploration -
8 Advances in Equipment Design and Handling of Very Large Resistivity Surveys.
9 AGU 100 Fall Meeting, San Francisco, 9-13 Dec. 2019, NS22A-07.
10
11 Wilkinson, P.B., Meldrum, P.I., Chambers, J.C., Kuras, O. and Ogilvy, R.D., 2006.
12 Improved strategies for the automatic selection of optimized sets of electrical
13 resistivity tomography measurement configurations. *Geophys. J. Int.*, **167**, 1119-
14 1126.
15
16 Yang, D., Oldenburg, D.W. and Haber, E., 2014. 3-D inversion of airborne
17 electromagnetic data parallelized and accelerated by local mesh and adaptive
18 soundings. *Geophysical Journal International*, **196**, 1492–1507.
19
20
21
22
23
24
25
26
27
28
29
30
31
32
33
34
35
36
37
38
39
40
41
42
43
44
45
46
47
48
49
50
51
52
53
54
55
56
57
58
59
60